

**IN PURSUIT OF AN OPTIMUM OPTICAL IMAGING
TECHNOLOGY FOR EARLY DETECTION OF DENTAL
CARIES**

ELNAZ BARADARAN SHOKOUHI

A THESIS SUBMITTED TO THE FACULTY OF GRADUATE STUDIES IN
PARTIAL FULFILLMENT OF THE REQUIREMENTS FOR THE DEGREE OF
MASTER OF APPLIED SCIENCE

GRADUATE PROGRAMME IN MECHANICAL ENGINEERING

YORK UNIVERSITY

TORONTO, ONTARIO

© ELNAZ BARADARAN SHOKOUHI, 2018

Abstract

Clinical caries detection techniques, such as radiographs, are not sensitive to detect and monitor the progression of caries at early stages. In recent years, several optics-based imaging modalities have been proposed for early detection of caries. In this thesis, we report on a systemic comparative study on the performances of optical coherence tomography and thermophotonic lock-in imaging (TPLI) as early caries detection imaging modalities based on light scattering and absorption, respectively. Through controlled demineralization on extracted human teeth, our results suggest that TPLI provides better sensitivity and detection threshold in detecting early stages of caries. The outcome justifies the need for a light-absorption based imaging modality to produce depth-resolved images. Therefore, preliminary imaging studies on a 3-D imaging platform known as a Truncated-Correlation Photothermal Coherence Tomography (TC-PCT) system was conducted to achieve optimal diagnostic yield. The results demonstrate that TC-PCT can detect early caries with significant enhancement in depth-resolution.

Acknowledgement

To my mother and father.

I would like to give a sincere thanks to Prof. Tabatabaei for his unconditional support and guidance all throughout my research.

Table of Contents

Abstract	ii
Acknowledgement	iii
Table of Contents	iv
List of Tables	vi
List of Figures	vii
List of Acronyms	xi
Chapter 1: Introduction	1
1.1 Prevalence and Challenges in Early Caries Detection and Management.....	1
1.2 Structure of Human Tooth and Early Dental Caries	2
1.3 Mechanism of Caries Formation	3
1.4 Classification of Caries	6
1.5 Light-Tooth Interactions	8
1.6 Existing Optical Methods.....	10
1.7 Optical Coherence Tomography (OCT).....	13
1.8 Thermophotonic Lock-in Imaging (TPLI)	17
1.9 The Objectives and Outlook of the Thesis	20
Chapter 2: Theory	22
2.1 Caries Detection in Long Wave Infrared Thermophotonic Imaging	22
2.2 Optical Coherence Tomography	27
Chapter 3: Materials, Instrumentation, and Methods.....	30
3.1 Thermophotonic Lock-in Imaging System	30
3.2 Optical Coherence Tomography	32
3.3 Micro Computed Tomography.....	33
3.4 Dental Sample Preparation and Controlled Demineralization Protocol.....	34
3.5 Data Processing and Analysis of OCT and TPLI.....	38
Chapter 4: Comparison of TPLI and OCT in Detection of Early Caries	42
4.1 Detection of Advanced Early Caries	42
4.2 Comparison of Detection Threshold	46
4.3 Detection Sensitivity of OCT and TPLI.....	49
4.4 Summary of the Comparative Study	55

Chapter 5: Truncated-Correlation Photothermal Coherence Tomography (TC-PCT) Analysis ..	57
5.1 Introduction to Matched Filtering in Thermography	57
5.1.1 <i>Linear Frequency Modulation</i>	59
5.1.2 <i>Binary Phase Coding</i>	62
5.2 Matched-Filtering and Truncated-Correlation Photothermal Coherence Tomography	65
5.3 TC-PCT Instrumentation.....	67
5.4 TC-PCT Experiments.....	68
5.5 Summary of the TC-PCT Experiments	79
Chapter 6: Conclusion and Future Directions.....	80
6.1 Conclusion	80
6.2 Future Directions	81
References.....	83

List of Tables

Table 1.1: Absorption and scattering properties of sound and carious enamel at select wavelengths [17].....	9
Table 2.1: Optical (800 nm) and thermal properties of dental tissues	25
Table 3.1: Samples' demineralization schedule and schematic of imaging study sequence.	36
Table 5.1: TC-PCT Imaging Study Parameters	74

List of Figures

Figure 1.1: The tooth and its supporting structure [8], Copyright 2014, Elsevier Health Sciences.	3
Figure 1.2: Demineralization and remineralization of tooth [3], Copyright 2008, Australian Dental Association.	4
Figure 1.3: a) Radiographic image of the cross section of a slice of healthy enamel and its transverse micro-radiography mineral profile, b) radiographic image of the cross section of slice of carious enamel and its transverse micro-radiography mineral profile. μ_s and μ_a represent the scattering and absorption coefficients of sound region of enamel, respectively. μ_s' and μ_a' are the scattering and absorption coefficients of the early carious region in enamel, respectively.....	6
Figure 1.4: Enamel infrared transmission spectrum [19], Copyright 2003, Marcel Dekker.	10
Figure 1.5: Caries on occlusal surface by FOTI are shown by arrows [25], Copyright 2006, Elsevier.	11
Figure 1.6: a) tooth with caries b) fluorescence image show caries as dark areas [30], Copyright 2009, American Institute of Physics.	12
Figure 1.7: OCT scanning coordinate system [35], Copyright 2012, Optical Society of America.	14
Figure 1.8: (a) Tooth with smooth surface caries (L) of (ICDAS II) Code 1. The dashed red line shows the region of interest (ROI) and the caries is visually seen after drying; (b) OCT image of smooth surface caries at ROI, bright shadowed spots show the carious/demineralized lesion (white arrows); (c) Tooth with occlusal surface caries (ICDAS II Code 2); (d) OCT image showing the ROI with caries lesions (white arrows) showing as bright areas and enamel cracking (yellow arrow). E: enamel, D: dentin, EDJ: enamel-dentin-junction [41], Copyright 2017, H. Schneider et al.....	15
Figure 1.9: (a) Photograph of the sample along with (b) amplitude and (c) phase images of tooth with artificially-induced caries [61], Copyright 2018, American Institute of Physics.	19
Figure 2.1: Light absorption in a turbid medium.....	23
Figure 2.2: Theoretical radiometric signal (a) phase and (b) amplitude vs. absorber depth.....	26
Figure 2.3: Phase images of blind holes at different depths [18], Copyright 2016, Ojaghi.	26
Figure 2.4: The working principle of OCT [66], Copyright 2013, Kozobolis et al.....	27

Figure 2.5: Intensity depth profile up to 5 mm in air.....	29
Figure 3.1: (a) Schematic representation of the developed thermophotonic lock-in imaging (TPLI) system. (b) TPLI signal processing [15], Copyright 2012, Nima Tabatabaei.	32
Figure 3.2: Schematic representation of the developed spectral-domain optical coherence tomography (OCT) system. The polarization controller is adjusted to yield interference in the cross-polarization state.....	33
Figure 3.3: Tooth inside the acidic gel.....	37
Figure 3.4: Integrated OCT en-face images using different integration limits along the depth of advanced caries on occlusal surface at (a) surface to 50 μm , (b) 20 μm to 50 μm (c) 20 μm to 500 μm , and smooth surface at (d) surface to 50 μm , (e) 20 μm to 50 μm (f) 20 μm to 500 μm .	39
Figure 3.5: ROC curves of two diagnostic experiments.....	41
Figure 4.1: Photographs of simulated advanced caries on (a) smooth and (b) occlusal surfaces; rectangles depict the location of treatment windows. Representative OCT B-mode images of (c) smooth surface and (d) occlusal caries samples along the solid lines indicated in panels (a) and (b), respectively. Integrated en-face OCT images at 10 days of treatment of (e) smooth and (f) occlusal caries samples. TPLI phase images obtained at 2-Hz modulation frequency at 10 days of treatment for (g) smooth surface (h) occlusal caries samples. (i) and (j) represent the μCT slices along the green and blue dashed lines in panel (f), respectively. Red and yellow arrows point to treatment window and false positives, respectively.....	45
Figure 4.2: (a) Visual image of tooth with artificially-induced caries at 3 locations. (b) TPLI phase image at 2-Hz modulation frequency. Integrated en-face OCT images at (c) 2 days, (d) 4 days, and (e) 8 days of demineralization. B-scan OCT images at (f) 2 days, (g) 4 days, and (h) 8 days of demineralization. μCT images at (i) 2 days, (j) 4 days, and (k) 8 days of demineralization.....	47
Figure 4.3: Average contrast values from early caries and the associated standard deviation of mean for (a) optical coherence tomography (OCT) and (b) thermophotonic lock-in imaging (TPLI), and (c) μCT	48
Figure 4.4: Optical image of the smooth surface of extracted human molar (a) before demineralization and (b) after 15 days of demineralization on the treatment window. Integrated en-face OCT images at (c) 0 days, (d) 1 day, (e) 2 days, (f) 5 days, (g) 10 days, and (h) 15 days	

of demineralization. B-scan OCT images at (i) 0 days, (j) 1 day, (k) 2 days, (l) 5 days, (m) 10 days, and (n) 15 days of demineralization. (o) μ CT image of 15-days treated sample.	50
Figure 4.5: TPLI phase images at 2-Hz modulation frequency at (a) 0 days, (b) 1 day, (c) 2 days, (d) 5 days, (e) 10 days, and (d) 15 days of demineralization. Yellow arrow points to change in contrast at cervical margin due to thinning of enamel and photothermal effects of the underlying cementum. Blue arrow points to part of the enamel which was damaged on day 10 of demineralization due to improper handling.	51
Figure 4.6: Average contrast values from early caries and the associated standard deviation for (a) spectral-domain optical coherence tomography (OCT), (b) thermophotonic lock-in imaging (TPLI), and (c) μ CT.	52
Figure 4.7: Statistically (CI: 95%) identified healthy (blue pixels) and demineralized (yellow pixels) at various stages of demineralization by (a) OCT and (b) TPLI.	54
Figure 4.8: Corresponding (a) sensitivity (S) and specificity (P) values and (b) receiver operating characteristic (ROC) curve.	55
Figure 5.1: (a) Linear frequency chirp signal (b) the outcome of matched filtering	59
Figure 5.2: Cross-correlation of a) two chirp waves and b) two sine waves	60
Figure 5.3: Thermophotonic radar imaging of a transparent sample with different absorption coefficients using (a) Cross-correlation (CC) amplitude; (b) CC peak delay time; (c) CC phase and their mean horizontal profiles; (d-f), respectively [79], Copyright 2011, American Institute of Physics.	61
Figure 5.4: TWR and TLI imaging of plastic step wedge. LIT phase images at (a) 0.01 Hz and (b) 1 Hz; (c) CC amplitude image; and (d) mean horizontal profile of figure (a). Distribution of (e) LIT phase and (f) CC peak amplitude values and standard deviations over the steps [79], Copyright 2011, American Institute of Physics.	62
Figure 5.5: Schematic procedure of Binary Phase Coding (BPC) signal construction in time (top) and frequency (bottom) domains for a 7-bit code and 5 Hz carrier [15, 80], Copyright 2012, Nima Tabatabaei.	63
Figure 5.6: (a) plastic step wedge; (b) LIT phase (unit: degree); (c) BPC peak delay time (unit: millisecond); and (d) BPC phase images (unit: degree). The experiments are obtained at 3Hz The curve in each image shows the mean horizontal profile of the corresponding contrast parameter [80], Copyright 2012, Nima Tabatabaei.	64

Figure 5.7: (a) teeth with inter-proximal early caries. The rectangle shows the imaged area; (b) conventional LIT and (c) BPC phase images [80], Copyright 2012, Nima Tabatabaei.	64
Figure 5.8: Flow diagram of the frequency domain TC-PCT algorithm. The cross-correlation of photothermal chirp with the truncated-reference chirp which are subjected to a controlled delay increment that determines penetration depth [82, 83], Copyright 2011, American Institute of Physics.	66
Figure 5.9: Experimental Setup of TC-PCT [81-84]	68
Figure 5.10: (a) Front and back photographs of the sample (b) amplitude and (c) phase images of TPLI	70
Figure 5.11: (a) the 2-D TC-PCT amplitude and (b) phase planar slices of the sample.....	70
Figure 5.12: (a) Amplitude and (b) phase plots of healthy and defective regions versus slice number	71
Figure 5.13: 3-D visualization of the stacked slices in TC-PCT channels	72
Figure 5.14: 3-D visualization of the stacked slices in (a) amplitude and (b) phase channels	73
Figure 5.15: (a) Amplitude and (b) phase plots of healthy and demineralized regions versus slice number	74
Figure 5.16: 3-D amplitude tomograms of (a) experiment 1, (b) experiment 2, and (c) experiment 3 along with 3-D phase tomograms of (d) experiment 1, (e) experiment 2, and (f) experiment 3. (g) Top view of phase and amplitude 3-D tomograms for better visualization of the lateral heat flow and size of the caries.....	75
Figure 5.17: 3-D amplitude tomograms of (a) experiment 2 and (b) experiment 4, along with 3-D phase tomograms of (c) experiment 2 and (d) experiment 4. (e) Top view of phase and amplitude 3-D tomograms	77
Figure 5.18: 3-D amplitude tomograms of (a) experiment 4 and (b) experiment 5, along with 3-D phase tomograms of (c) experiment 4 and (d) experiment 5. (e) Top view of phase and amplitude 3-D tomograms.	78

List of Acronyms

Acronym	Definition
BPC	Binary Phase Coding
CC	Cross-Correlation
CEJ	Cementoenamel Junction
CP-OCT	Cross-Polarization OCT
DEJ	Dental-Enamel-Junction
FOTI	Fiber-Optic Transillumination
GS	Galvo Scanner
ICDAS	International Caries Detection and Assessment System
LFM	Linear Frequency Modulation
LIT	Lock-In Thermography
LWIR	Long-Wave Infrared
MWIR	Mid-Wave Infrared
NIR	Near-Infrared
OCT	Optical Coherence Tomography
PCT	Photothermal Optical Coherence Tomography
PS-OCT	Polarization Sensitive OCT
QLF	Quantitative Light-Induced Fluorescence
ROC	Receiver Operating Characteristic
SNR	Signal-To-Noise Ratio
TC-PCT	Truncated-Correlation Photothermal Coherence Tomography

TCT	Thermal Coherence Tomography
TPI	Thermophotonic Imaging
TPLI	Thermophotonic Lock-In Imaging
TWR	Thermal-Wave Radar
μ CT	Micro Computed Tomography

Chapter 1

Introduction

This chapter introduces a brief background on prevalence and challenges in early caries detection along with characteristics of human tooth and mechanism of caries formation. Discussion is then followed by an introduction to optical coherence tomography and thermophotonic lock-in imaging as two promising optical imaging modalities for dental caries diagnosis and management.

1.1 Prevalence and Challenges in Early Caries Detection and Management

Dental caries still remains as one of the most common chronic diseases among children aged 5 to 17 years—making it 5 times more common than asthma [1]. Caries are the main reason for 85% of the services that dentists offer in the office [2], and is the main cause of tooth loss in all age groups. Over the last century, foods with excessive sugar are seen to be the main cause of dental caries with minimal effort on public health campaigns against the widespread use of sugars [2]. Although dental caries is largely preventable, once it is formed the disease requires treatment and the longer it remains untreated, the more cumbersome and costly the treatment becomes.

Despite the success of conventional methods and non-surgical management approaches in preserving the natural state of tooth [3-6], dental caries is still widespread and considered as a major public health challenge [7]. The reason behind the ineffectiveness of current standard of care is the fact that management and treatment of dental caries is most effective when detection is early; yet, current clinical detection methods existing clinical detection methods lack sufficient sensitivity to detect early stages of caries formation.

1.2 Structure of Human Tooth and Early Dental Caries

Tissues that make up the human tooth consist of: enamel, dentin, pulp, and cementum (Figure 1.

1). Enamel is the hardest, thin, and translucent outer covering of the tooth. Enamel is made of 96% inorganic minerals, hydroxyapatite ($\text{Ca}_2(\text{PO}_4)_3\text{OH}$) – a mineral made of crystalline calcium phosphate [8]. Inter-crystalline gaps also known as micro-pores in the enamel are positioned between enamel crystals and are equipped with water and organic material to separate these enamel crystals from each other. The thickness of enamel varies over the surface of the tooth with thickest at the cusp of the tooth (occlusal surface of the tooth) and thinnest at the cemento-enamel junction (CEJ). Tooth surface on the same side of a neighboring tooth is called a proximal surface. Due to semi-translucent nature of enamel, the color of enamel/teeth varies from white to yellow to gray.

Dentin is a mineralized, elastic, yellowish-white, avascular layer underlying the enamel that supports the enamel, and compensates for enamel brittleness due to its high mineral content [8]. Dentin contains microscopic channels called dentin tubules and when the enamel is damaged it becomes sensitive to heat or cold and cause sensitivity or pain. Dentin is capable of repair because cells in the pulp can be stimulated to deposit more dentin.

Pulp is a soft living inner structure of teeth. Blood vessels and nerves run through the pulp of the tooth. Cementum is a layer of connective tissue that binds the roots of the teeth firmly to the gums and jawbone [8]. Cementum covers the roots of the teeth and is an avascular mineralized connective tissue. Dental enamel junction or DEJ is a boundary between the enamel and the underlying dentin that form the solid structure of a tooth [8].

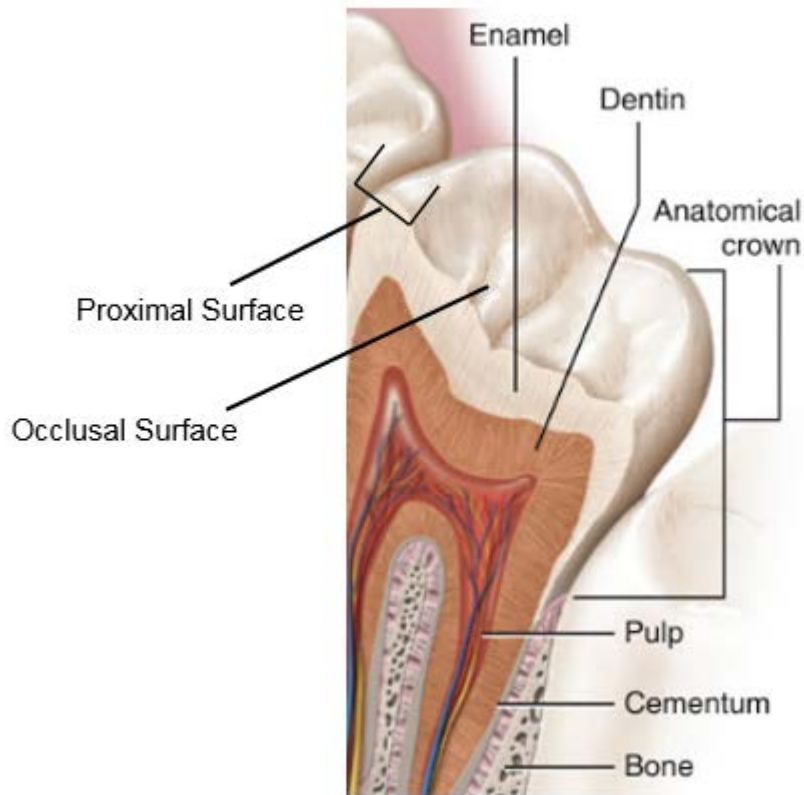


Figure 1.1: The tooth and its supporting structure [8], Copyright 2017, Elsevier Health Sciences.

1.3 Mechanism of Caries Formation

Dental caries is a chronic infectious disease caused by the bacterial deposits known as plaque in dental biofilms which produce acids when digesting the carbohydrates in foods. The production of acid causes the plaque pH to fall below 5, resulting in demineralization of hydroxyapatite crystals in the outermost layer of the tooth (i.e., enamel). The plaque remains acidic for some time, taking 30-60 minutes to return to its normal pH (in the region of 7) by saliva and therefore, increasing the pH, reversing the chemical reaction and yielding remineralization. Over time, the demineralization and remineralization cycles occur periodically (Figure 1.2) and when the net demineralization rate exceeds that of remineralization, the net effect is the loss of minerals and thus creation of early dental caries [3].

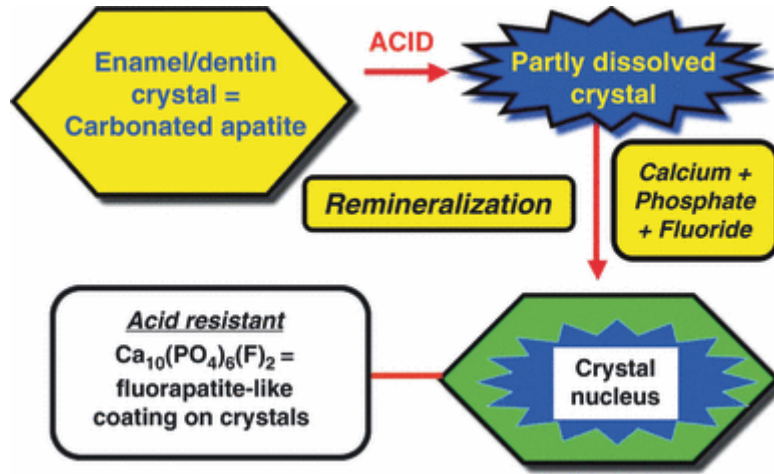
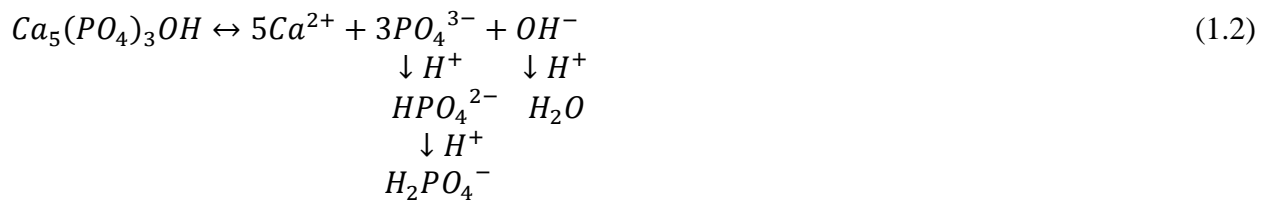


Figure 1.2: Demineralization and remineralization of tooth [3], Copyright 2008, Australian Dental Association.

The interaction of micro-pores with hydroxyapatite crystals of enamel causes the water in the micro-pores to be saturated with respect to hydroxyapatite [9]:



where $K_{SP(HA)}$ represents the solubility product of hydroxyapatite at 37°C. The pH of the water in which hydroxyapatite and calcium phosphate dissolves has an impact on their solubility. The reaction in (1.1) shows that dissolution of hydroxyapatite stops when PO_4^{3-} , OH^- , and Ca^{2+} accumulate in solution. On the other hand, when acid from plaque is added, PO_4^{3-} ions and OH^- ions form HPO_4^{2-} ions and H_2O , respectively, causing a proportion of PO_4^{3-} and OH^- ions to be removed:



In an event of demineralization (reaction in 1.2), mineral from surface of hydroxyapatite is removed and is dissolved in the solution up to a saturation point in order to compensate for the

lack of ions in the solution. For remineralization of dental enamel, the pH of the solution must be raised along with addition of calcium and/or phosphate to the solution [9].

Figure 1.3 shows radiograph images of cross section of slices of sound and carious enamel. Healthy enamel as shown in Figure 1.3(a) shows no loss in mineral content along the thickness of enamel. Early caries, however, is a subsurface region of high porosity protected by thin intact and mineralized enamel surface (shown in radiograph image of Figure 1.3(b)). By being in direct contact with saliva, this surface is resilient to being dissolved by acids [11]. If the early caries is not treated, at this crucial early stage, the demineralization will continue and the thin layer will break which yields irreversible conditions such as cavities which are permanently damaged areas in tooth and require surgical intervention.

However, early dental caries have the potential to be stopped (i.e. arrested caries) or even reversed (i.e., healed/remineralized) through preventive actions such as oral hygiene counseling or fluoride therapy [11]. From this description it becomes obvious that the formation of the biofilm and its metabolic activity cannot be prevented, but disease progression can be stopped or even reversed so that a clinically visible lesion never forms or alternatively, the process can be arrested (become inactive). Therefore, early clinical detection and monitoring is an essential step in dental caries management [11].

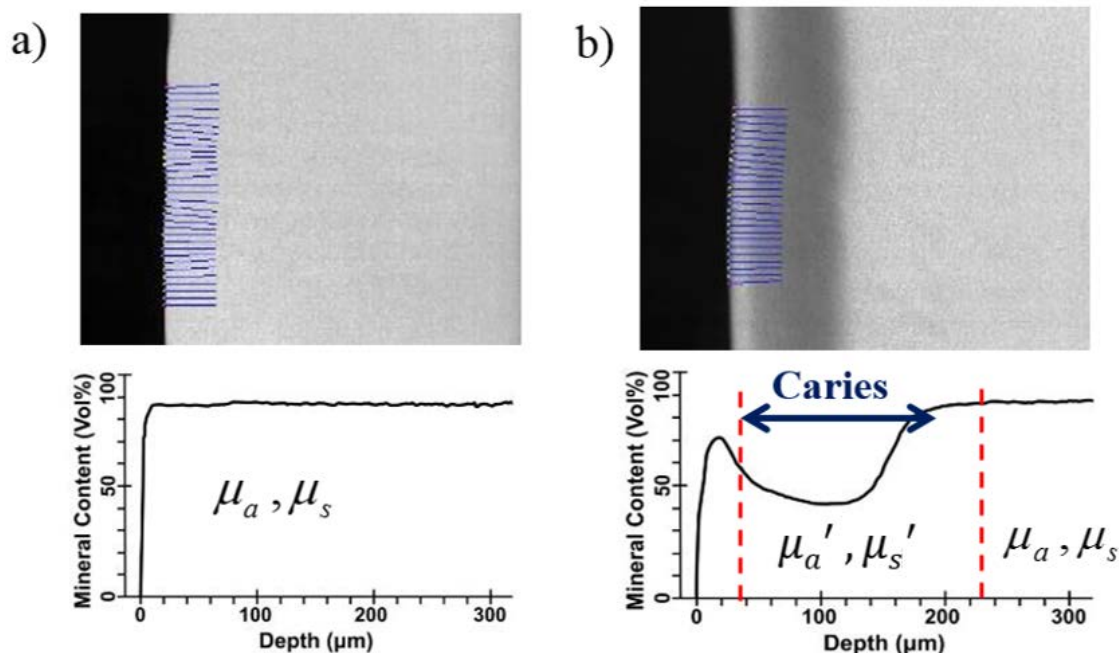


Figure 1.3: a) Radiographic image of the cross section of a slice of healthy enamel and its transverse micro-radiography mineral profile, b) radiographic image of the cross section of slice of carious enamel and its transverse micro-radiography mineral profile. μ_s and μ_a represent the scattering and absorption coefficients of sound region of enamel, respectively. μ_s' and μ_a' are the scattering and absorption coefficients of the early carious region in enamel, respectively.

1.4 Classification of Caries

The International Caries Detection and Assessment System (ICDAS) is a popular classification technique for dental caries based on visual inspection [12].

The criteria consist of seven scores [12]:

0= Sound

1= First visual change in enamel (seen after air drying)

2= Distinct visual change in enamel

3= Localized enamel breakdown (without clinical visual signs of dentinal involvement)

4= Underlying dark shadow from dentine

5= Distinct cavity with visible dentine

6= Extensive distinct cavity with visible dentine involving more than half the dentin

The most desirable detection tool is the one that has the detection threshold of code 1 (or less) that allows for non-surgical, preventive treatments which if successful, should arrest or even remineralize the carious lesion. The reason behind ineffectiveness of current preventive practices in Dentistry is the fact that the success of therapeutic techniques in stopping the progression of dental caries to cavities strongly rely on detection of caries at the very early stages of formation [13]. X-ray imaging and visual-tactile inspection are the conventional examination methods widely adapted in dental clinics for detection of different stages of dental caries. However, studies based on these methods often show an overall low sensitivity and high specificity which means that a large number of lesions may be missed, especially those at clinically challenging surfaces such as occlusal and proximal. They are also limited in their detection threshold, and their ability to detect early caries lesions is poor. That is, approximately, 30%–40% mineral loss is necessary before an enamel carious lesion is visible radiographically [14] at which point the chances of arresting or remineralizing the caries is very unlikely. Therefore, dentistry is shifting to a focus on model of early caries diagnosis and management. Early noninvasive caries detection will shift dentists' traditional reactive approach-drilling and filling- to preventive dentistry-healing caries at early stages. That is why development of sensitive dental diagnostic modalities capable of detecting early caries has been the focus of many researchers in past decade. Among these technologies, optical diagnostic methods have been most notable in terms of their sensitivity in detection of early stages of caries due to their intrinsic ability to probe very small changes in enamel optical properties such as light absorption or scattering.

1.5 Light-Tooth Interactions

Light-tooth interactions can be classified into reflection, transmission, scattering, and absorption. From an optics point of view, dental caries enhance both light absorption and light scattering [15]. Optical properties of the carious and sound enamel suggest that absorption and scattering coefficients of carious enamel are significantly higher than those of intact enamel. Light scattering occurs when photons change direction without any change in their energy. Absorption of light takes place when the photon energy is converted to internal energy (i.e. heat) or partially converted to heat along with the emission of photons of lower energy. Since at early carious lesion there is mineral loss (i.e. substitution of hydroxyapatite crystals with micro-pores) close to the surface of enamel, this leads to creation of micro-pores and, consequently, results in a high amount of optical scattering as well as optical absorption [15]. To characterize the optical properties of tissues, parameters such as scattering (μ_s) and absorption (μ_a) coefficients are incorporated which refer to the average number of scattering and absorption events per propagation unit length of a photon [15-17]. Accordingly, the total light attenuation coefficient can be formulated as $\mu_t = \mu_a + \mu_s'$ in which reduced scattering coefficient ($\mu_s' = \mu_s (1-g)$) can be regarded as an effective isotropic scattering coefficient that represent the cumulative effect of several forward scattering events. Here g is the average cosine of the scattering angles and a measure of medium anisotropy. The total attenuation coefficient is an essential parameter in determining the total optical penetration depth [15-17]. Tooth is considered a turbid medium due to its highly random and scattered propagation of light and the amount of scattering is a function of photon energy. That is, high energy photons (shorter wavelengths) are scattered more and cannot penetrate deep into the tooth. Since the scattering properties of a tooth at near-infrared wavelengths is highly forwarded ($g \approx 1$), photons can reach the structure of tooth from enamel to

dentin [15]. While light scattering is an important parameter which can be studied to identify the presence of early caries, light absorption is another interesting optical properties to explore for caries detection. Direct consequence of absorption of light photons is generation of heat. Therefore, absorption of light by caries produce thermal signatures known as photothermal responses which can be detected in various ways such as infrared radiation (i.e., radiometry). As such, effective detection of caries through optical signatures requires careful selection of excitation and detection wavelengths. Literature suggest that near-infrared wavelengths (700 nm to 1400 nm) is a suitable choice for excitation range of the source (i.e. laser) to create optical contrast between healthy enamel and caries with minimal interference from water [18]. Table 1.1 lists optical absorption and scattering coefficients for sound and carious enamel at select wavelength [17].

Table 1.1: Absorption and scattering properties of sound and carious enamel at select wavelengths [17]

Wavelength (nm)	Absorption coefficient $\mu_a (m^{-1})$	Scattering Coefficient $\mu_s (m^{-1})$
Sound Enamel		
543	<100	10500
600	<100	3,300-7000
633	40-97	110-6600
700	<100	2,700-5,500
800	<100	3,300
1053	<100	1,500
Cariou Enamel		
600	-	55,000
633	-	32,000-157,000

For radiometric detection of light absorption thermal responses, mid (3-5 μm) or long (8-14 μm) wave infrared ranges are often utilized. However, literature suggests the 8-14 μm long-wave infrared range offers better isolation of conductive thermal responses from direct radiative responses (Figure 1.4) [18].

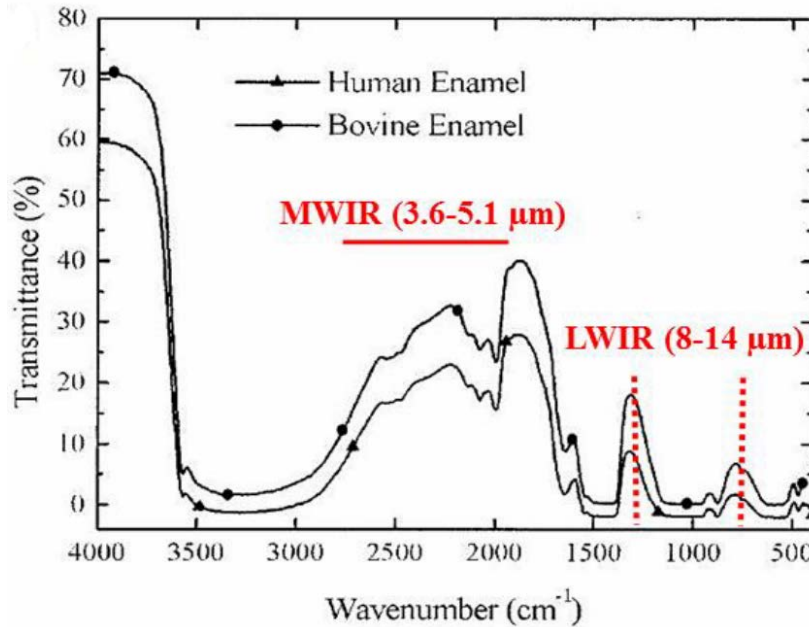


Figure 1.4: Enamel infrared transmission spectrum [19], Copyright 2003, Marcel Dekker.

1.6 Existing Optical Methods

As mentioned earlier, existing clinical caries inspection methods such as x-ray imaging lack sufficient detection sensitivity that is required for early detection and monitoring of dental caries. To address the shortcomings, several optics-based caries detection methods have been developed. Unlike x-ray imaging modalities, which are carcinogenic and may cause molecular changes in biologic systems [20], optics-based technologies use non-ionizing laser light that is not only safe for tissue but also very sensitive to small changes in tissue properties [21]. Moreover, these systems are non-invasive as the generated temperature gradients are not strong enough to induce permanent damage in biological tissues [21]. The detection mechanism of

majority of optics-based technologies rely on enhancement of light scattering in early carious lesion while few of them operate based on enhancement of light absorption in early caries.

Fiber-optic transillumination (FOTI) [22-24] is an imaging method that incorporates a narrow beam of bright white light to illuminate the translucent structure of tooth. At demineralized areas of tooth, the light beam gets scattered thereby producing shadows (Figure 1.5) [22]. A study by Bader *et al.* [24] commented on high specificity and low sensitivity of FOTI for identifying caries due to the obscuring effect of signal branching from healthy tissues surrounding the lesion [22, 24]. The shallow penetration due to absorption of visible light as well as placement of fiber optic light at various angles and distances to the suspected teeth may also effect the results.



Figure 1.5: Caries on occlusal surface by FOTI are shown by arrows [25], Copyright 2006, Elsevier.

Working under the same basis as FOTI, near-infrared (NIR) transmission uses near-infrared light to penetrate in enamel with minimal attenuation in the NIR region [26]. In a study by Chung *et al.* [27], longer NIR wavelengths showed better performance for occlusal surface caries lesions, with 1300 nm representing an overall optimal imaging wavelength as it sets an intrinsic difference between enamel and water attenuation. An advantage in using NIR transmission is that parameters such as NIR wavelengths, light angles, and illumination positions can all be adjusted for various depth of visualization of caries and other features. NIR is also insensitive to

surface deposits such as stain [27]. The major limitation of NIR transmission is poor specificity for detection of early caries which is rooted in the fact that in scattering-based methodologies the signal baseline created by healthy regions overlaps with the small signal increase at early caries sites.

Another category of optical diagnostic methodologies is known as the energy conversion technologies which operate based on transformation of optical energy to other energy forms. Quantitative light-induced fluorescence (QLF) is one such method which uses light-to-fluorescence conversion and the decrease in fluorescence transmission due to increased scattering from demineralized spots as a source of contrast (Figure 1.6). In QLF, mineral content is proportional to the emitted fluorescence in which demineralized areas appear darker than healthy regions [28]. However, QLF's sensitivity to masking effects of plaque or stains and proper cleaning of tooth surface hinder the applicability of this technique in clinical scenarios [28]. The degree of dehydration of tooth tissue also influences the fluorescence intensity measured [29].

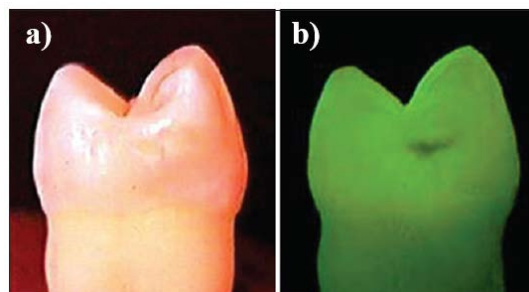


Figure 1.6: a) tooth with caries b) fluorescence image show caries as dark areas [30], Copyright 2009, American Institute of Physics.

DIAGNOdent is a diagnostic aid tool for diagnosis and monitoring of caries especially hidden occlusal caries [31-33]. The light probe scans the tooth with diode laser of 655 nm wavelength. With carious lesions emitting more fluorescent light compared to sound regions, this results in

elevated scale and digital readout in an audible signal readings of the DIAGNOdent [34]. One major limitation of the device is its accuracy in relation to the number shown by the DIAGNOdent and depth of the decay [31-33]. Also, due to high probability of false positives in the diagnosis, the use of DIAGNOdent is recommended in combination with other techniques [31].

Optical coherence tomography (OCT) and thermophotonic lock-in imaging (TPLI) are other emerging caries detection technologies based on light scattering and absorption, respectively. Since these two technologies offer unique advantages over other optical caries detection techniques, they have recently gained popularity in the field of Dentistry.

1.7 Optical Coherence Tomography (OCT)

Optical coherence tomography is a promising non-invasive and non-contact optical imaging modality capable of providing 3-dimensional sub-surface morphology of biological tissue microstructure with micron-scale resolution [35]. OCT is analogous to ultrasound imaging but uses infrared light instead of sound. In ultrasound, transducers can directly detect the backscattered sound. In OCT, however, the distance between optical reflections from different layers of tissue is measured through interferometry by retrieving the time delay of the light reflected from optical interfaces (A-scan) through Fourier transformation. A series of A-scans along a line on sample surface creates cross-sectional or B-scan images, while scanning the sample surface in two dimensions provides volumetric data (Figure 1.7) [35].

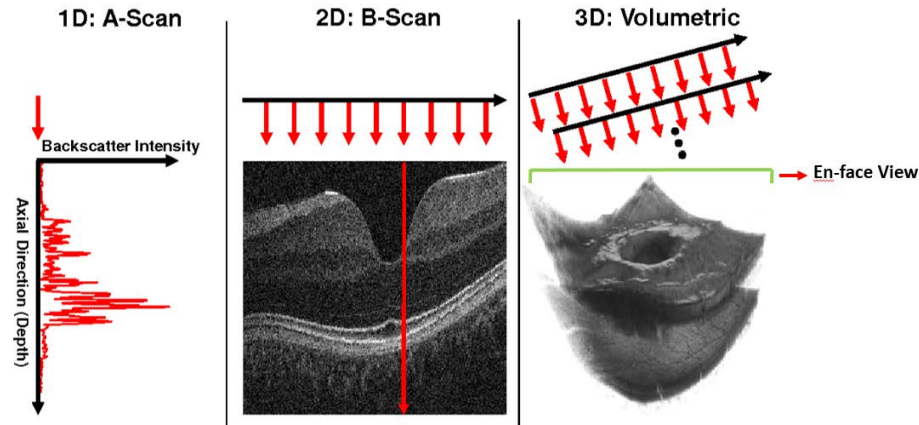


Figure 1.7: OCT scanning coordinate system [35], Copyright 2012, Optical Society of America.

Owing to the ability of OCT to provide high-resolution 3-dimensional images, OCT has recently gained popularity in Dentistry research for diagnosis and screening of dental diseases and oral cancer [36-41]. Otis *et al.* [42] presented the first in vivo OCT images of human dental tissues. They obtained a smaller but deeper (3 mm) tooth image. Knowing that caries detection at early stages of demineralization is challenging, Figure 1.8(a) shows OCT images of carious lesions on a smooth tooth surface, where demineralization can be seen visually as white spot lesions on dried enamel surfaces (ICDAS II Code 2) [41]. Since demineralization/porosity increases the light back scattering intensity, the carious lesion shows as a bright area with higher contrast in the OCT image (Figure 1.8(b)). Similar results are seen in occlusal surface caries (Figure 1.8(c)-(d) white arrows) which shows the bright and higher contrast areas as carious lesions. OCT can also be applied for detection of cracks [35, 41]. The yellow arrow in Figure 1.8(d) shows an enamel crack. Cracked teeth may lead to tooth loss if there is no treatment intervention.

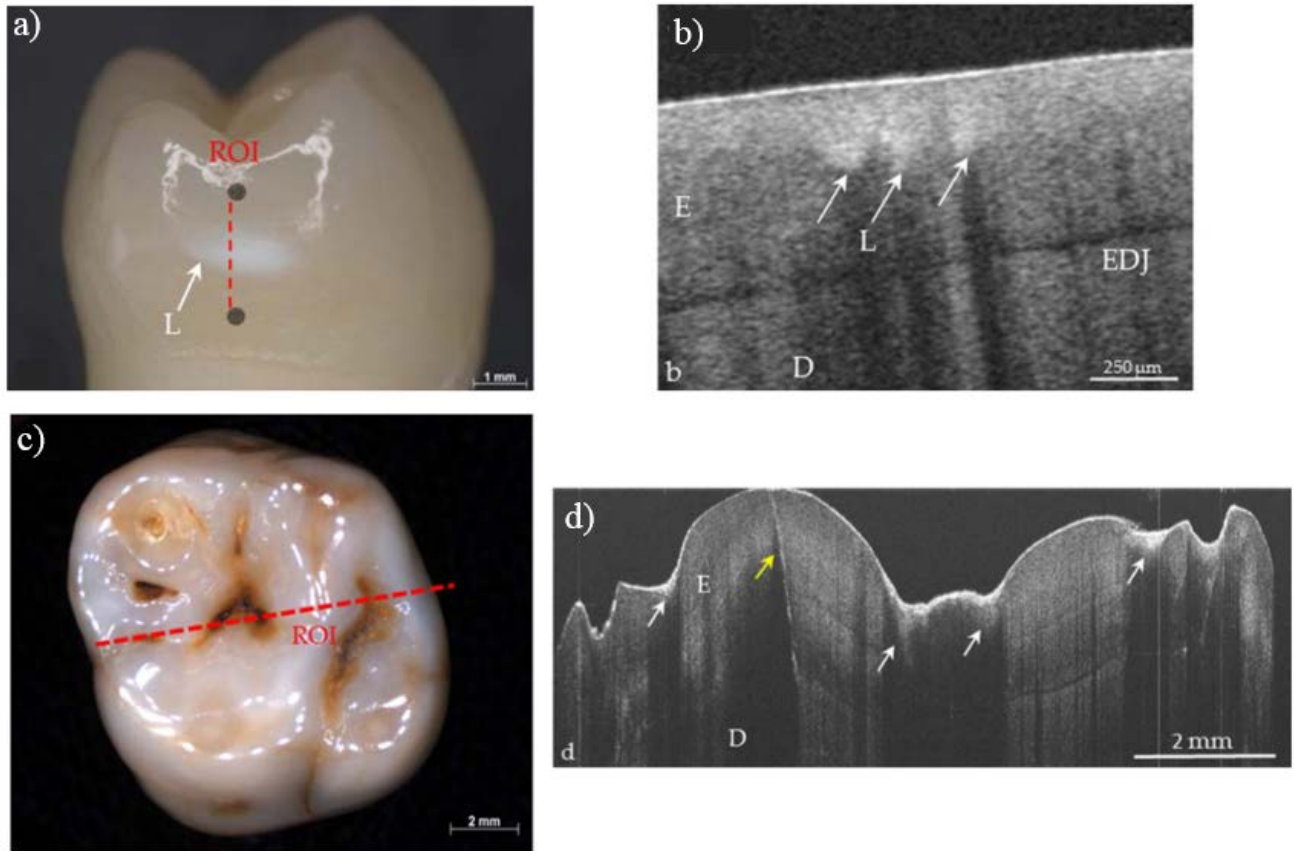


Figure 1.8: (a) Tooth with smooth surface caries (L) of (ICDAS II) Code 1. The dashed red line shows the region of interest (ROI) and the caries is visually seen after drying; (b) OCT image of smooth surface caries at ROI, bright shadowed spots show the carious/demineralized lesion (white arrows); (c) Tooth with occlusal surface caries (ICDAS II Code 2); (d) OCT image showing the ROI with caries lesions (white arrows) showing as bright areas and enamel cracking (yellow arrow). E: enamel, D: dentin, EDJ: enamel-dentin-junction [41], Copyright 2017, H. Schneider *et al.*

To assess various types of enamel lesions *in vivo*, a study by Espigares *et al.* [37] compared OCT with micro-focus x-ray computed tomography (μ CT) images, concluding that OCT shows the lesions as areas of increased signal intensity and that OCT has great potential to be used in clinical practice for detection and screening of caries. In another study, Shimada *et al.* [38] used OCT for detection of the challenging clinical cases of occlusal caries and reported a superior sensitivity in detection of early caries on occlusal surfaces using OCT over the existing clinical

modalities of x-ray imaging and visual/tactile inspection. Due to shallow imaging depth of the system (~ 1-2mm), however, other diagnostic imaging modalities have to be used for diagnosis of more advanced caries. While A- and B-scan OCT images were studied in these dental OCT works, Sinescu *et al.* [39] used *en-face* OCT images to examine the material defects of dental prostheses as well as micro-leakages at prosthetic interfaces. En-face imaging (shown in Figure 1.7) allows for production of transverse or front section images for a fixed path length difference [43]. *En-face* OCT imaging appears to be an optimal option for delivering the complex tomographic information of OCT [39]. In addition to caries and crack detection, a study by Tsai *et al.* [36] showed that OCT provides high resolution pathological information for an effective diagnosis of oral cancer at its early stages and detection of oral squamous cell carcinoma.

Another major advancement in the field has been the introduction of cross-polarization OCT (CP-OCT) by Fried *et al.* [40, 44-46] for elimination of the obscuring effects of surface Fresnel reflections and thus more reliable quantification and monitoring of various stages of carious lesions. Polarization sensitive OCT (PS-OCT) has also been utilized for imaging composite restorations and mineralization defects [47-49]. The additional contrast channels offered by PS-OCT, such as depolarization and retardation [50], are believed to have better linkage to the mineralization status of dental hard tissues compared to the reflectivity profiles of conventional OCT. However, conventional OCT and CP-OCT are still mainstream in dental OCT research mostly due to the complexities associated with instrumentation and data processing of PS-OCT data as well as the additional instrumentation cost of PS-OCT.

Despite the wealth of information provided by dental OCT studies, correlation of findings among studies has proven to be quite challenging, especially for detection of early dental caries. This is mostly due to two fundamental inconsistencies in the design of experiments: First, most studies

report performance parameters (e.g., sensitivity, specificity, etc) by studying natural caries (i.e., unstandardized samples) which introduces a significant degree of variability in studied samples as optical properties of tooth and its susceptibility to demineralization are multifactorial phenomena, being function of parameters such as a patient's oral health status, diet, ethnicity, etc. Second, most studies base the early caries detection criteria on the contrast obtained between the suspected early caries lesion and the healthy areas at its immediate proximity as opposed to a more global reference such as the contrast between suspected lesion and the healthy areas on the whole surface of the tooth. Due to these inconsistencies, variations in terms of sensitivity and specificity of OCT to early stages of caries formation are found in the literature with an overall observation of better sensitivity of OCT compared to radiography but no significant difference in specificity for early detection of caries at challenging surfaces such as proximal [51].

1.8 Thermophotonic Lock-in Imaging (TPLI)

While OCT provides a three dimensional map of light-reflecting interfaces in biological tissues such as micro pores introduced by demineralization in a tooth, light absorption-based technologies such as thermophotonic imaging (TPI) produce a map of subsurface features absorbing the specific incident laser radiation (e.g., calcium and phosphate as the byproducts of demineralization). TPI is a non-destructive testing technology that performs diagnostic imaging using infrared cameras, therefore a thermography technique [52]. Most of the applications of thermography are passive; for example, imaging of temperature differences in parts and structures (e.g., heat losses in buildings) or biological tissues (e.g., skin temperature mapping). In active thermography, on the other hand, an energy source (e.g., laser) is introduced to the system to produce a thermal contrast between the feature of interest and the background in a controlled manner [52]. That is, an intensity modulated light source (e.g., laser) is utilized to induce heat

periodically while the local surface temperature modulation is captured by an infrared camera [53]. In this arrangement, presence of subsurface defects (e.g. early caries), alters the registered surface temperature profiles that the IR camera captures, thus creating a contrast between the intact and defective regions. One example of active thermography is thermophotonic lock-in imaging or TPLI [52, 53], in which the altered surface temperature profiles are revealed through the lock-in demodulation signal processing algorithm. In TPLI, the role of lock-in modulation is to only evaluate the alternating (ac) part of the detected signal which carries information from subsurface inhomogeneities [54]. That is, subsurface defects alter the local centroid of the thermal wave field, leading to a phase delay as well as change in the amplitude of the ac radiometric detected signal by the IR camera. As such, lock-in demodulation of the thermophotonic signals lead to calculation of phase and amplitude images with respect to the reference signal (i.e., optical excitation modulation signal) [18]. Therefore, by changing the modulation frequency, the contrast in thermophotonic lock-in phase images and detection of inhomogeneities at short subsurface distances can be adjusted [54].

Lock-in thermography is a popular non-destructive testing technique which has predominantly been used in industry for interrogation of manufactured parts and industrial samples such as detection of fatigue cracks in structures [55] or defective aerospace component [56]. Among the first studies incorporating lock-in thermography for medical diagnosis were the ones conducted by John and Salerno [57] and John *et al.* [58]. They examined the ground section of a resin-embedded extracted human tooth using modulated optical excitation and lock-in thermography. However, the result of their study was limited only to estimation of the relative thermal thickness of dental samples. In a more recent study, applications of lock-in thermography in Dentistry has also been recognized and investigated. Tabatabaei *et al.* [59] incorporated lock-in thermography

for the first time for imaging of early stages of demineralization in dental tissues using a mid-wavelength infrared (MWIR) camera. The study established a long term strategy for detecting early dental caries and its diagnostic outperformance over other emerging technologies such as polarized Raman spectroscopy [59]. Ojaghi and Tabatabaei [60] demonstrated diagnostic imaging of early caries using lower-cost and passively cooled long-wave infrared cameras (LWIR) [59, 60]. Our group's most recent work in this area demonstrates feasibility of detecting early dental caries using a cellphone attachment infrared cameras which cost as low as ~\$250, opening the door for commercialization and translation of the TPLI technology to Dentistry as an inexpensive end user product [61]. Figure 1.9 shows the obtained results from artificially-induced caries on a smooth surface of a tooth using a cellphone camera. Caries are seen as a higher contrast area in both amplitude and phase images (Figure 1.9(b)-(c)) which manifests that the demineralization process has enhanced absorption of light with generation of larger amplitude thermal waves. TPLI has also been utilized in Dentistry research for applications other than early caries detection. Streza *et al.* [62] performed a comparative study between lock-in thermography and optical microscopy to examine adhesion between dental fillings and the dental hard tissue. The outcome of the study demonstrated that lock-in thermography has superior photothermal contrast in the presence of micro-gaps and testing of dental interfaces where optical microscopy showed no defects at the enamel interface [62].

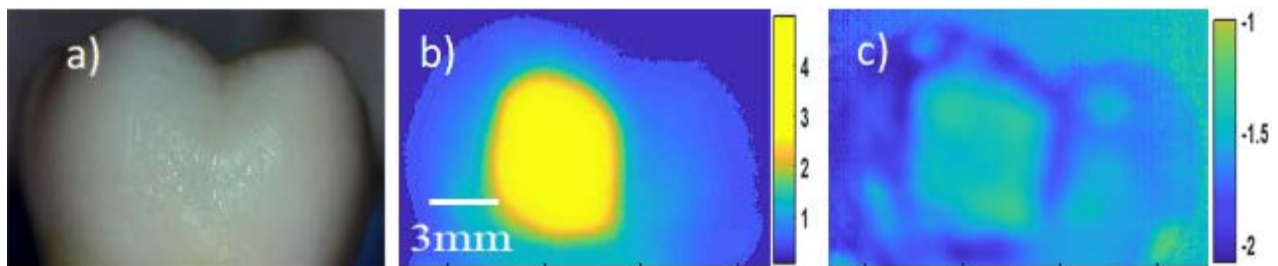


Figure 1.9: (a) Photograph of the sample along with (b) amplitude and (c) phase images of tooth with artificially-induced caries [61], Copyright 2018, American Institute of Physics.

1.9 The Objectives and Outlook of the Thesis

In past two decades, researchers have made significant progress in the development and validation of early caries detection modalities. Yet, minimal research effort has been focused on objective comparison of the basic capabilities of scattering-based and absorption-based contrast mechanisms such as detection specificity. The above review of literature suggests that both OCT and TPLI (as representative techniques based on light scattering and absorption, respectively) have the promise of detecting caries at early stages of formation when preventive measures can be utilized to not only arrest the caries lesion but also heal it through remineralization therapeutic techniques. As such, in this thesis, we report on a systemic comparison of OCT and TPLI while identifying the advantages and limitations of each technique in detecting artificially-induced/standardized early dental caries. Based on the outcome of the comparative study, we then suggest an optimum diagnostic imaging modality (known as Truncated-Correlation Photothermal Coherence Tomography (TC-PCT) system) and present preliminary imaging studies with the TC-PCT technology, paving the way for further development of an optimal early caries detection technology.

Since the first phase of the thesis involves OCT and TPLI imaging, Chapter 2 presents the theoretical background of the two systems in detection of caries.

Chapter 3 describes the instrumentation and methodologies used in this thesis. Moreover, in this chapter, the procedure for sample and acidic gel preparation are described.

Chapter 4 discusses the outcomes of the comparative study between TPLI and OCT on early caries detection, justifying the need for an optimum detection technology (i.e. truncated

correlated tomography or (TC-PCT) which offers the advantage of both OCT and TPLI with minimal compromise.

Chapter 5 presents the theory, instrumentation/method and preliminary imaging studies using TC-PCT, establishing feasibility of performing tomographic imaging of early caries and dental defects based on absorption of light.

Chapter 6 brings together the conclusions of the research presented in this thesis and recommends future directions.

Chapter 2

Theory

This section presents the basic theoretical background of TPLI and OCT. Through simulation, the expected theoretical trends and outcomes have been presented and discussed in order to gain better understanding for interpretation of experimental results as well as to justify selection of OCT and TPLI for the comparative study.

2.1 Caries Detection in Long Wave Infrared Thermophotonic Imaging

The light-matter interaction in dental hard tissue is governed by coupled diffuse-photon-density and thermal-processes. The presence of caries increases the optical scattering and absorption resulting in generation of subsurface modulated thermal fields (aka thermal waves) which contribute to the spectrum of the radiometric signal captured on the sample surface as [54, 63]:

$$S(l, t) \propto \bar{\mu}_{IR} \int_0^l T(z, t) \exp(-\bar{\mu}_{IR}z) dz \quad (2.1)$$

where $\bar{\mu}_{IR}$, l , and $T(z, t)$ are the average IR absorption coefficient over the detection/IR camera wavelength range (LWIR: 8-14 μm), absorber depth, and the induced thermal-wave field, respectively. That is, the radiometric signal receives contributions from the thermal-wave field in the form of an exponentially attenuated depth integral, with $\bar{\mu}_{IR}$ serving as the attenuation coefficient.

To gain better understanding of TPLI responses in a tooth, light absorption by dental caries can be modeled as one dimensional collimated beam entering a turbid medium which is then absorbed at depth $z=l$ after attenuation in the turbid medium due to the absorption and scattering in healthy enamel [64] [18], Figure 2.1.

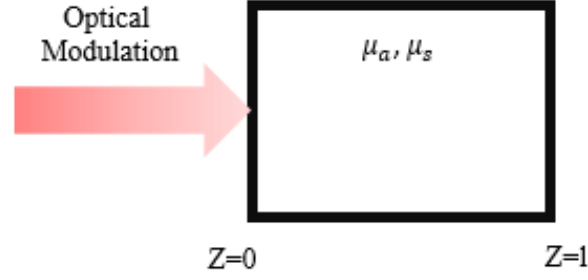


Figure 2.1: Light absorption in a turbid medium

The frequency-domain thermal-wave problem for such method can be formulated by considering a depth dependent source term to the heat diffusion differential equation as well as an attenuated heat source at $z=l$ through a boundary condition [64] [18]:

$$\begin{cases}
 \frac{\partial^2 \theta(z; \omega)}{\partial z^2} - \sigma^2 \theta(z; \omega) = -\frac{\mu_a}{k} I(z) F(\omega) \\
 -k \frac{\partial \theta(z; \omega)}{\partial z} \Big|_{z=0} = 0 & \text{(I)} \\
 -k \frac{\partial \theta(z; \omega)}{\partial z} \Big|_{z=l} = I(l) F(\omega) & \text{(II)} \\
 \theta(z; \omega) = \mathfrak{T} \{ T(z, t) - T_\infty \}
 \end{cases} \quad (2.2)$$

where k , μ_a , T_∞ and $F(\omega)$ are thermal conductivity, absorption coefficient, sample equilibrium temperature, and the spectrum of the applied optical excitation, respectively. In addition, $\sigma = \sqrt{\frac{i\omega}{\alpha}}$ is the complex wavenumber, where ω and α are laser modulation frequency and thermal diffusivity, respectively. Equation 2.2 is a Fourier-domain representation of the time-domain problem comprising of an ordinary nonhomogeneous differential equation. The spectrum of the radiometric signal can eventually be found as [64] [18]:

$$S_c(l; \omega) \propto \bar{\mu}_{IR} \int_0^l \theta(z, \omega) \exp(-\bar{\mu}_{IR}z) dz = \bar{\mu}_{IR} \left[\frac{A}{\sigma - \bar{\mu}_{IR}} (\exp[(\sigma - \bar{\mu}_{IR})l] - 1) - \frac{B}{\sigma + \bar{\mu}_{IR}} (\exp[-(\sigma + \bar{\mu}_{IR})l] - 1) - \frac{C}{\mu_{eff} + \bar{\mu}_{IR}} (\exp[-(\mu_{eff} + \bar{\mu}_{IR})l] - 1) - \frac{D}{\mu_t + \bar{\mu}_{IR}} (\exp[-(\mu_t + \bar{\mu}_{IR})l] - 1) \right] \quad (2.3)$$

where $\bar{\mu}_{IR}$ is the average infrared absorption coefficient over the detection wavelength range and A , B , C , and D are constants linked to medium thermal properties [9]. The time-domain radiometric signal can then be calculated by taking the inverse Fourier transform of equation 2.3. The time-domain signal is a periodic signal which has an amplitude and an initial phase. Equation 2.4 depicts the mathematical analogue of this signal being processed by lock-in demodulation algorithm for retrieval of amplitude (A) and phase (ϕ) information. In short, the lock-in algorithm mixes the radiometric signal with in-phase, $\sin(\omega_0 t)$, and quadrature, $\sin(\omega_0 t + 90)$, reference signals. The weighted frames are summed and sent to a low-pass filter them to achieve in-phase (S^0) and quadrature (S^{90}) values. Amplitude and phase of radiometric signal is finally calculated using the well-known relationships of complex algebra.

$$\begin{aligned} \begin{cases} \sin(\omega_0 t) \times A \sin(\omega_0 t + \phi) \\ \sin(\omega_0 t + 90) \times A \sin(\omega_0 t + \phi) \end{cases} &\xrightarrow{\text{Mixing}} \begin{cases} \frac{A}{2} [\cos(\phi) - \cos(2\omega_0 t + \phi)] \\ \frac{A}{2} [\sin(\phi) - \cos(2\omega_0 t + \phi + 90)] \end{cases} \xrightarrow[\times\sqrt{2}]{\text{Weighting}} \\ \begin{cases} \frac{A}{\sqrt{2}} [\cos(\phi) - \cos(2\omega_0 t + \phi)] \\ \frac{A}{\sqrt{2}} [\sin(\phi) - \cos(2\omega_0 t + \phi + 90)] \end{cases} &\xrightarrow{\text{LPF}} \begin{cases} S^0 = \frac{A}{\sqrt{2}} \cos(\phi) \\ S^{90} = \frac{A}{\sqrt{2}} \sin(\phi) \end{cases} \rightarrow \begin{cases} A = \sqrt{(S^0)^2 + (S^{90})^2} \\ \phi = \arctan \left(\frac{S^{90}}{S^0} \right) \end{cases} \end{aligned} \quad (2.4)$$

In regions where early caries exist, an increase in amplitude and a change in initial phase is observed compared to intact regions which forms the basis of diagnostic contrast for early dental caries detection with TPLI. To extend the findings from theoretical modelling, opto-thermal

properties of enamel (Table 2.1) can be used to calculate the phase and amplitude of the signals and plot them against absorber/caries depth.

Table 2.1: Optical (800 nm) and thermal properties of dental tissues

	Optical absorption Coefficient, μ_a (m^{-1})	Optical scattering Coefficient, μ_s (m^{-1})	Thermal diffusivity α (m^2/s)	Thermal conductivity κ (W/mk)
Enamel	100	3300	4.7×10^{-7}	1.07

The spatial resolution in thermal-wave imaging systems such as TPLI is defined by half the thermal diffusion length: $\lambda/2 = \sqrt{\alpha/\pi f_m}/2$ where α and f_m denote thermal diffusivity and laser modulation frequency, respectively. But at the same time, the maximum inspection depth is proportional to $1/\sqrt{f_m}$. Therefore, in thermal-wave imaging there is always a compromise between improving the resolution and increasing the inspection depth.

Figure 2.2(a) and Figure 2.2(b) show the simulation results of TPLI amplitude and phase channels at various frequencies. Careful inspection of these plots reveal that at low modulation frequencies, thermal waves can inspect deep into the sample, while high frequency thermal waves are limited to near the surface due to higher attenuation. Moreover, it can be seen that at higher modulation frequencies although inspection depth is significantly reduced, the axial resolution (i.e., slope of lines) is increased. Consequently, the inspection depth and resolution of photothermal systems can be adjusted, based on the thermo-optical properties of the sample, via controlling the modulation frequency. For early detection of dental caries, we have empirically found that modulation frequency of 2 Hz provides a reasonable compromise between resolution and inspection depth. Using this modulation frequency and an average thermal diffusivity of enamel of $2 \times 10^{-7} \frac{m^2}{s}$, the resolution is found as 90 μm .

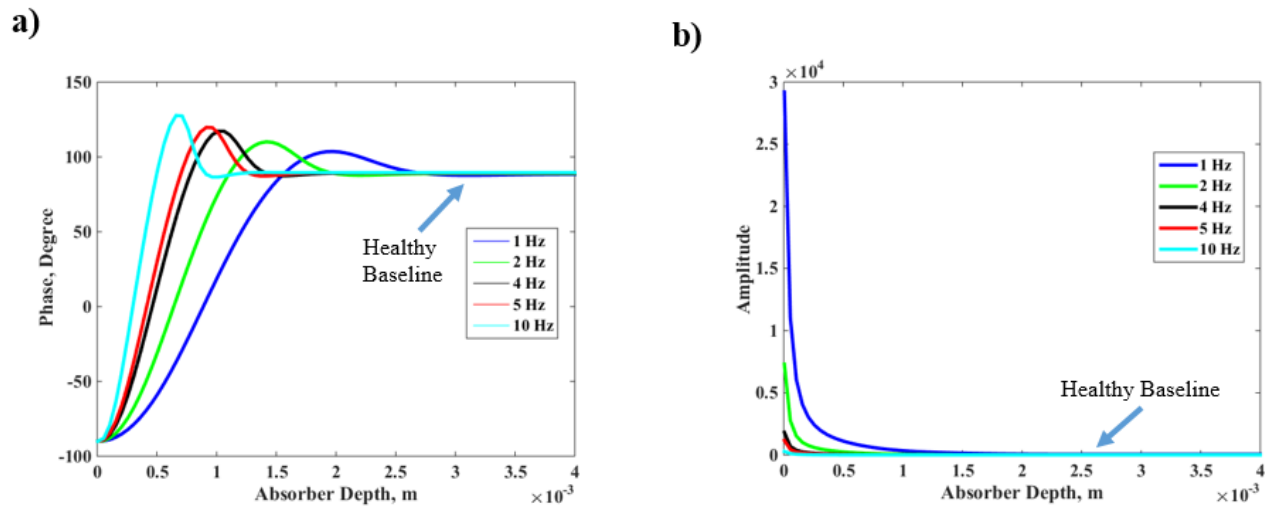


Figure 2.2: Theoretical radiometric signal (a) phase and (b) amplitude vs. absorber depth

Figure 2.3 shows TPLI phase images of an aluminum block which is an opaque sample with defects at several depths [18]. The depth-integrated nature of TPLI shows that high modulation frequencies cannot penetrate deep into the sample resulting in lower detection depth, hence, the fading of the deeper holes.

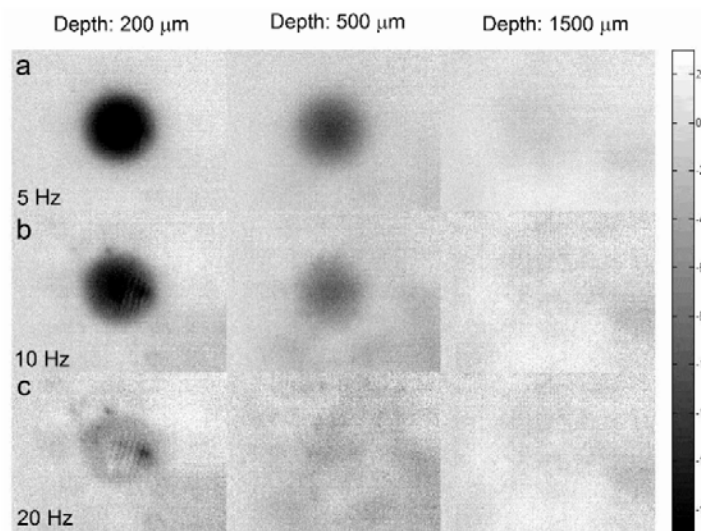


Figure 2.3: Phase images of blind holes at different depths [18], Copyright 2016, Ojaghi.

2.2 Optical Coherence Tomography

OCT measures the intensity of interference between lights received from sample and a reference path and uses it to find depth profiles of back reflecting interfaces in the sample through Fourier transformation. The interference spectrum measured by an OCT spectrometer can theoretically be modeled as [65]:

$$I(k) = I_S + I_R + 2\sqrt{I_S I_R} \cos(2k\Delta L) \quad (2.5)$$

Here I_S , I_R , and ΔL represent sample light intensity, reference light intensity and the path length difference between the back reflected light from sample and reference lights, respectively. In general, $2k\Delta L$ is called the phase shift of the light. By taking the inverse Fourier transform of the Fourier-domain signal (i.e., equation 2.5; the spectrometer signal) one can form depth profiles in which reflecting interfaces can clearly be identified (Figure 2.4). In presence of caries, the depth scan obtained shows greater signal intensity at carious lesion due to larger I_S . Moreover, OCT, unlike TPLI, is a tomographic imaging technology which can discern between reflective regions located at different depths inside sample (i.e., can determine ΔL).

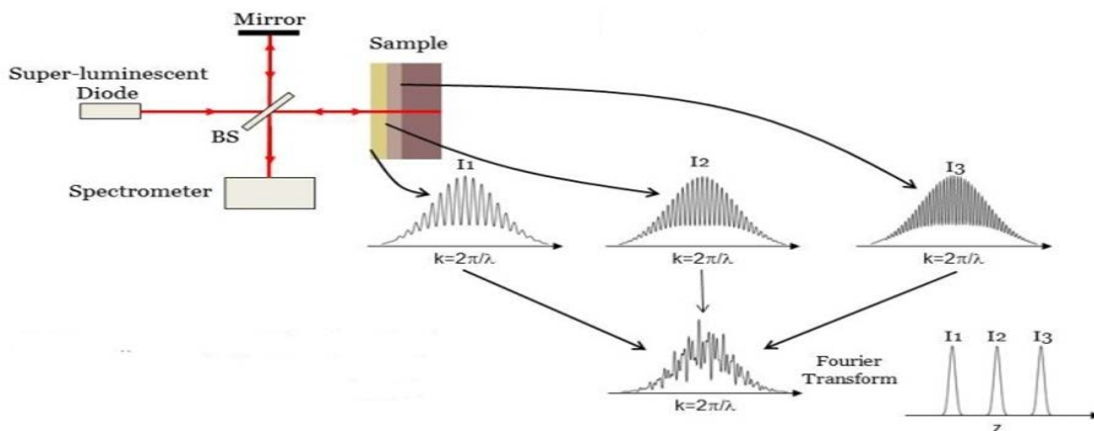


Figure 2.4: The working principle of OCT [66], Copyright 2013, Kozobolis et al.

In low coherence interferometry, the axial resolution for a Gaussian spectrum is given by [65]:

$$\Delta Z = \frac{2 \ln 2}{\pi} \frac{\lambda^2}{\Delta \lambda} \quad (2.6)$$

where ΔZ is the full width at half maximum of the autocorrelation function (axial resolution), λ is the centre wavelength of light, and $\Delta \lambda$ represents bandwidth of light source [65]. Since the axial resolution is inversely proportional to the bandwidth of light, the broad bandwidth could lead to the higher axial resolution [65]. On the other hand, as in microscopy, the lateral resolution depends on light focusing power of objective lens and can be determined by using the following formula:

$$\Delta x = \frac{4\lambda}{\pi} \frac{f}{d} \quad (2.7)$$

here f represents the focal length of objective lens and d stands for spot size of laser beam at back aperture of lens.

The developed OCT system in our laboratory has the center wavelength of light, λ , of 1315 nm, the bandwidth of light source, $\Delta \lambda$, of 115 nm at 3 dB (decibels). Thus, using equation 2.6 the theoretical axial resolution can be calculated as:

$$\Delta Z = 0.44 \frac{(1315)^2}{115} \approx 6.6 \mu\text{m}$$

In order to determine the lateral resolution, equation 2.7 has been deployed. Here, the focal length of sampling lens is 18 μm and d is 3 mm:

$$\Delta x = \frac{4\lambda}{\pi} \frac{18}{3} = 10 \mu\text{m}$$

In experiments, however, axial resolution of OCT system was measured as $\sim 12 \mu\text{m}$ in air and $8.6 \mu\text{m}$ in tissue. While image penetration depth is essential for imaging modalities, intensity of OCT signal lowers along depth due to scattering and absorption of light within the sample.

Figure 2.5 shows the experimental imaging performance of OCT system along depth in a form of sensitivity roll-off plot where optical path length difference between sample arm and reference arm is varied at $254 \mu\text{m}$ step intervals and an intensity depth profile is generated up to 5 mm in air using a mirror as sample. This plot indicates how signal-to-noise ratio (SNR) of interference signal acquired decreases along depth and demonstrates acceptable SNR in our system for interrogation of enamel caries which at the most are expected $1\text{-}2 \text{ mm}$ before the surface.

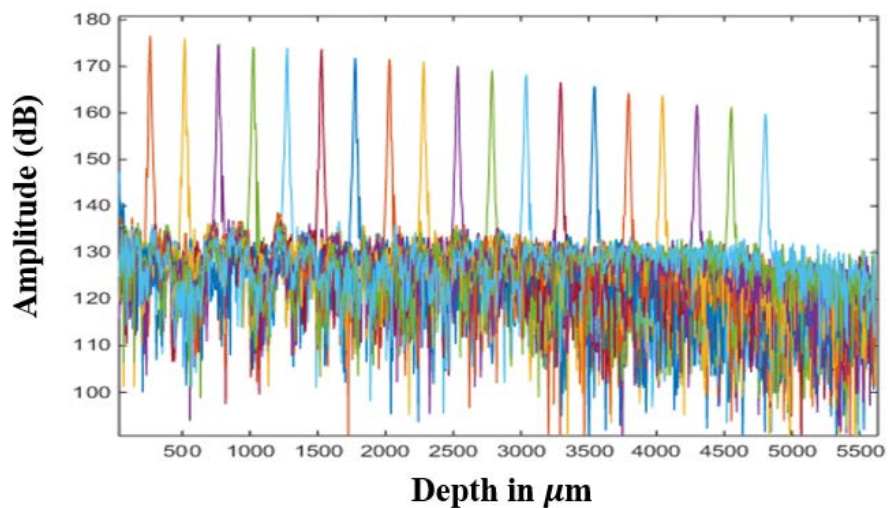


Figure 2.5: Intensity depth profile up to 5 mm in air.

Chapter 3

Materials, Instrumentation, and Methods

This section provides detailed information on the experimental setup and methodologies used in this thesis for OCT and TPLI experimentations. A thorough explanation of data analysis and processing methodologies is also provided. Finally, the preparation of dental samples for controlled demineralization protocol has been explained.

3.1 Thermophotonic Lock-in Imaging System

In TPLI experimental setup, Figure 3.1(a), the excitation source consists of a fiber coupled (multimode; core diameter = 200 μm) continuous wave near-infrared laser (808 nm; Jenoptik, Jena, Germany) which is regulated by a laser controller unit (Ostech, Berlin, Germany) in order to allow for modulation of laser intensity at a given modulation frequency (e.g., $f_m=2$ Hz) and to maintain an average optical intensity of 2 W/cm^2 on the sample surface [59, 60, 67]. Our previous studies on TPLI imaging of early caries suggest $f_m=2$ Hz to yield best compromise between resolution and inspection depth. The 2 Hz laser modulation frequency yields a theoretical resolution of 90 μm in enamel. A long-wave infrared (LWIR) camera (Gobi 640; Xenics, Leuven, Belgium) and frame grabber along with a custom made extension tube and an 18 mm focal-length objective lens (Xenics OPT-000179) are used to obtain a magnification of one from the interrogated surface of the sample. Samples are placed on LEGO blocks and positioned at the focal plane of the camera. The distance between the optical fiber and the sample is adjusted to get a 15 mm diameter beam size on the interrogated surface of the sample.

A multifunctional data acquisition board (National Instruments, Austin, Texas, NI USB-6363 BNC) is used to capture and record the emitted thermal radiation from samples subjected to

intensity modulated laser excitation. The multifunctional data acquisition board synchronously generates three signals: reference pulse train, in-phase, and quadrature reference signals, Figure 3.1(b). The reference pulse train indicates the beginning of each modulation cycle for averaging purposes. The in-phase reference signal is responsible for modulating the intensity of the laser beam. As such, the in-phase reference signal is in-phase with the laser modulation while there is a 90° phase lead between the in-phase and quadrature reference signals. The LWIR camera is focused on the surface of the sample which is securely mounted on a LEGO block. During experiments, camera images are acquired at a maximum frame rate of 50 frames per second while at the same time the values of in-phase and quadrature signals are recorded. Subsequently, the acquired images are weighed and averaged using the instantaneous readings of the two reference signals to yield in-phase (S^0) and quadrature (S^{90}) images [60]. The amplitude and phase for each pixel are then calculated by applying equation 3.1, resulting in calculation of amplitude and phase images, respectively.

$$A = \sqrt{(S^0)^2 + (S^{90})^2} \quad \text{and} \quad \varphi = \arctan\left(\frac{S^{90}}{S^0}\right). \quad (3.1)$$

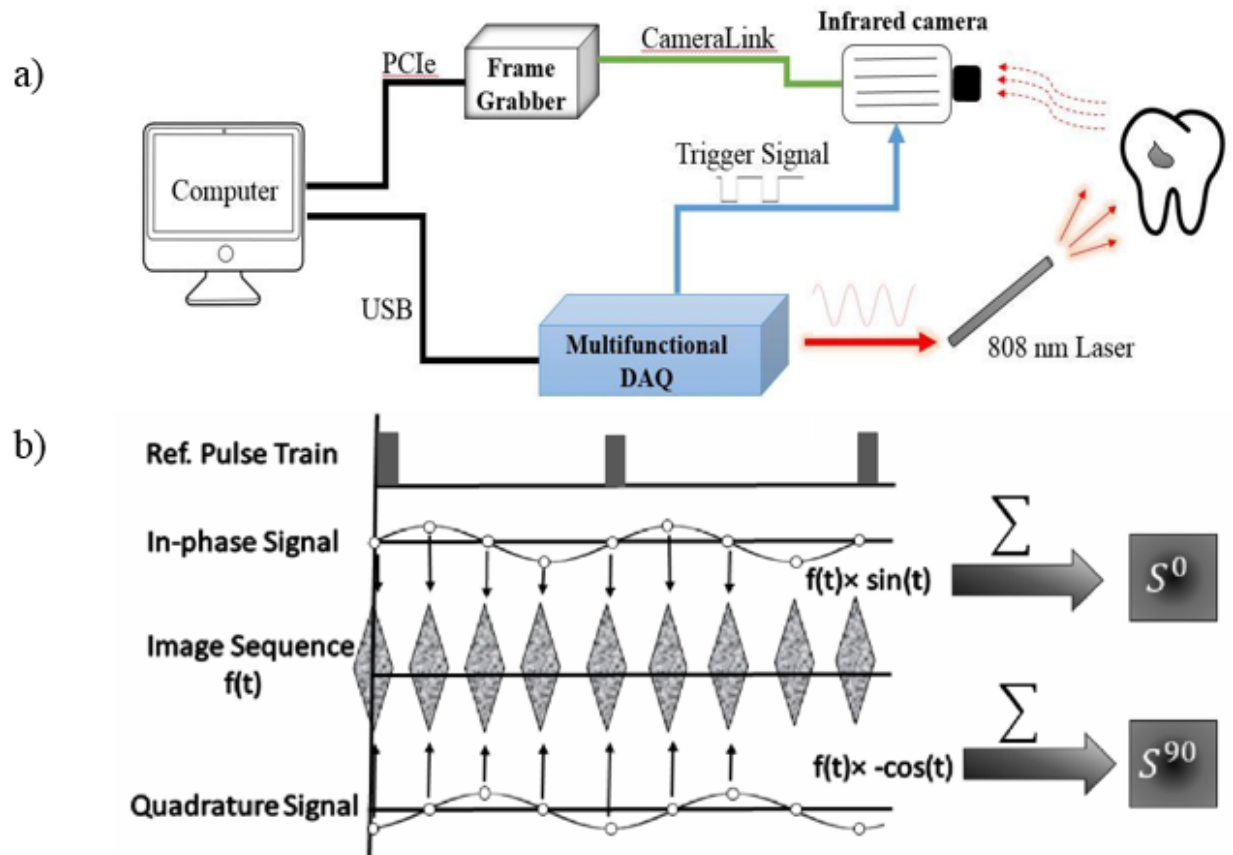


Figure 3.1: (a) Schematic representation of the developed thermophotonic lock-in imaging (TPLI) system. (b) TPLI signal processing [15], Copyright 2012, Nima Tabatabaei.

3.2 Optical Coherence Tomography

Figure 3.2 depicts a schematic of the developed spectral-domain OCT system. The light source is a near-infrared superluminescent diode (Exalos; Switzerland) emitting at 1315 nm with a 115 nm FWHM and a maximal output power of 30 mW. After passing through a fiber coupler, the source light is coupled into a fiber-based Michelson interferometer. The splitting ratio of the 2×2 fiber coupler is 50/50. To minimize reflection signals from samples, a polarization controller is used in the reference arm to adjust polarization to the cross-polarization state. Subsequently, the interference spectrum is captured in the spectrometer by a line scan camera, composed of 2048 pixels, with a maximum scan/acquisition rate of 147 kHz. Optical power at sample is ~7 mW and

the SNR of the built OCT system is measured to be >100 dB. The developed data acquisition and processing program scans the OCT beam along the surface of the sample using the two galvo scanners (GS) and performs the inverse Fourier transform operation on the spectral-domain signals registered by the spectrometer, thus creating 3-D tomographic images of subsurface reflectors (e.g., early caries). The amplitudes of the backscattered light in a form of B-scan (i.e., cross-sectional image) were used for studying the effects of demineralization.

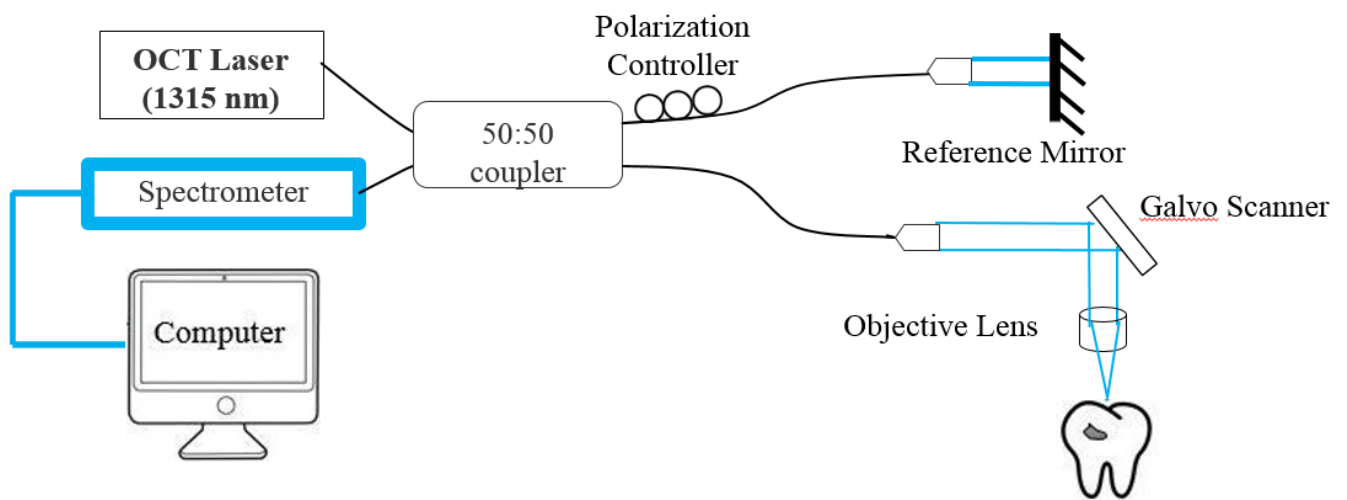


Figure 3.2: Schematic representation of the developed spectral-domain optical coherence tomography (OCT) system. The polarization controller is adjusted to yield interference in the cross-polarization state.

3.3 Micro Computed Tomography

In this study, micro Computed Tomography (Skyscan 1272 high-resolution μ CT system, Bruker MicroCT, Kontich, Belgium) with a camera pixel size of $7.4 \mu\text{m}$ was used as a gold standard for qualitative validation of OCT and TPLI experiments. Tooth samples were placed in a cylindrical tube and positioned on the stage such that the treatment window would fall in the field of view of the detector. To minimize the effects of beam hardening, a 0.5 mm Al/Cu filter was used with a scan rate of 100 kV and exposure time of 1251 ms per frame. NRecon software (NRecon, version 1.7.1.6., Skyscan, Kontich, Belgium) was used to perform reconstruction on the

projections and DataViewer software was further used to display the captured cross-sectional slices on X, Y, and Z axis.


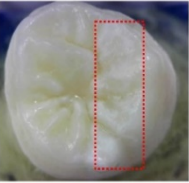
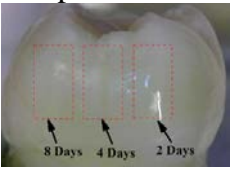

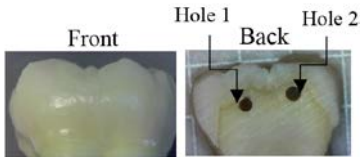

3.4 Dental Sample Preparation and Controlled Demineralization Protocol

Following the bio- and laser safety regulations at York University, anonymous extracted human teeth were collected from local oral surgeons. Samples were stored in tight container containing distilled water to maintain constant hydration and were kept in the laboratory fume hood at room temperature. The surfaces of the samples were not polished or altered in any way prior to the experiments. For controlled demineralization of dental samples, a lactic acid-based solution was prepared. The solution was an acidified gel (pH of 4.5), consisting of 0.1 M lactic acid and 0.1 M NaOH which is gelled with the addition of 6% w/v hydroxyethylcellulose [60, 67] This acidified gel is known to mimic the properties of bacterial plaques on enamel, providing an environment for cyclic occurrence of demineralization and remineralization and thus creating an early caries with thin healthy surface layer (as opposed to surface demineralization or erosion). As such, 4 teeth with no visible defect or white spot lesions was selected and cleaned namely samples 1 to 4 (Table 3.1). Samples were then mounted on LEGO blocks using an epoxy adhesive. After drying in air, the surface of tooth was covered by transparent nail polish, leaving a small window of a specific surface area uncovered, namely the treatment window. Applying the nail polish to the surface of the tooth except for the treatment window functions as a protection barrier, therefore, preventing other areas of the tooth from being exposed to the acidic gel. Sample was then submerged upside down in a test tube containing 25 ml of acidic gel and left in the gel for duration of the demineralization protocol (Figure 3.3) [60, 67]. After each treatment step/period, the sample was removed from the gel, cleaned under running water and dried in air [60, 67].

Then, the transparent nail polish was removed from the interrogated surface with acetone and the sample was again cleaned.

Acid exposure time of treatment windows for samples 1 and 2 was 10 days in order to produce advanced early caries. Sample 3 was designed to have 3 treatment windows with acid exposure times of 2, 4 and 8 days in left, middle and right windows, respectively. Imaging studies (sequence: OCT, TPLI, μ CT then TC-PCT) were carried out on samples 1-3 after completion of the abovementioned demineralization schedule. To study the systems' performance parameters as a function of demineralization time, the treatment window of sample 4 was incrementally demineralized. Imaging studies (OCT followed by TPLI) were conducted after each demineralization step. The treatment window's cumulative acid exposure duration at each imaging study session is depicted in Table 3.1. The μ CT experiment was conducted on sample 4 after the final demineralization step (i.e., 15 days). In preparation for OCT and TPLI imaging, the samples are air-blown and dried for 10 seconds to simulate the condition under which the inspection of caries is typically carried out in clinical scenarios. Additionally, to monitor the appearance of the demineralization window in each demineralization interval, a high magnification CCD camera was used to take photographs of the sample. Once imaged with the OCT and TPLI systems, the same procedure was repeated to apply additional demineralization in the treatment window. Samples 5 and 6 were used for TC-PCT image analysis. The back of sample 5 was drilled in order to induce two blind holes with varying remaining thicknesses and imaged with TPLI and TC-PCT to detect the holes (i.e. hidden defect). No artificial demineralization was applied to this sample. Sample 6 was demineralized in the same way that sample 3 was artificially demineralized except with different demineralization period. Only TC-PCT imaging was conducted on this sample.

Table 3.1: Samples' demineralization schedule and schematic of imaging study sequence.

Photograph	Study Target	Total Demineralization Period(s) Applied to Treatment Window	Sequence of Imaging Modalities Used at Each Demineralization Step
<p>Sample 1</p> 	Detection of Advanced Early Caries on Smooth Surface	10 days	OCT→TPLI→μCT
<p>Sample 2</p> 	Detection of Advanced Early Caries on Occlusal Surface	10 days	OCT→TPLI→μCT
<p>Sample 3</p> 	Detection Threshold	Left window-2days Middle Window-4days Right Window-8Days	OCT→TPLI→μCT →TC-PCT
<p>Sample 4</p> 	Detection Sensitivity	1day→2days→3days →4days→5days→6days →7days→8days →10days→15days	OCT→TPLI→μCT
<p>Sample 5</p> 	TC-PCT Image Analysis	None	TPLI→TC-PCT
<p>Sample 6</p> 	TC-PCT Image Analysis	Left window-3days Right Window-7Days	TC-PCT

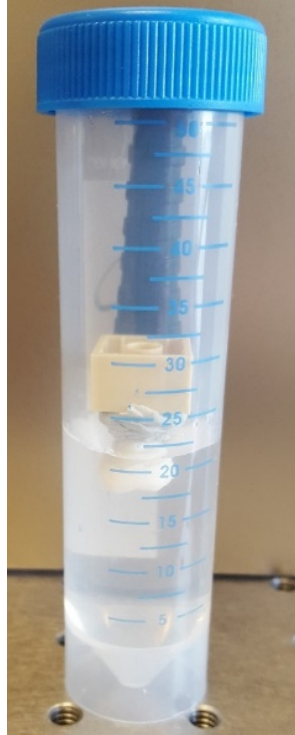


Figure 3.3: Tooth inside the acidic gel

3.5 Data Processing and Analysis of OCT and TPLI

In order to present the wealth of information obtained in an OCT 3-D volume more conveniently, we followed the convention in the field by producing integrated *en-face* images [39]. Integrated *en-face* images were produced by integrating the A-line values located 20 μm to 500 μm below the enamel surface. The integrated OCT *en-face* images (Figure 3.4) taken from sample 1 in Table 3.1 demonstrates that exclusion of the superficial 20 μm enabled us to remove the obscuring effects of surface specular reflections from the signals more efficiently.

To conduct a comparison of the images captured from OCT and TPLI at various stages of demineralization, the thermophotonic phase images at 2Hz and integrated *en-face* images derived from OCT were normalized. This was done to account for the small day-to-day changes in the experimental setup (e.g., laser source power) and tooth.

For integrated *en-face* OCT images, normalization was carried out by applying equation 3.2. That is, in any given integrated *en-face* image, the average pixel value of an intact reference area was divided from each pixel value.

$$\text{Normalized image pixel value} = \frac{\text{pixel value}}{\text{average amplitude value of healthy region}} \quad (3.2)$$

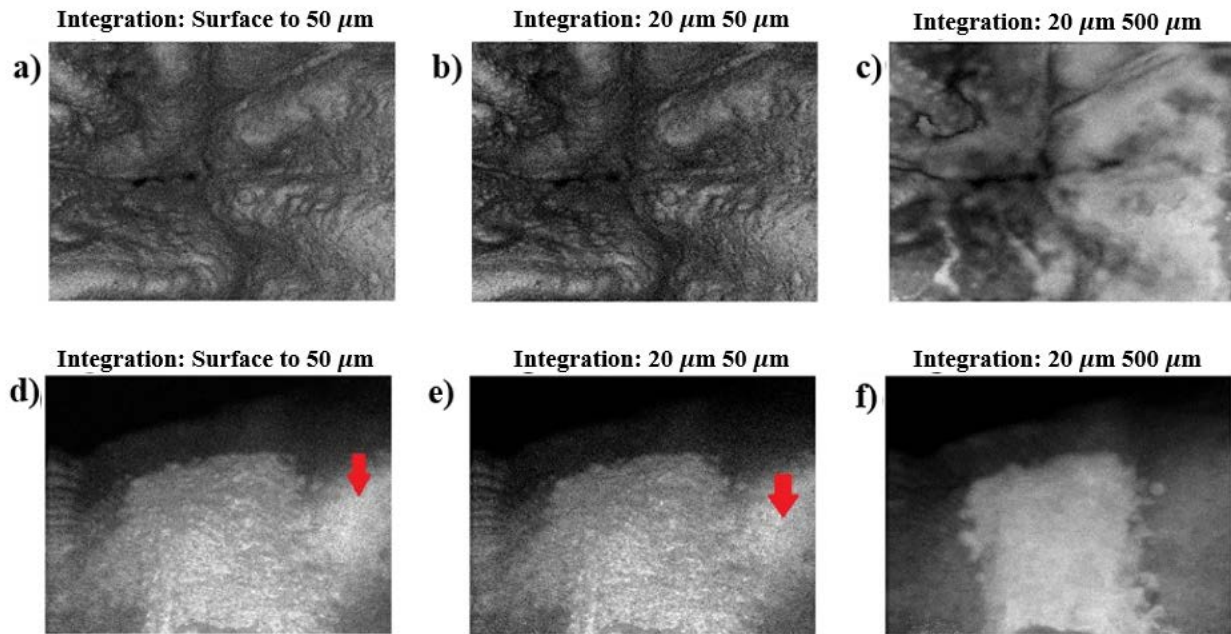


Figure 3.4: Integrated OCT *en-face* images using different integration limits along the depth of advanced caries on occlusal surface at (a) surface to 50 μm , (b) 20 μm to 50 μm (c) 20 μm to 500 μm , and smooth surface at (d) surface to 50 μm , (e) 20 μm to 50 μm (f) 20 μm to 500 μm .

For TPLI phase images, a similar normalization was performed:

$$\text{Normalized image pixel value} = \text{pixel value} - \text{average phase value of healthy region} \quad (3.3)$$

In order to quantify the diagnostic performances of the two systems, the following statistical analysis was conducted on the longitudinal demineralization study of the sample exposed to the demineralizing gel for various durations. First, the field of view of OCT and TPLI experiments were matched, followed by calculation of mean and standard deviation of contrast within the treatment window in each image. Then, the contrast value of each pixel in a given image was statistically compared to the mean and standard deviation of the treatment window within the same image with 95% confidence. Following this analysis, pixels having significantly different contrast compared to that of the treatment window were identified as true negative and false negative if they were located outside and inside the treatment window, respectively. Similarly,

pixels showing no significantly different contrast compared to that of the treatment window were identified as false positive and true positive if they were located outside and inside the treatment window, respectively. Following these quantifications, sensitivity and specificity values were calculated. Sensitivity measures the proportion of positives that are correctly identified. Low sensitivity suggests many false negatives. Additionally, specificity measures the proportion of negatives that are correctly identified.

$$\text{Sensitivity} = \frac{TP}{TP+FN} \quad (3.4)$$

$$\text{Specificity} = \frac{TN}{TN+FP} \quad (3.5)$$

where the TP , TN , FN , FP are true positive, true negative, false negative and false positive, respectively. From sensitivity and specificity, the corresponding receiver operating characteristic (ROC) curves were produced.

The ROC curve plots the sensitivity versus (1 -specificity) and it is an effective method of comparing performances of diagnostic tests. Better performing diagnostic tests have ROC curves where the sensitivity is high for whole range of specificities and are thus located closer to the upper left-hand corner in “ROC space” [68]. For instance, Figure 3.5 shows experiment 1 has a better diagnostic capability than experiment 2.

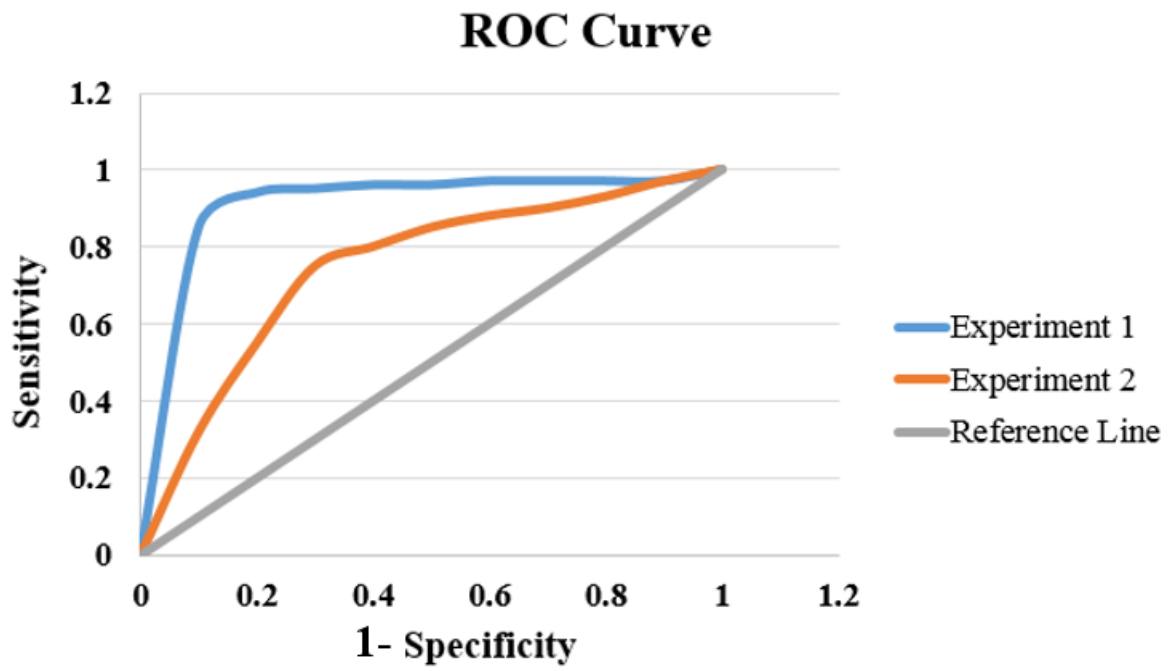


Figure 3.5: ROC curves of two diagnostic experiments

Chapter 4

Comparison of TPLI and OCT in Detection of Early Caries

This section presents and discusses the experimental results and outcome from the comparison of OCT and TPLI in detection of early caries.

4.1 Detection of Advanced Early Caries

To examine the performances of OCT and TPLI in detecting advanced stages of early caries, teeth samples which were demineralized for 10 days on the smooth (sample 1) and occlusal (sample 2) surfaces were imaged. The visual photographs of these samples were acquired after drying with compressed air, Figure 4.1(a)-(b); rectangles depict the location of treatment windows. The photographs indicate the presence of white spot lesions on both samples, suggesting presence of early caries that have progressed well into the enamel layer (i.e., advanced early caries). In the OCT B-scan and integrated *en-face* images of the samples (Figure 4.1(c)-(f)), the presence of the advanced enamel caries is well-recognized with a sharp contrast as a result of enhancement of light scattering within the treated region. Consequently, the demineralized regions appear bright in both B-mode and *en-face* images. This observation is consistent with reports of other researchers [69, 70]. Moreover, the B-mode/cross sectional image of Figure 4.1(c) suggests that the enhancement in light scattering within the superficial caries region has been to an extent that the light photons could not effectively probe the underlying dental-enamel-junction (DEJ). For the healthy areas surrounding the treatment region, however, the light backscattering is not significant enough to mask the underlying structures as the tooth surface was protected against the demineralizing acid by the nail polish coating. As a result, DEJ can clearly be recognized in the untreated areas in the cross-sectional image of the smooth surface caries, Figure 4.1(c). The B-mode OCT image of the advanced occlusal caries,

Figure 4.1(d), is also showing enhanced light scattering within the treated region. However, the DEJ cannot be resolved in this image due to the large thickness of enamel in the occlusal region and the limited imaging depth of OCT. Similar to OCT, the presence of lesions is clearly observed in the TPLI phase image taken at 2Hz after 10 days of demineralization, Figure 4.1(g)-(h). Selective absorption of laser light at caries sites results in shifting of the centroid of the thermal-wave field and causes a phase shift in the thermal signals registered from caries areas compared to those collected from intact regions. The increase in light absorption at caries sites occurs as a result of absorption of laser light by the by-products of demineralization. Light absorption is further enhanced by the local enhancement of light scattering at caries as it results in increase in the local laser light flux within the caries area.

Compared to images taken with OCT, TPLI images offer a much larger field of view of the tooth with similar detection sensitivity. Another key difference between the performances of OCT and TPLI in detecting dental caries is the detection specificity (i.e., ability to yield minimal false positives). Figure 4.1(d) and Figure 4.1(f) suggest that although the treated area appears with an enhanced contrast in the image, there are other areas outside the treatment windows which also show up as bright in both B-mode and integrated *en-face* images, yellow arrows in Figure 4.1(d) and 4.1(f). Figure 4.1(i) and 4.1(j) show the μ CT slices taken from the bright areas inside and outside the treatment window, respectively, along the dashed lines indicated in Figure 4.1(f). These μ CT slices clearly show the presence of early caries in the treatment window but no indication of mineral loss outside the treatment window and in the area where the OCT *en-face* image displays enhancement in contrast (yellow arrows). The characteristic mineral profile of early caries (i.e., area of mineral loss close to surface, protected by a thin healthy layer) is clearly resolved in the μ CT slice taken from the treated area which speaks to the effectiveness of the

artificial demineralization protocol adhered to in this study. As such, our results suggest that while the integrated *en-face* and B-scan OCT images indicate the ability of OCT in detecting advanced stages of smooth surface and occlusal early caries as areas of enhanced light scattering, structural non-homogeneities other than those caused by demineralization induce a similar effect in OCT images; thus, creating false positive readings. Presence of false positives speaks to the non-specific nature of light scattering contrast mechanism which is enhanced as a result of discontinuities in refractive index, not necessarily caused by demineralization. While non-specific nature of OCT images of early caries has also been reported by other investigators [38, 71], recent studies suggest that this problem can be alleviated using PS-OCT [48]. TPLI images, on the other hand, display enhancement of contrast only within the treated area because laser excitation is selectively absorbed in these regions; thus, yielding minimal false positive readings. The downside of TPLI imaging, however, is that these images are governed by the physics of heat diffusion and as such are depth-integrated rather than depth resolved and cannot provide tomographic maps of samples or create transverse/B-mode type images resolving internal tissue features. In summary, qualitative analysis of results of Figure 4.1 suggests that both optical systems have sufficient detection sensitivity to detect advanced stages of early caries on smooth and occlusal surfaces; however, detection specificity is better in TPLI imaging.

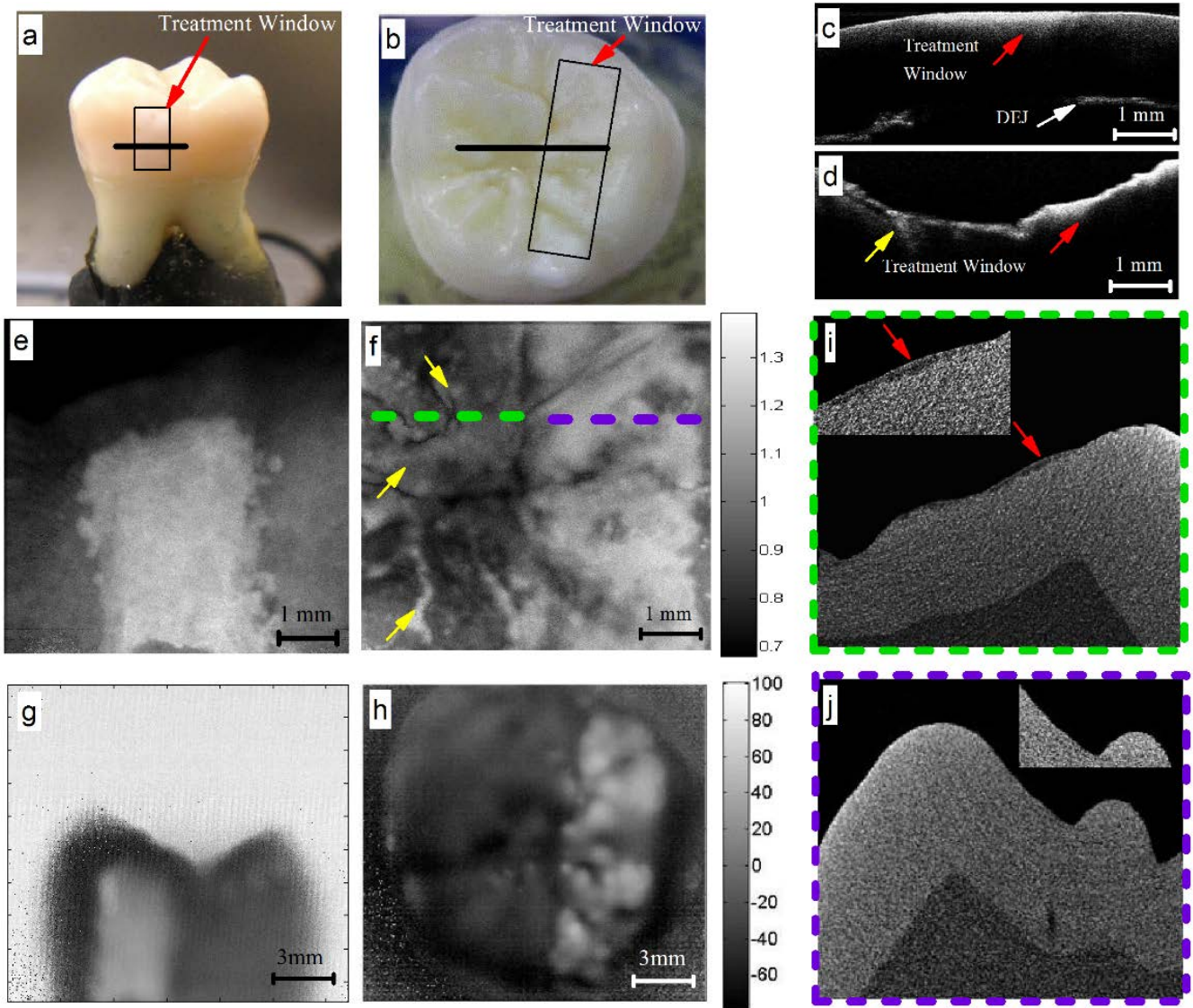


Figure 4.1: Photographs of simulated advanced caries on (a) smooth and (b) occlusal surfaces; rectangles depict the location of treatment windows. Representative OCT B-mode images of (c) smooth surface and (d) occlusal caries samples along the solid lines indicated in panels (a) and (b), respectively. Integrated en-face OCT images at 10 days of treatment of (e) smooth and (f) occlusal caries samples. TPLI phase images obtained at 2-Hz modulation frequency at 10 days of treatment for (g) smooth surface (h) occlusal caries samples. (i) and (j) represent the μ CT slices along the green and blue dashed lines in panel (f), respectively.

Red and yellow arrows point to treatment window and false positives, respectively.

4.2 Comparison of Detection Threshold

In the context of detecting early dental caries, detection threshold is the smallest amount of demineralization that a diagnostic system can reliably detect. To study this performance parameter, a healthy tooth sample (sample 3) with three artificially-induced caries for 2, 4 and 8 days on the same surface was chosen (Figure 4.2(a)). As it can be seen in integrated *en-face* OCT images (Figure 4.2(c)-(e)), the presence of demineralization is not visually detectable in 2- and 4-day treated windows due to the reflections with same level of contrast as of the treated regions originating from the healthy regions (i.e., false positives). However, the 8-day treated window shows a relatively higher contrast making it somewhat distinguishable, Figure 4.2(e). Similar trend is observed in the OCT B-mode images (Figure 4.2(f)-(h)): After 8 days of treatment, the demineralization has made further progress with reduced contrast at the DEJ as a result of overlaying demineralization; however, for 2- and 4-day windows, the DEJ appears with normal contrast due to the minimal enhancement of light scattering at demineralized areas. TPLI (Figure 4.2(b)), on the other hand, is capable of detecting all the artificially-induced caries as higher contrast areas. The contrast of demineralized regions of 2 and 4 days are approximately equal but their contrast compared to the intact areas of the enamel are higher. The contrast at 8 days of demineralization shows a significant increase by visual inspection compared to other treatment windows as well as intact areas. However, since in this sample the extent of demineralization has been quite small, μ CT images (panels Figure 4.2(i)-(k)) are incapable of detecting such very early stages of caries formation and they show vague indications of demineralization at 4 and 8 days of treatment. This insensitivity is, in fact, the motivation behind the surge of research on optical imaging methods for detection of early caries.

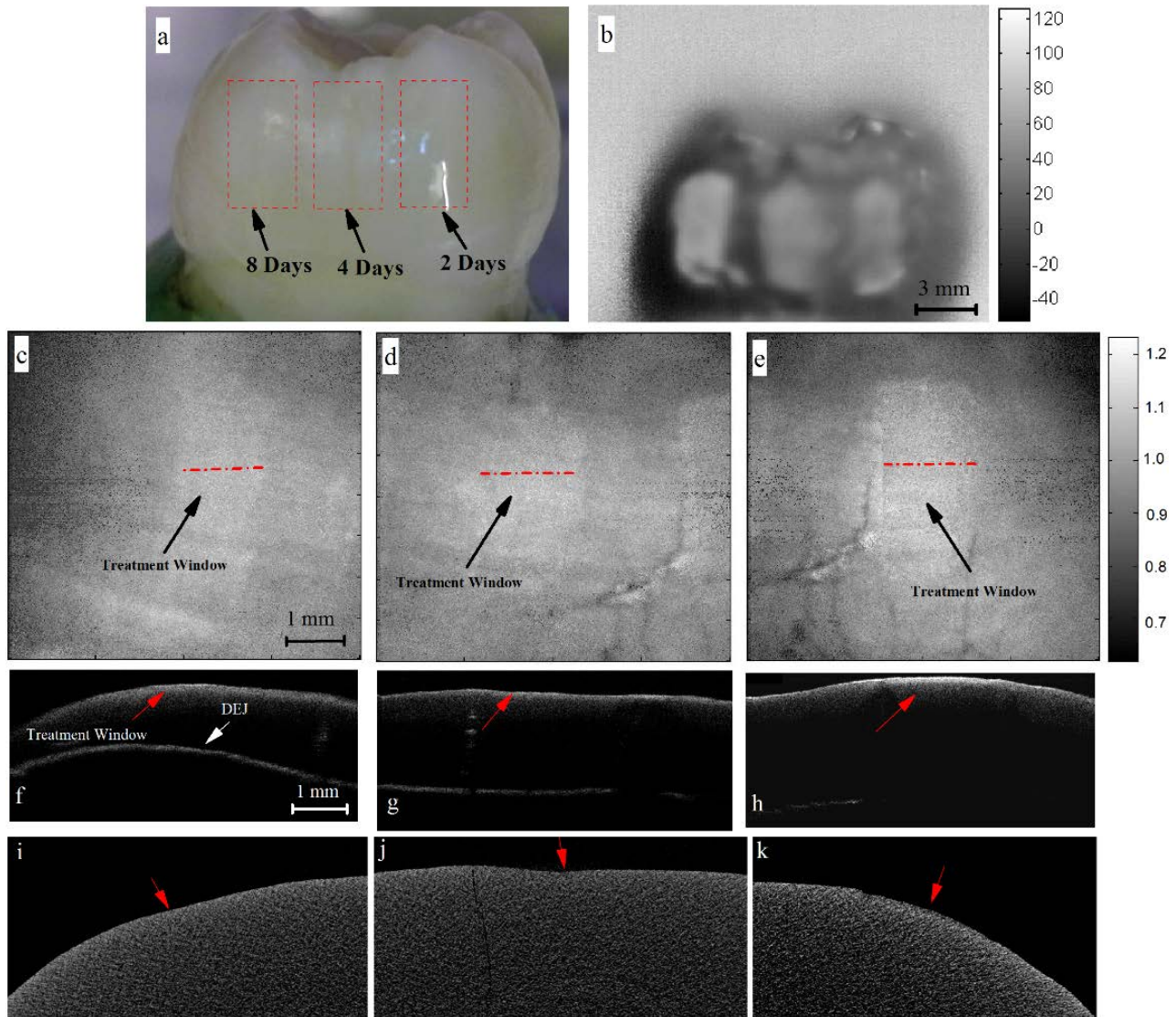


Figure 4.2: (a) Visual image of tooth with artificially-induced caries at 3 locations. (b) TPLI phase image at 2-Hz modulation frequency. Integrated en-face OCT images at (c) 2 days, (d) 4 days, and (e) 8 days of demineralization. B-scan OCT images at (f) 2 days, (g) 4 days, and (h) 8 days of demineralization. μ CT images at (i) 2 days, (j) 4 days, and (k) 8 days of demineralization.

Quantitative analysis was also conducted on images of Figure 4.3. The bar plots of the average integrated intensity of the integrated *en-face* OCT images (Figure 4.3(a)) along with their standard deviations indicate that OCT is statistically not specific enough to differentiate between the sound/healthy and each of the demineralized windows as the average integrated intensity values of all the treatment windows are within the standard deviation of the average integrated

intensity value obtained from the untreated healthy region. However, the TPLI bar plots (Figure 4.3(b)) suggest reliable increase of average normalized phase values between treated and healthy areas. The carious lesion formed as early as 2-days of demineralization can be differentiated due to an increase in average phase value above the range of standard deviation of phase value derived from the healthy region. The enhancement in detection threshold of TPLI over OCT is because of its basis on light absorption, thus effectively eliminating the background signals from healthy areas. Quantification of μ CT images, panel (c), indicates that none of the treated windows can be reliably identified.

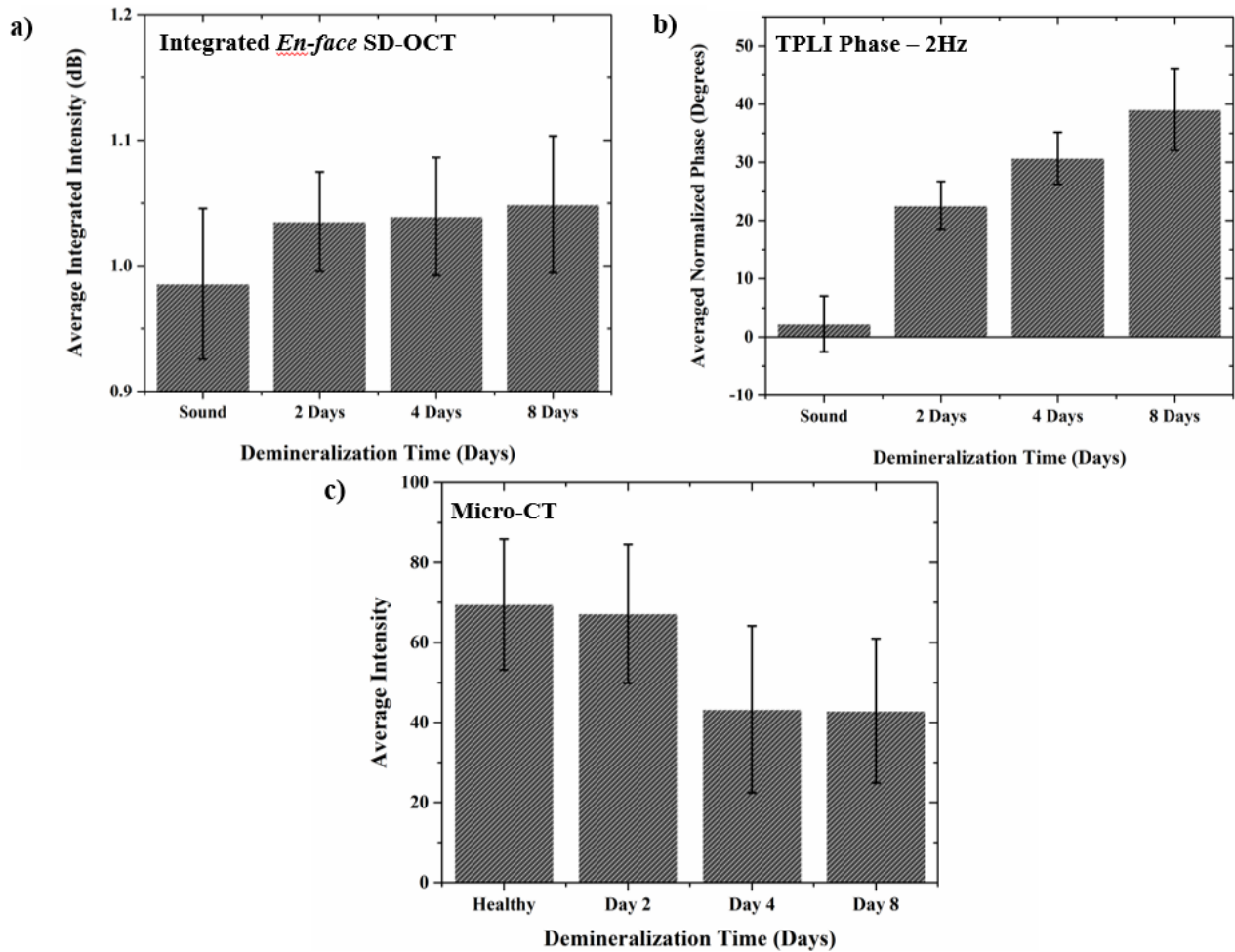


Figure 4.3: Average contrast values from early caries and the associated standard deviation of mean for (a) optical coherence tomography (OCT) and (b) thermophotonic lock-in imaging (TPLI), and (c) μ CT.

4.3 Detection Sensitivity of OCT and TPLI

In the context of detection of early dental caries, detection sensitivity is linked to the ability of the diagnostic system in creating a noticeable change in contrast given an incremental increase in demineralization [70]. For this performance metric, a time-dependent demineralization procedure was followed on smooth surface of a relatively healthy tooth (sample 4) in small intervals of 1 day up to 8 days of demineralization and larger intervals up to 15 days of demineralization. Figure 4.4(a) and 4.4(b) show the photograph of the sample before and after application of 15-days of demineralization, respectively. In integrated *en-face* and B-scan OCT images (Figure 4.4(c)-(n)), a very small change in contrast at the treatment window starts from day 1 of demineralization. This change in contrast gradually increases while reaching its maximum contrast at day 15 of demineralization. The presence of false positives (shown with yellow arrows) can be seen in many of these OCT images. Similar trend can be seen in TPLI phase images (Figure 4.5) with contrast becoming reliably detectable at day 2 of demineralization, with gradual enhancement up to day 15 of demineralization. Thinning of enamel at the cervical margin (yellow arrow) results in underlying cementum acting as thermal impedance; thus, creating a change in contrast.

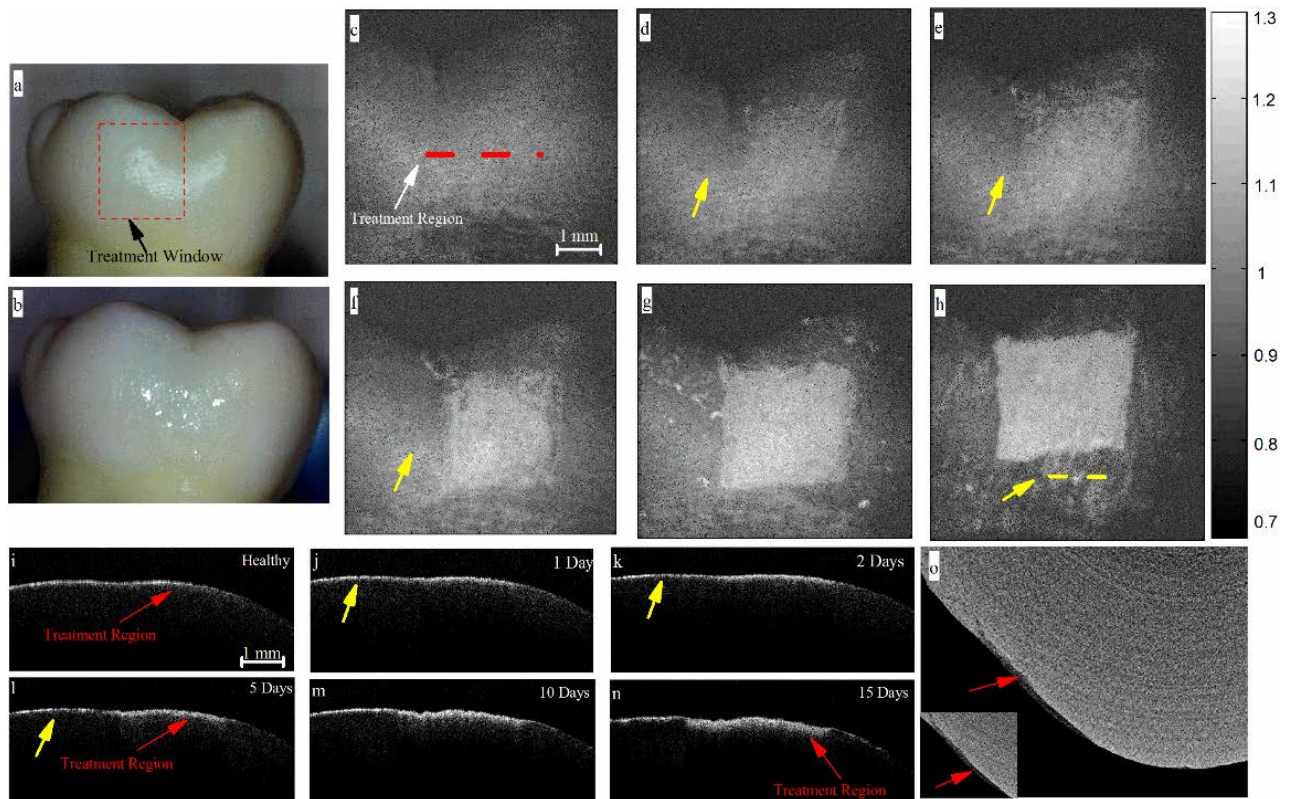


Figure 4.4: Optical image of the smooth surface of extracted human molar (a) before demineralization and (b) after 15 days of demineralization on the treatment window. Integrated en-face OCT images at (c) 0 days, (d) 1 day, (e) 2 days, (f) 5 days, (g) 10 days, and (h) 15 days of demineralization. B-scan OCT images at (i) 0 days, (j) 1 day, (k) 2 days, (l) 5 days, (m) 10 days, and (n) 15 days of demineralization. (o) μ CT image of 15-days treated sample.

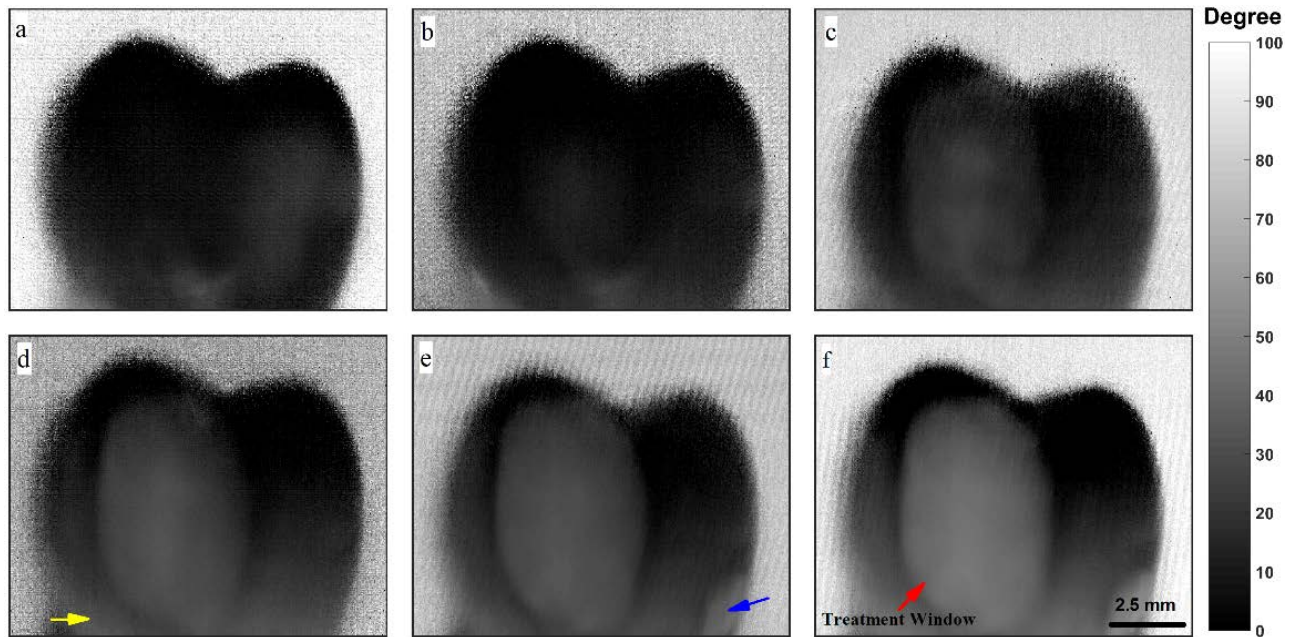


Figure 4.5: TPLI phase images at 2-Hz modulation frequency at (a) 0 days, (b) 1 day, (c) 2 days, (d) 5 days, (e) 10 days, and (f) 15 days of demineralization. Yellow arrow points to change in contrast at cervical margin due to thinning of enamel and photothermal effects of the underlying cementum. Blue arrow points to part of the enamel which was damaged on day 10 of demineralization due to improper handling.

To further study the changes in average phase and integrated intensity values over various stages of demineralization progression, Figure 4.6 shows the bar plots generated from OCT and TPLI images of Figure 4.4 and Figure 4.5. In integrated *en-face* OCT bar plots (Figure 4.6(a)), it can be seen that with progression of artificially-induced early caries, there is a gradual enhancement in average integrated intensities. However, these small enhancements cannot be reliably realized due to the large standard deviations associated with the averaged contrast values. Consequently, it can be concluded that, in these experiments, OCT could not reliably differentiate between healthy and early carious lesions up to day 10 of treatment, setting the earliest reliable detection at 15 days of treatment. Figure 4.6(b) depicts the bar plots of the TPLI experiments. It can be seen that the detection threshold of TPLI can be distinguished as early as day 2 of demineralization. Moreover, a sizable change in contrast is observed as demineralization

increases from 1 day of treatment to 15 days of treatment. The enhanced detection sensitivity of TPLI over OCT can be verified by calculating the amount of change in contrast at the detection threshold. For OCT, a 17.5% increase in contrast (1.011dB to 1.188dB) is observed after 15 days of treatment while TPLI contrast increases by 203% (-11.2° to 11.5°) only after 2 days of treatment. The TPLI enhancement in contrast at OCT detection threshold (i.e., 15 days of treatment) is found to be 424% (-11.2° to 36.3°). Panel (c) indicates the ability of μ CT in detecting the well-developed early caries after 15 days of demineralization.

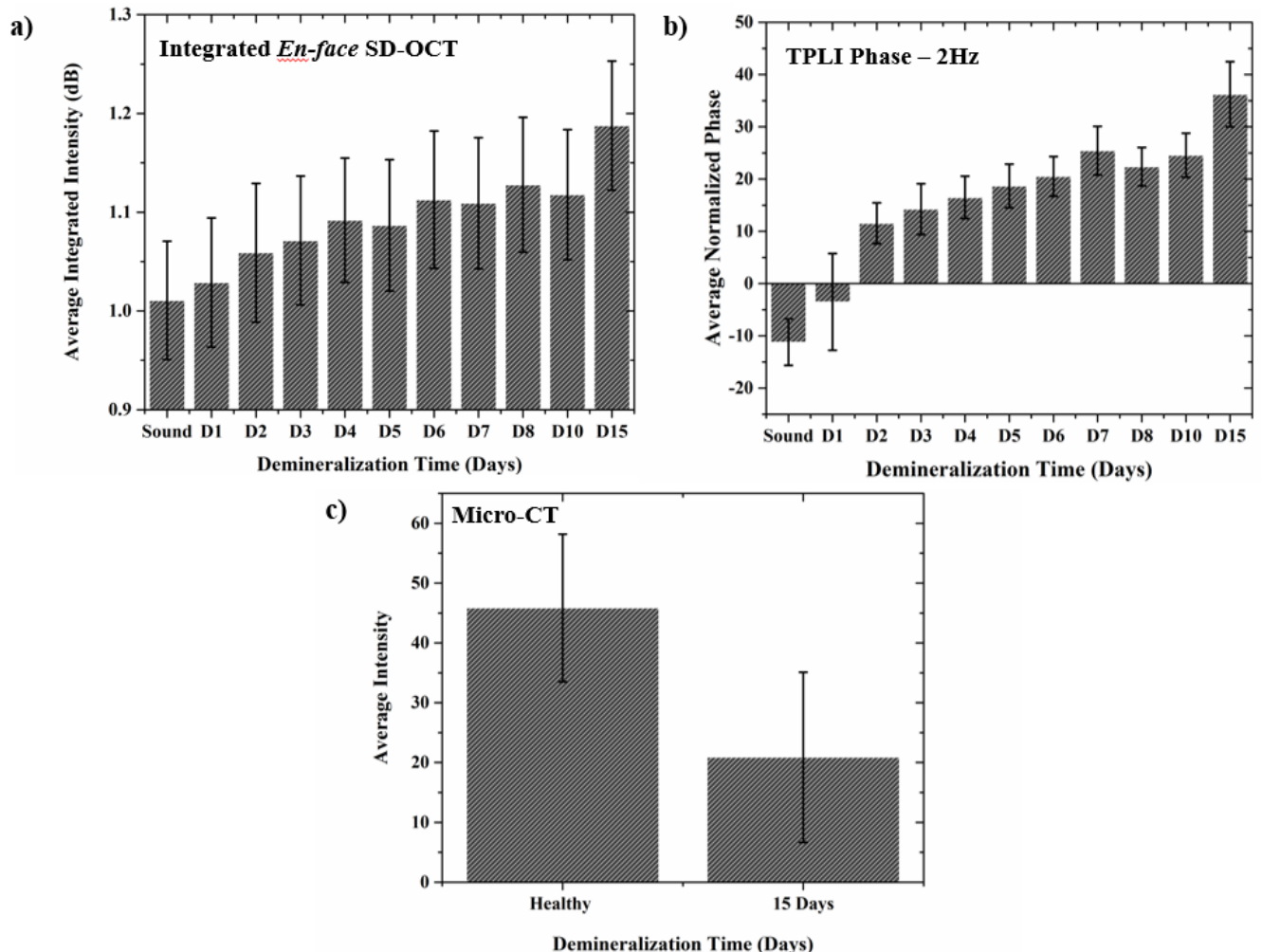


Figure 4.6: Average contrast values from early caries and the associated standard deviation for (a) spectral-domain optical coherence tomography (OCT), (b) thermophotonic lock-in imaging (TPLI), and (c) μ CT.

Figure 4.7 and Figure 4.8 depicts results of the statistical analysis carried out using the procedure explained in section 3.5. Figure 4.7(a) and Figure 4.7(b) highlight pixels that are statistically identified as demineralized (i.e., yellow pixels) by OCT and TPLI at different stages of demineralization. It can be seen that false positives (i.e., yellow pixels outside the treatment window) are significantly reduced in TPLI at 2 days (or more) of demineralization while such false positives are dominantly present in OCT images up to 7 or 8 days of demineralization. The tabulated sensitivity and specificity data in Figure 4.8(a) confirms this visual observation. Finally, the ROC plot in Figure 4.8(b) clearly shows that both technologies are sensitive to detection of early caries. However, accumulation of TPLI data points in the upper left corner of the ROC plot confirms the more specific nature of TPLI over OCT, especially at early stages of caries formation.

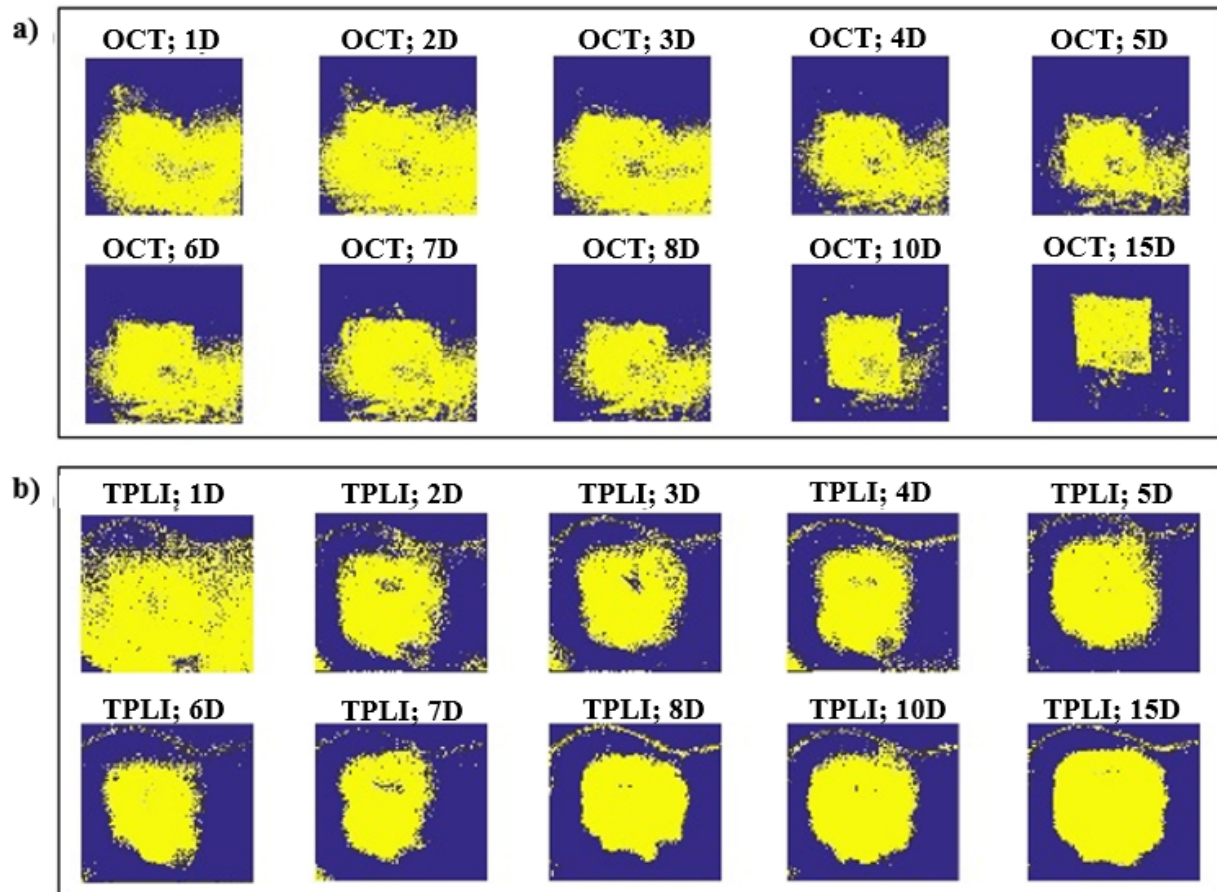


Figure 4.7: Statistically (CI: 95%) identified healthy (blue pixels) and demineralized (yellow pixels) at various stages of demineralization by (a) OCT and (b) TPLI.

a)

		1D	2D	3D	4D	5D	6D	7D	8D	10D	15D
CP-OCT	S	0.91	0.96	0.91	0.87	0.83	0.93	0.93	0.88	0.84	0.82
	P	0.61	0.54	0.62	0.76	0.85	0.73	0.73	0.82	0.95	0.98
TPLI	S	0.96	0.88	0.90	0.91	0.96	0.92	0.91	0.92	0.92	0.91
	P	0.42	0.86	0.86	0.89	0.87	0.90	0.91	0.91	0.91	0.93

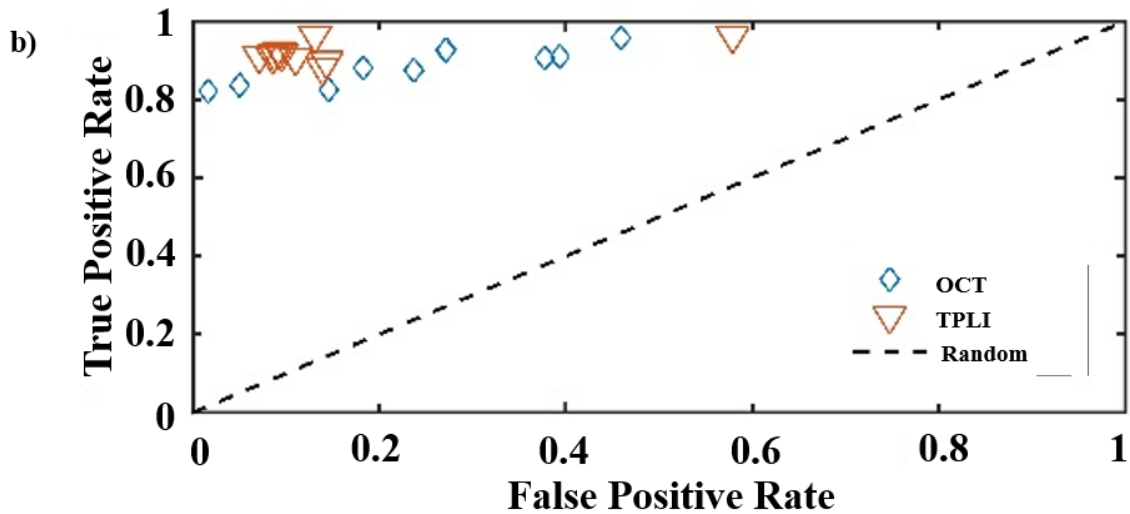


Figure 4.8: Corresponding (a) sensitivity (S) and specificity (P) values and (b) receiver operating characteristic (ROC) curve.

4.4 Summary of the Comparative Study

In this chapter, we present results of a comparative study between cross-polarization spectral-domain optical coherence tomography (OCT) and thermophotonic lock-in imaging (TPLI) in detecting early dental caries. The effectiveness of the artificial demineralization protocol adhered has been demonstrated through μ CT validation experiments. Our experimental results suggests that both modalities have sufficient sensitivity for detection of well-developed early caries on

occlusal and smooth surfaces; however, TPLI provides better sensitivity and detection threshold in detecting very early stages of caries formation which is deemed to be critical for effectiveness of therapeutic and preventive approaches in Dentistry. Moreover, due to the more specific nature of light absorption contrast mechanism over light scattering, TPLI exhibits better detection specificity which results in significantly less false positive readings and thus allows for proper differentiation of early caries regions from the surrounding intact areas. TPLI, as a hybrid imaging method, is intrinsically insensitive to surface reflection because in TPLI laser excitation is carried out with an 808 nm laser but thermal detection is performed in the 8000-14,000 nm. Therefore, any laser reflection from the surface (or any other place) does not fall in the spectral range of the IR camera. This is in fact one of the reasons behind better specificity of TPLI. Other advantages of TPLI over OCT include larger field of view and less complexity of instrumentation. Major advantage of OCT over TPLI is its depth-selective and 3-D tomographic nature over the intrinsic depth-integrated and 2-D nature of TPLI which enables visualization of lesions within the 1-2 millimeter inspection range of OCT. 3-D visualization of lesions enables quantification of parameters such as lesion depth and volume. Consequently, a light-absorption based imaging modality with the ability to produce tomographic and depth-resolved images is highly desired in the field of Dentistry as such modality would simultaneously offer the major advantages of OCT and TPLI. Truncated-correlation photothermal coherence tomography (TC-PCT) [72] and photothermal optical coherence tomography (PCT) [73] are extensions of TPLI and OCT, respectively, which can theoretically provide such 3-D maps based on absorption of light. Therefore, in the next chapter we present preliminary results exploring the feasibility of detecting and visualizing caries and hidden defects using TC-PCT.

Chapter 5

Truncated-Correlation Photothermal Coherence Tomography (TC-PCT) Analysis

As demonstrated in previous chapters, the most important limitation of TPLI is its intrinsic depth integrated nature which results in acquisition of 2-D images in which light absorbing features within the thermal diffusion length are superposed. Matched-filter thermography incorporates radar signal coding and decoding techniques in order to alleviate the depth integrated limitation of thermography. This section provides basic principles of radar matched-filtering and its application in an optimal thermography technology known as Truncated-Correlation Photothermal Coherence Tomography (TC-PCT). While, similar to TPLI, TC-PCT operates based on absorption of light, due to matched-filtering it can provide 3-D visualization of subsurface defects. After presentation of principles and methodology, the chapter concludes by presentation of results of preliminary experiments.

5.1 Introduction to Matched Filtering in Thermography

In chapter 4, we demonstrated the more specific and sensitive nature of light absorption based imaging modalities in detecting defects. These enhancements in performance are believed to be key to the success of preventive measures in Dentistry in order to heal or arrest caries. However, major shortcoming of TPLI is its depth-integrated and 2-D nature. Therefore, a technique known as radar matched filtering has recently been introduced to the field of thermography to maintain resolution while probing deep in samples. Matched filter is a special type of filter with which a replica of a known signal (aka matched-filter) can be detected in a noisy signal [74]. For instance, consider a sonar system sending waves of known pattern and trying to determine the distance of an object from the antennas received signals. It would be very challenging to remove

the noise without altering the true back reflected signal from object. Hence, a matched filter based on the pattern of the output waves of sonar can be used for correlation with received noisy signal not only to determine the presence of replica of transmitted signal, but also to characterize the properties of the backscattered signal from the object. From a mathematical point of view, matched filter is incorporated by carrying out the cross-correlation of excitation, $e(t)$, and response, $r(t)$, signals.

$$CC(\tau) = \int_{-\infty}^{\infty} e(t)r(t - \tau)dt \quad (5.1)$$

Or more conveniently in frequency-domain using excitation, $E(\omega)$, and response, $R(\omega)$, spectra as:

$$CC(\tau) = \mathfrak{F}^{-1}\{E^*(\omega)R(\omega)\} \quad (5.2)$$

Here \mathfrak{F} and $*$ denote Fourier transform and complex conjugate operators. Figure 5.1 schematically present the output of such cross-correlation (CC) as a *Sinc* signal with its main peak located in delay time axis at τ_p [15, 75]. This delay time represents the delay between the transmitted and received signals. As such, location of main peak determines the distance of the object from antenna while the width of the main peak determines radars axial/depth resolution. For better axial/depth resolution, the main peak of the CC has to be narrower. In addition, for higher SNR the height of the main peak has to be larger. A technique known as “pulse compression” is often employed to decrease the width of the CC peak for higher axial resolution and increase the height for better SNR [15, 76, 77]. The idea behind pulse compression is to code/pattern the transmitted/excitation waveform using frequency or phase modulation so that after matched filtering a narrower and better SNR response is achieved.

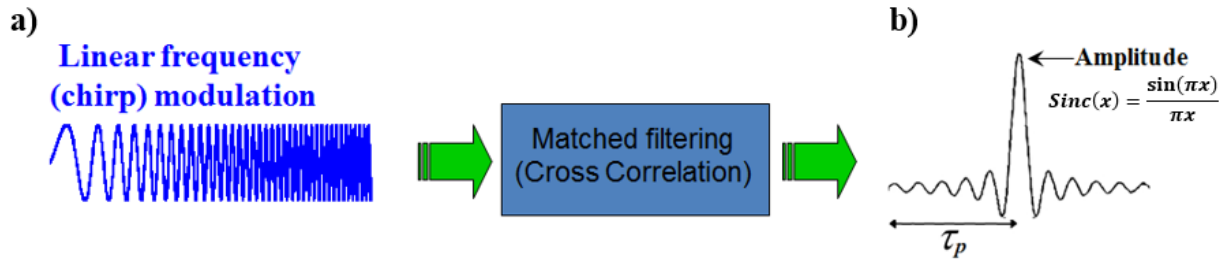


Figure 5.1: (a) Linear frequency chirp signal (b) the outcome of matched filtering

Aside from radars, matched-filtering is used in tomographic medical imaging modalities such as 3-D ultrasound and optical coherence tomography. In the field of thermography, matched filtering is used to alleviate the depth integrated nature of thermal responses in order to differentiate between the depths of defects. That is, in matched filter thermography laser intensity modulation is performed using a pulse compression technique (instead of single frequency modulation in TPLI) and the thermal amplitude and phase responses are found by finding the cross-correlation of the laser modulation pattern and infrared camera frames (as opposed to lock-in demodulation in TPLI). To demonstrate the concept, sections below briefly present and review select matched filter thermography works using two commonly used pulse compression methods known as linear frequency modulation (LFM) and binary phase coding (BPC).

5.1.1 Linear Frequency Modulation

Matched filters are commonly used in the radar signal processing using chirp or linear frequency modulated signals [78]. A linear frequency chirp (LFM) signal is a signal in which the frequency increases (up-chirp) or decreases (down-chirp) with time (Figure 5.1(a)) [15, 77].

Figure 5.2(a) shows the result of the cross-correlation of one chirp signal with no delay and another chirp signal with delay. Panel (b), on the other hand, displays the cross-correlation of two mono frequency sine-waves. Comparison of these two matched-filter responses indicates

that LFM compresses the energy of the signals under the main lobe of the output; thus, significantly increasing the SNR while improving axial resolution.

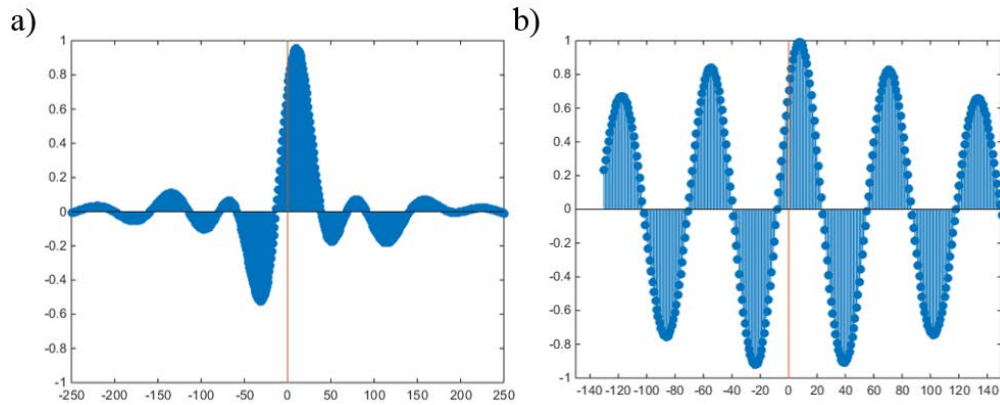


Figure 5.2: Cross-correlation of a) two chirp waves and b) two sine waves

Tabatabaei *et al.* [79] were the first to implement LFM matched-filtering in thermography, coining the name thermal waver radar (TWR) imaging. Figure 5.3(a)-(c) show the three contrast parameters that can be used in thermophotonic radar imaging: amplitude, peak delay time (τ_p), and phase [79]. Here the sample is a stack of transparent glass slides painted with different colors at the bottom surface, simulating iso-depth absorbers with different light absorption coefficients. Figure 5.3(d)-(f) show that the peak delay time and phase channels can reliably determine the depth of absorbers while the amplitude channel provides information on the strength of light absorption [79].

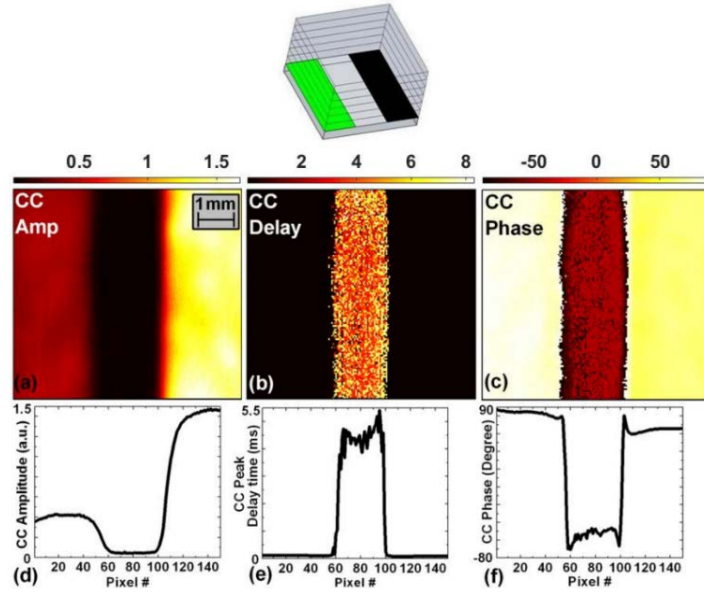


Figure 5.3: Thermophotonic radar imaging of a transparent sample with different absorption coefficients using (a) Cross-correlation (CC) amplitude; (b) CC peak delay time; (c) CC phase and their mean horizontal profiles; (d-f), respectively [79], Copyright 2011, American Institute of Physics.

Figure 5.4 shows the comparative results on the depth resolution capabilities between lock-in thermography (LIT) and thermal-wave radar (TWR) imaging on a black plastic step wedge sample in a turbid medium [79]. In the LIT images, it can be seen that at low modulation frequencies (Figure 5.4(a)) all steps can be detected but steps cannot be resolved from each other due to the poor axial resolution at large thermal diffusion lengths. At high LIT frequencies (Figure 5.4(b)), on the other hand, axial resolution is significantly improved but only shallow steps can statistically be detected. These figures clearly demonstrate the classic compromise of LIT between inspection depth and depth resolution. Figure 5.4(c) is the matched-filter thermography amplitude image obtained from 0.01-1 Hz chirps with 6s demonstrating that, using the principles of matched filtering, TWR imaging not only resolves the steps but detects them all [79].

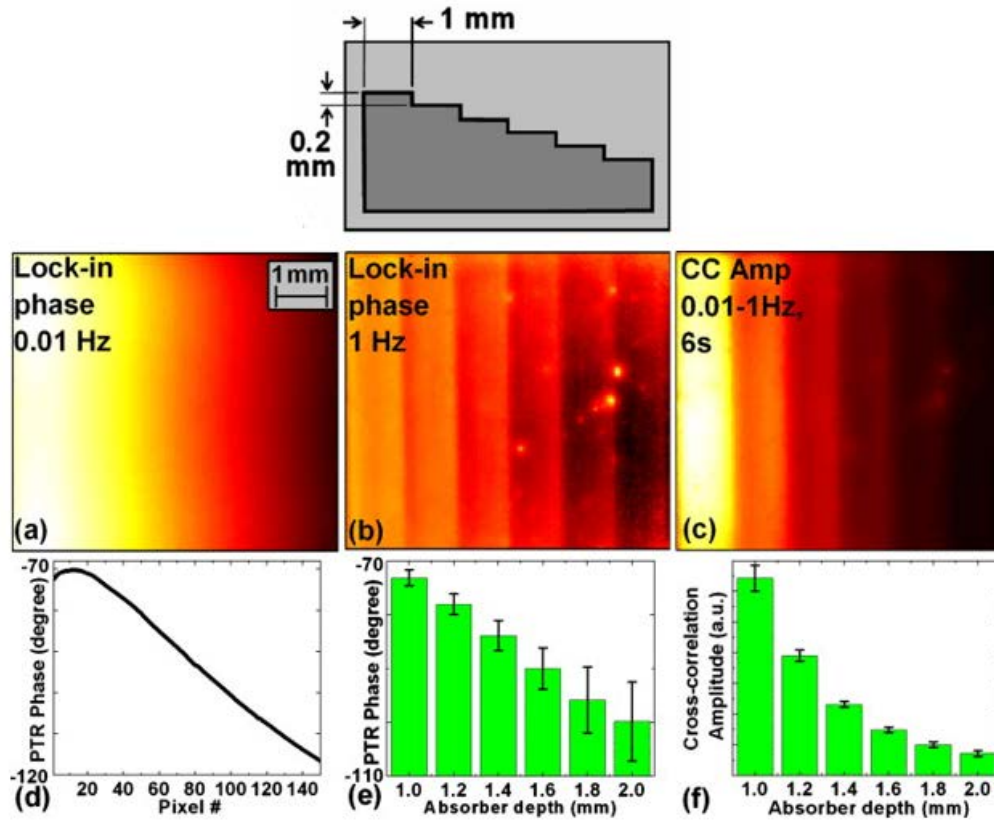


Figure 5.4: TWR and TLI imaging of plastic step wedge. LIT phase images at (a) 0.01 Hz and (b) 1 Hz; (c) CC amplitude image; and (d) mean horizontal profile of figure (a). Distribution of (e) LIT phase and (f) CC peak amplitude values and standard deviations over the steps [79], Copyright 2011, American Institute of Physics.

5.1.2 Binary Phase Coding

Another type of pulse compression is binary phase coding (BPC) which encodes the transmitted pulse with information that is compressed in the receiver of the radar [15, 80]. The BPC signal consists of a single frequency carrier and a binary coded envelope. The narrow band signal is formed either by multiplying these components in the time-domain or alternatively by convolving their spectra in the frequency-domain, Figure 5.5. As it can be seen in Figure 5.5, the BPC signals contains weighted *Sinc* functions which results in a waveform that has most of its energy at the carrier frequency yielding a narrow-band waveform, as opposed to the wide band LFM signals [15, 80].

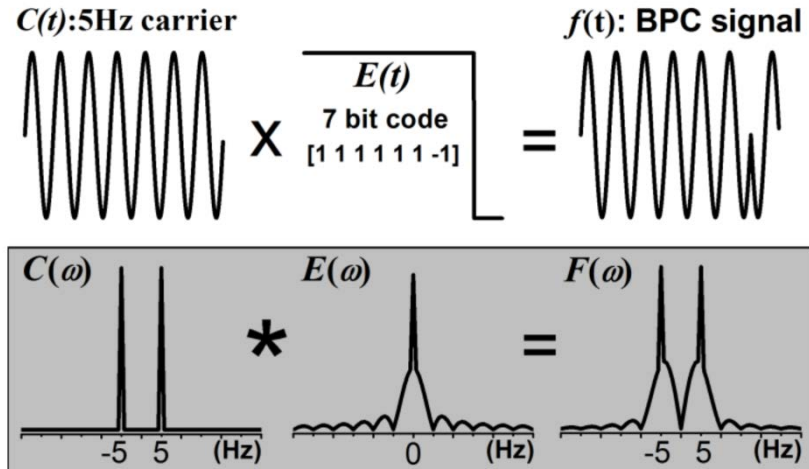


Figure 5.5: Schematic procedure of Binary Phase Coding (BPC) signal construction in time (top) and frequency (bottom) domains for a 7-bit code and 5 Hz carrier [15, 80], Copyright 2012, Nima Tabatabaei.

Tabatabaei *et al.* [80] were the first to implement BPC matched-filtering in thermography, coining the name thermal coherence tomography (TCT) imaging and demonstrating its enhanced imaging performance over LIT and TWR.

Figure 5.6(b) shows the LIT phase image along with its mean profile over the same step wedge sample discussed in Figure 5.4. Panel (b) demonstrates that in LIT a sacrifice in axial resolution is required for detection of all steps [80]. On the other hand, TCT imaging yields excellent resolution down to the deepest step in both peak delay time and phase images, Figures 5.6(c) and (d), respectively [80].

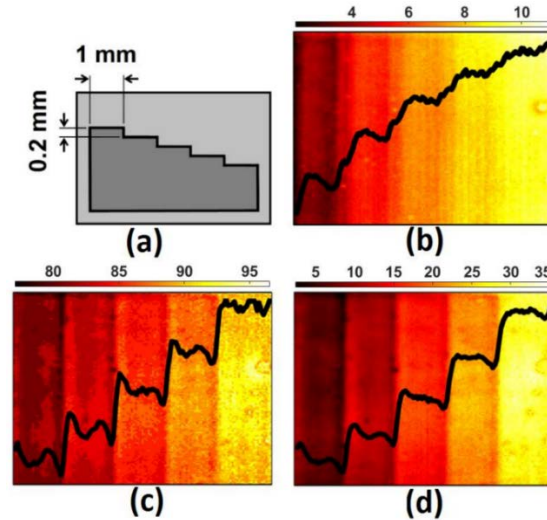


Figure 5.6: (a) plastic step wedge; (b) LIT phase (unit: degree); (c) BPC peak delay time (unit: millisecond); and (d) BPC phase images (unit: degree). The experiments are obtained at 3Hz The curve in each image shows the mean horizontal profile of the corresponding contrast parameter [80], Copyright 2012, Nima Tabatabaei.

Figure 5.7 shows experimental results obtained from a teeth matrix with interproximal early caries. The contacting surface of the teeth has been artificially demineralized. Comparison of LIT and BPC phase images (Figures 5.7(b) and (c)), demonstrate the enhanced axial resolution of the BPC over LIT while detecting the deep interproximal defect [80].

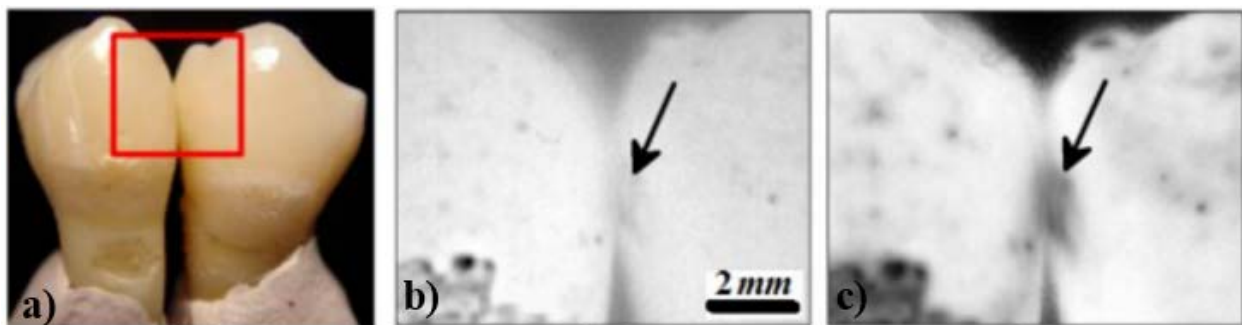


Figure 5.7: (a) teeth with inter-proximal early caries. The rectangle shows the imaged area; (b) conventional LIT and (c) BPC phase images [80], Copyright 2012, Nima Tabatabaei.

5.2 Matched-Filtering and Truncated-Correlation Photothermal Coherence

Tomography

As discussed in previous sections, TCT and TWR incorporate matched filtering in order to probe deep in samples while maintaining acceptable axial resolution. However, their outputs are still 2-D images of light absorbers superposed on top of each other. Recently, a more optimized matched filter thermography technique known as truncated-correlation photothermal coherence tomography (TC-PCT) has been introduced which is capable of producing depth-resolved 3-D maps of defects [81-83]. Figure 5.8 shows the block diagram of the frequency-domain matched filtering for TC-PCT imaging. The TC-PCT concept was originated from linear frequency modulation (LFM) matched-filtering where a chirp of short optical pulses (E) with certain pulsewidth is used instead of the sinusoidal function of TWR to excite the sample and create photothermal waves. For 3-D reconstruction of absorbers, in TC-PCT, truncated reference chirps of pulsewidth W_T ($W_T < \text{excitation pulsewidth}$) with continuously variable delay (d) which are synthesized from the laser excitation chirp are generated. These truncated reference chirps may have a different pulsewidth known as sweep-delay step than the pulsewidth of the excitation waveform. The truncated reference chirps consist of an in-phase reference truncated signal (R_0) and its quadrature (R_{90}). The minimum value for the W_T is limited by the camera frame rate, and the maximum is limited by the time difference between the last two pulses in the up-chirp waveform. Each photothermal relaxation chirp captured by infrared camera is then cross-correlated with the truncated reference chirps in a pixel-by-pixel manner to generate two-dimensional axially resolved layer-by-layer images of the sample set by the reference phase delay. For example, cross-correlation of the first reference chirp $R_{1,0}$ in-phase with the thermal transient response (S) will yield a surface image of the sample. In the case of $R_{2,0}$, the outcome

will be depth-scaled subsurface planar image. As d increases, the depth of the layer below the surface also increases [82-84]. Therefore, in TC-PCT signal processing d controls the depth while W_T determines axial resolution. The output of TC-PCT consists of cross-correlation amplitude ($A_{CC,n}$) and cross-correlation phase ($\emptyset_{CC,n}$) that carry depth-integrated information:

$$A_{CC,n} = \sqrt{CC_{n,0}^2 + CC_{n,90}^2} \quad (5.3)$$

$$\emptyset_{CC,n} = \tan^{-1}(CC_{n,90}/CC_{n,0}) \quad (5.4)$$

Similar to TPLI, phase channel is less sensitive to variations in laser profile intensity and/or sample surface conditions since it is an emissivity normalized property.

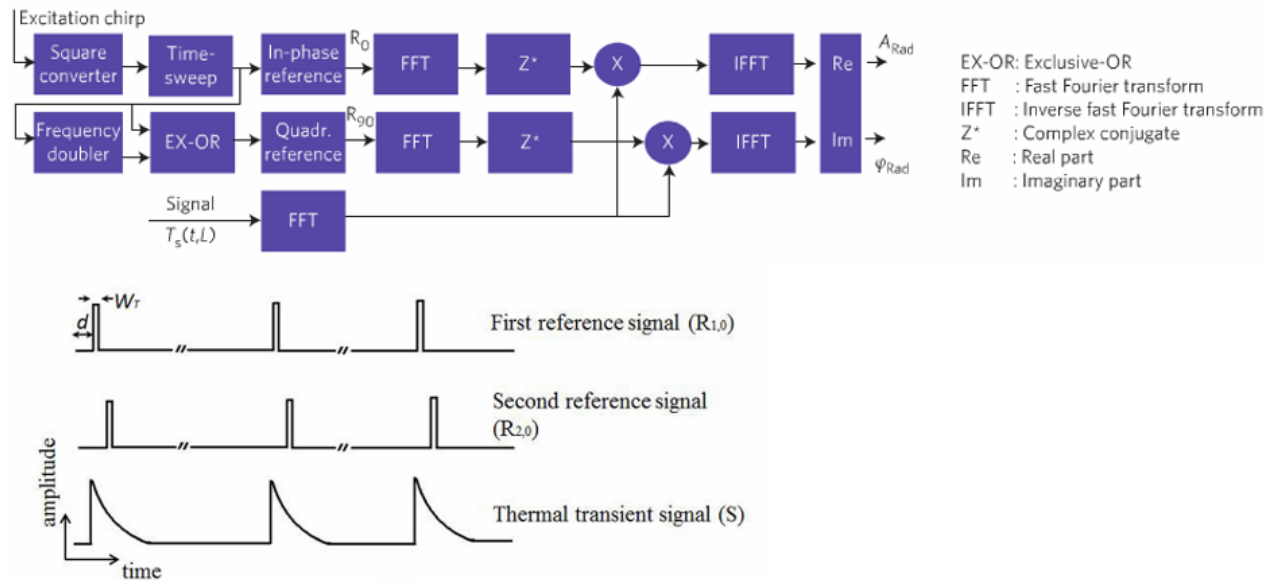


Figure 5.8: Flow diagram of the frequency domain TC-PCT algorithm. The cross-correlation of photothermal chirp with the truncated-reference chirp which are subjected to a controlled delay increment that determines penetration depth [82, 83], Copyright 2011, American Institute of Physics.

To estimate the mean diffusion depth corresponding to a given delay time following an impulsive thermal source on the surface of a semi-infinite solid, the following expression is used based on the semi-infinite solid temperature impulse response [82]:

$$\bar{z} = \frac{\int_0^{\infty} z e^{-z^2/\alpha t} dz}{\int_0^{\infty} e^{-z^2/4\alpha t} dz} = \frac{2\sqrt{\alpha t}}{\sqrt{\pi}} \quad (5.5)$$

where α is the thermal diffusivity of medium. For instance for healthy enamel, the thermal diffusivity is between $2.27 \times 10^{-7} - 4.7 \times 10^{-7} \text{ m}^2\text{s}^{-1}$ [17].

5.3 TC-PCT Instrumentation

Experimental results presented in this chapter were acquired using our collaborator's instrumentation at the University of Toronto. The experimental set up of TC-PCT [81-84] (Figure 5.9) consists of a mid-infrared (3-5 μm spectral band) camera that captures emitted radiation from a sample surface following optical excitation source by a pulsed diode laser (Jenoptic JOLD- 120- QPXF-2P). The laser beam is regulated by a laser driver (PCO-6131, Directed energy, Colorado, USA) that is controlled by a function generator (Keysight 33500B, USA) which generates the chirp waveform. The laser driver provides the current to the laser through a copper wire. In front of the laser, a diffuser (ED1-C20, Thorlabs Inc., New Jersey, USA) is mounted to uniformly illuminate the laser beam across the sample surface adjusted to get a 1.5~2.0 cm diameter beam size on the interrogated surface of the sample.

To generate 3-D images from TC-PCT, the desired excitation pulse width, experiment duration, start and end frequency are set on a designated LabVIEW code and the camera software records a video based on a user-specified integration time, frame rate and duration of excitation signal for each experiment. Then, all the recorded frames are exported in excel format in the desired

directory. After exporting all the raw camera frames, there are two post-processing steps to acquire TC-PCT slice images. In the first post-processing step, the algorithm generates a reference signal-which may have different pulsewidth known as sweep-delay-based on the excitation waveform and is synchronized with infrared camera frames [81]. In the second processing step, the reference signal passes through a delay-incremented unit, and the algorithm computes the quadrature of every shifted reference signal [81]. The program then measures the cross-correlation of thermal transient signal with delay-incremented and quadrature reference signals and generates the channels of TC-PCT (i.e. amplitude or phase).

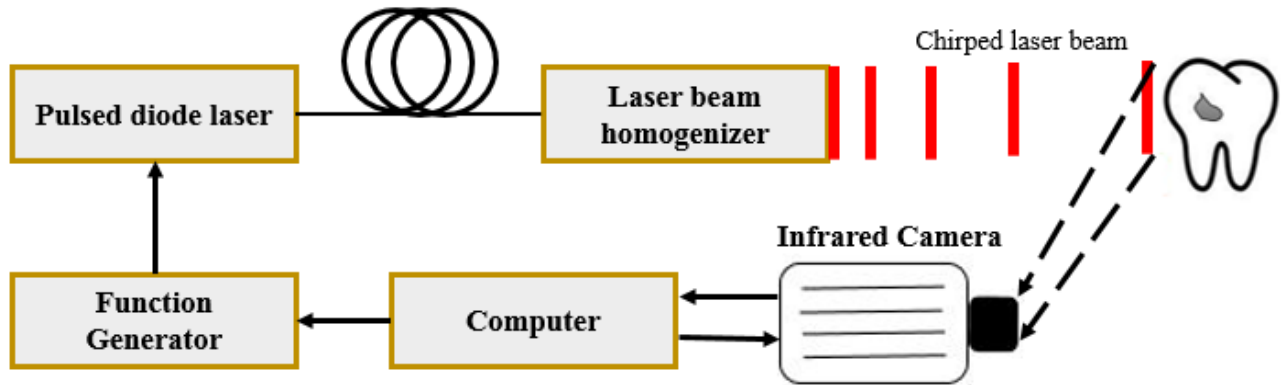


Figure 5.9: Experimental Setup of TC-PCT [81-84]

5.4 TC-PCT Experiments

Our first step in determining the feasibility of using TC-PCT in dental diagnostic imaging involved a healthy tooth with simulated subsurface cavities/defects. These defects normally show up in TPLI images as higher contrast areas, however, TPLI is not capable of determining the actual depth location of these defects. The output of TC-PCT, on the other hand, is a series of depth-resolved 2-D images, all of which can be stacked up to produce a 3-D image of the sample with depth as the third dimension [81]. To demonstrate tomographic capability of TC-PCT in visualizing dental defects, a relatively healthy tooth sample (sample 5 in Table 3.1; Figure 5.10(a)) was selected and two blind holes were drilled at the back of the sample. The front of the

sample was then imaged with both TPLI and TC-PCT. The dashed rectangle on the front of the sample in Figure 5.10(a) shows the field of view on which the TC-PCT imaging was done. The depth of hole 1 (shallow hole) is 7.59 mm leaving an intact thickness of approximately 0.63 mm from the surface of enamel. The depth of hole 2 (deep hole) is 7.34 mm leaving a intact thickness of 0.52 mm from the surface of enamel. Note that due to limited field of view of camera, only a portion of hole 2 is seen on TC-PCT amplitude and phase images.

For this sample, the surface was illuminated with a sweep range of 0.04-0.3 Hz, a duration of 35 s, and pulse duration of 30 ms. A sweep-delay of 30 ms was used to generate a stack of 86 2-D images. In 2-D amplitude and phase images of TPLI (Figure 5.10(b)-(c)), only hole 2 (deep hole) appears as high contrast area because it is closer to the surface of the enamel while hole 1 cannot reliably be seen due to its larger depth from the interrogated surface with respected to the thermal diffusion length at 2 Hz modulation frequency. For proper identification of hole 1 using TPLI, experiments at multiple lower frequencies must be carried out which increases the measurement time and thus limits the clinical feasibility of using TPLI. On the other hand, in 2-D planar amplitude and phase slices of TC-PCT (Figure 5.11(a)-(b)), both holes can be detected. The fact that holes cannot be seen on the surface planar images of the sample (slices 1 to 10) speaks to the depth-selective nature of TC-PCT and its ability in revealing the intact enamel layers above the holes. The high amplitude and phase values emerging from the holes can be seen after we move in-depth into the sample.

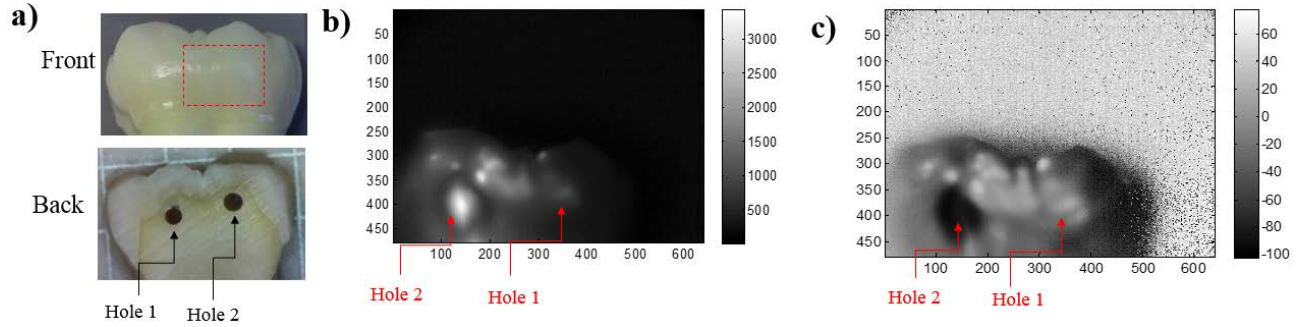


Figure 5.10: (a) Front and back photographs of the sample (b) amplitude and (c) phase images of TPLI

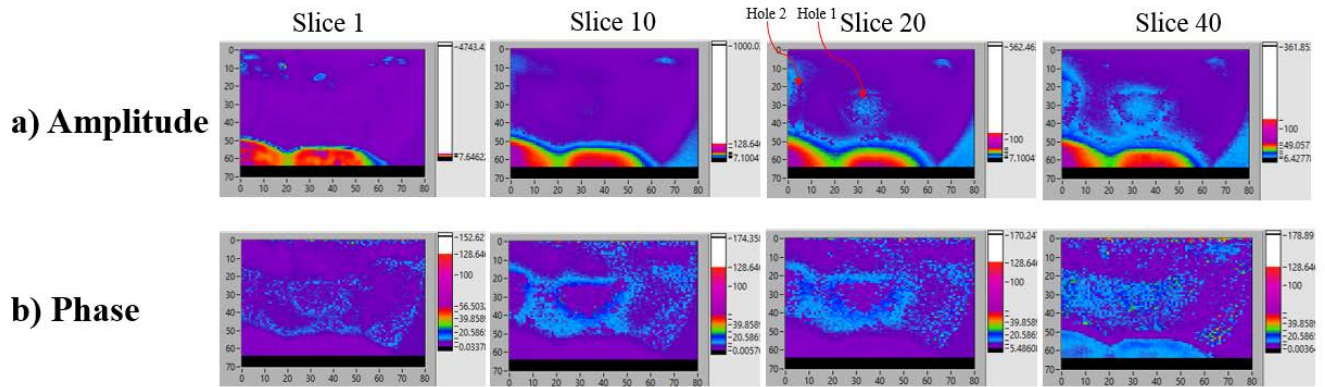


Figure 5.11: (a) the 2-D TC-PCT amplitude and (b) phase planar slices of the sample

The relative depths of the two holes can also be retrieved from the TC-PCT images. TC-PCT's amplitude and phase plots in the intact thickness of the sample (Figure 5.12) show a relatively constant contrast down to slices 27 and 15, respectively. Slices appearing after this intact thickness mark approximately where the two holes start to appear due to the significant change in amplitude and phase values, hence, showing the depth-selective nature of TC-PCT. In 3-D amplitude and phase channels of TC-PCT (Figure 5.13), the emergence of the two holes can be clearly seen. In addition, using TC-PCT dataset we can determine the slice where the holes start to appear and hence, determine the mean thermal diffusion length of each hole. Since the contrast change of hole 1 occurs at approximately slice 27, we can derive the mean thermal diffusion length of hole 1 by using equation 5.5 and thermal diffusivity of $4.7 \times 10^{-7} m^2 s^{-1}$ as:

$$\bar{z} = \frac{2 * \sqrt{4.7 \times 10^{-7} \text{ m}^2\text{s}^{-1} * 0.03\text{s} * 27}}{\sqrt{\pi}} = 0.696 \text{ mm}$$

For hole 2, the contrast change happens at slice 15, and therefore, the mean thermal length is:

$$\bar{z} = \frac{2 * \sqrt{4.7 \times 10^{-7} \text{ m}^2\text{s}^{-1} * 0.03\text{s} * 15}}{\sqrt{\pi}} = 0.518 \text{ mm}$$

The mean thermal diffusion length for hole 1 and hole 2 are therefore, 0.696 mm and 0.518 mm, respectively. Comparing the calculated values to the actual intact thickness of 0.63 mm and 0.52 mm for hole 1 and hole 2, the percentage error can be determined for both holes:

$$\%_{error} (\text{hole 1}) = \frac{0.696 - 0.63}{0.63} \times 100 = 10.4\%$$

$$\%_{error} (\text{hole 2}) = \frac{0.518 - 0.52}{0.52} \times 100 = 0.38\%$$

The obtained results from this experiment, therefore, suggest the feasibility of performing dental TC-PCT imaging for detecting sharp and well-defined defects such as hidden cavities and cracks in dental enamel or sealants.

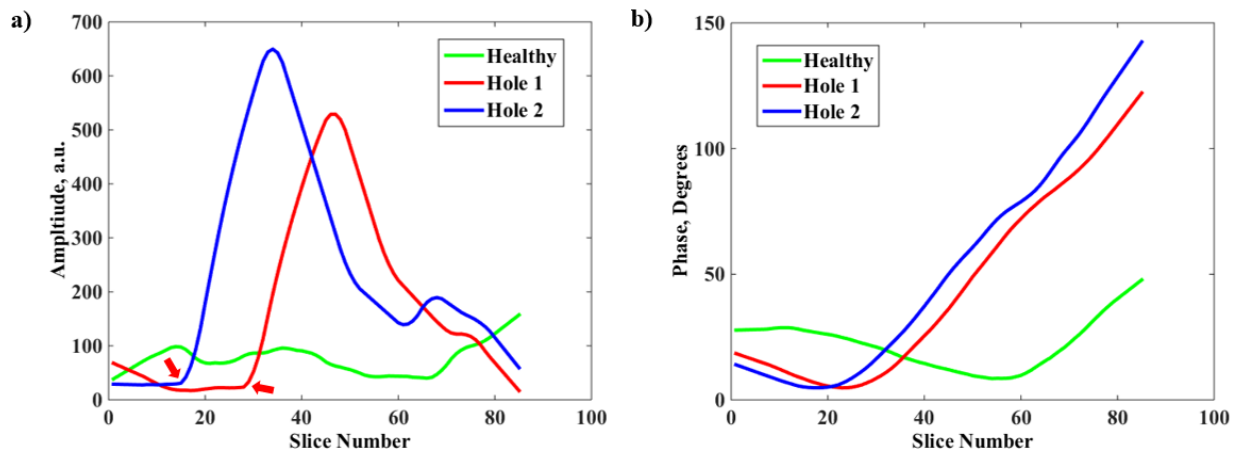


Figure 5.12: (a) Amplitude and (b) phase plots of healthy and defective regions versus slice number

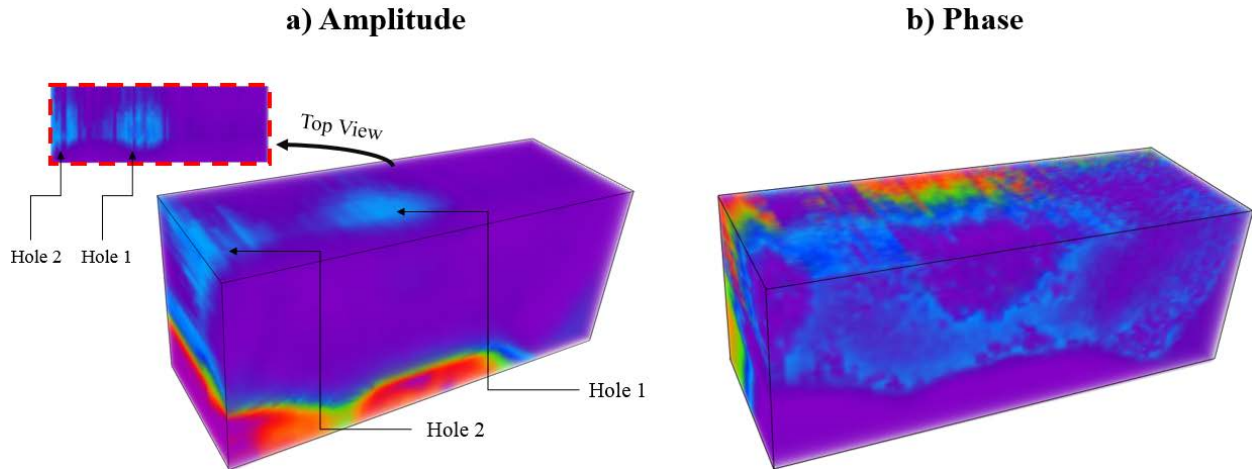


Figure 5.13: 3-D visualization of the stacked slices in TC-PCT channels

The purpose of the next experiment was to explore if TC-PCT can visualize early demineralization in tooth in 3-D. As such, sample 3 (also introduced in section 4.2) was a suitable choice for this study as in section 4.2 we observed that the presence of demineralization was not detectable in 2- and 4-day treated windows in OCT images. Additionally, in TPLI images of the sample, the contrast of 2 and 4 days were equal and only 8 day window showed a significant increase in contrast. Therefore, examining the ability of TC-PCT in resolving the 3 demineralization windows of this challenging sample in 3-D was highly desired. Since the region of interest was very close to the interrogated surface of sample, the experimental excitation pulse chip parameters for this study were selected as: starting frequency 0.2 Hz, ending frequency 0.6 Hz, chirp period 18 s, and excitation pulse width of 30 ms. A sweep-delay of 10 ms was used to generate a stack of 272 2-D images.

The 3-D images of Figure 5.14 show that in both amplitude and phase channels of TC-PCT, 8-day window contains the highest contrast compared to 2- and 4- day treated windows. The 4-day treated window contains a higher contrast compared to 2-day, but lower contrast compared to 8-day treated windows. Lastly, 2-day treated window contains the lowest contrast in comparison to the other treated windows; yet, it can still be distinguished from surrounding intact enamel.

Therefore, visual observation suggest that each one of the treated windows can be detected and differentiated from each other in the 3-D images of TC-PCT. Due to the extent of demineralization in 8-day window and thus significant amount of light absorption, however, the contrast at the center of 8-day window remains saturated in all depth slices. But, in 3-D images of TC-PCT, 2-day and 4-day windows lose their contrast and reach a contrast that is close to that of the healthy region at deep slices. On the other hand, the phase channel of TC-PCT offers the highest dynamic range due to its emissivity-normalized nature and the extent of each demineralization window into enamel is well displayed.

Figure 5.15 plots show the change in amplitude and phase values in each of the demineralized windows. It can be seen that at locations where there were less demineralization, such as 2-day window, after the initial slices the defect contrast diminishes to indicate a shallow defect. The preliminary results obtained from this experiment suggest feasibility of resolving early dental caries in 3-D using the TC-PCT method. In clinical practice, 3-D visualization of early caries is expected to aid clinicians in making better interventional and preventive decisions.

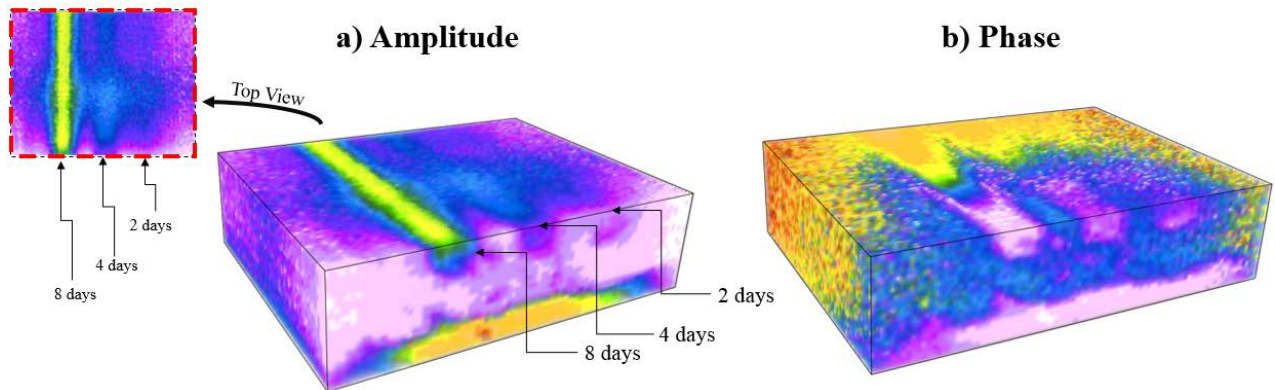


Figure 5.14: 3-D visualization of the stacked slices in (a) amplitude and (b) phase channels

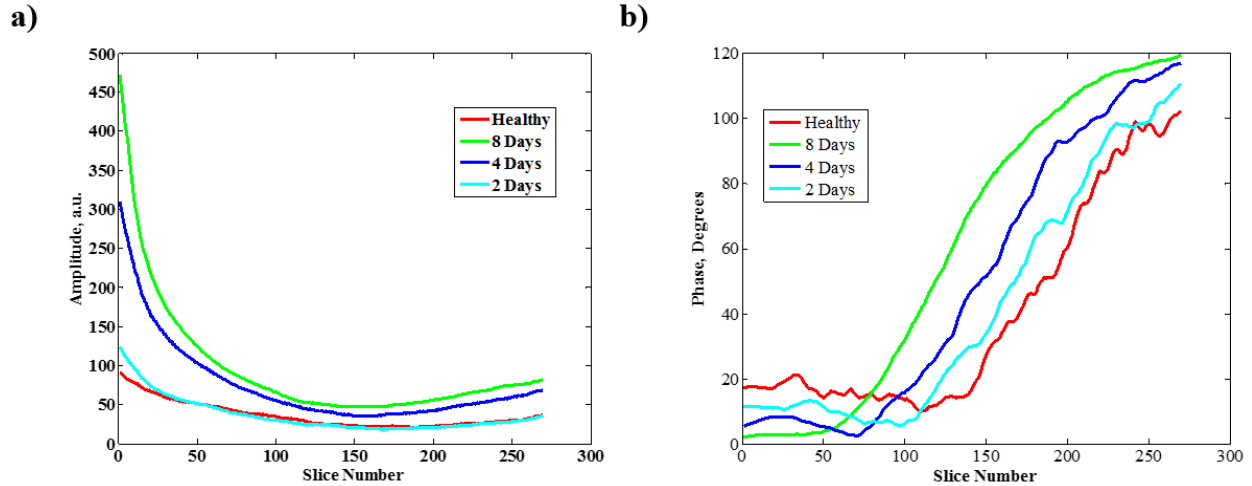


Figure 5.15: (a) Amplitude and (b) phase plots of healthy and demineralized regions versus slice number

Our next step in exploring the feasibility of using TC-PCT for early caries detection was to study the effects of experimental parameters on image quality. As such, a healthy tooth sample (sample 6 in Table 3.1) with two artificially-induced caries for 3 and 7 days on the same surface was chosen. Table 5.1 shows a series of 5 experiments/imaging studies that were performed for studying the effects of imaging parameters such as frequency, sweep-delay, and excitation pulse width.

Table 5.1: TC-PCT Imaging Study Parameters

Experiment	Frame Rate (Hz)	Frequency (Hz)	Duration (s)	Sweep-Delay (ms)	Excitation Pulse Width (ms)
1	104	0.1-0.3	21	50	10
2	104	0.1-0.3	21	50	30
3	104	0.1-0.3	21	50	150
4	104	0.05-0.15	37	50	30
5	104	0.05-0.15	37	200	30

Experiments 1, 2, and 3 looked into the effect of various excitation pulse widths on image quality and visualization of caries (Figure 5.16(a)-(f)). In 3-D amplitude and phase tomograms of these

experiments, it can be observed that there is an increased intensity/contrast achieved by increasing the excitation pulse width as more optical energy is converted to heat. With higher excitation pulse widths, the amplitude and phase images exhibit higher SNR for visualization of the artificially-induced caries. However, tomograms suggest that by increasing the excitation pulse width, more thermal energy gets accumulated at caries, enhancing lateral heat flow and perception of a larger defect size [82]. Therefore, there is an interplay between intensity and precision of defining the geometry of defects. The effect of excitation pulse width on lateral heat flow can also be seen in the top view of the 3-D tomograms in Figure 5.16(g).

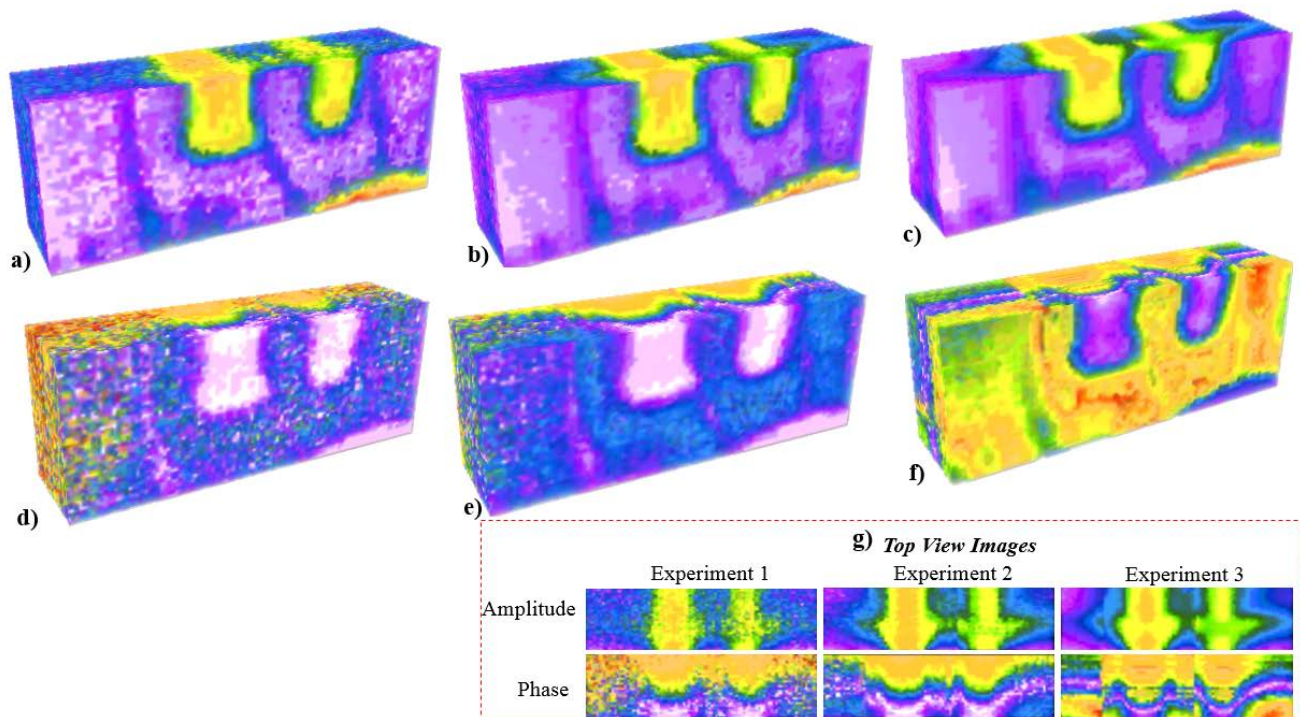


Figure 5.16: 3-D amplitude tomograms of (a) experiment 1, (b) experiment 2, and (c) experiment 3 along with 3-D phase tomograms of (d) experiment 1, (e) experiment 2, and (f) experiment 3. (g) Top view of phase and amplitude 3-D tomograms for better visualization of the lateral heat flow and size of the caries.

Experiment 4 maintained the same experimental parameters to that of experiment 2. However, to enhance the depth range, parameters were modified by using lower starting and ending frequencies of 0.05 and 0.5Hz, respectively. As it can be seen in Figure 5.17(a)-(d), when using a chirp laser beam, lowering starting and end frequencies results in an increase in thermal diffusion length, thus enabling detection of deeper features in samples that may not otherwise be visible using higher frequencies (e.g., feature shown by red arrow in the amplitude tomogram of experiment 4). Although, low-frequency thermal waves can penetrate deep into the sample, they lack the desired depth resolution [83]. Increasing the starting and end frequencies to 0.1 and 0.3 Hz as seen in experiment 2 corresponds to seeing features with shallower depths (i.e. thinner 3-D images) and a decrease in thermal diffusion length [74]. Changing the frequencies, however, did not influence the visualization of the caries. Only at higher frequencies the artificial caries are seen in more details (Figure 5.17(e)).

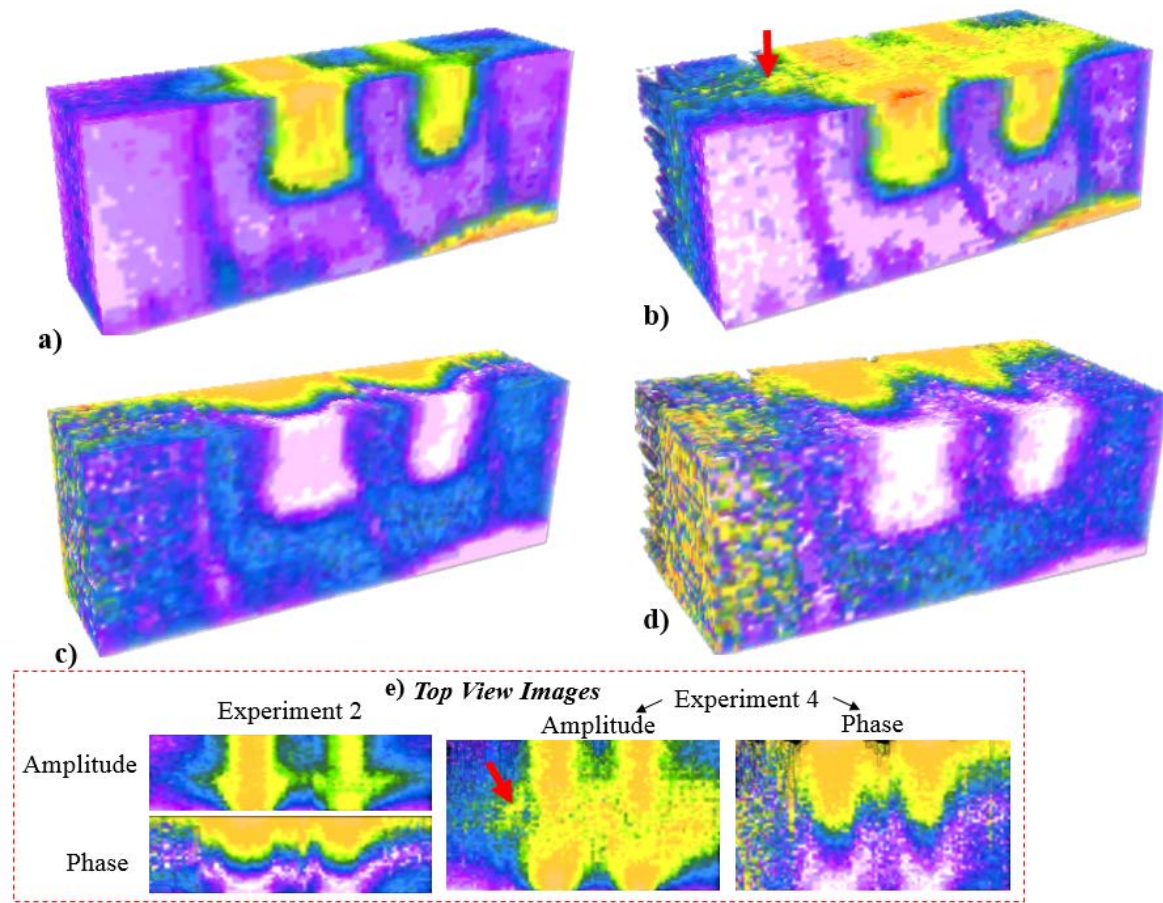


Figure 5.17: 3-D amplitude tomograms of (a) experiment 2 and (b) experiment 4, along with 3-D phase tomograms of (c) experiment 2 and (d) experiment 4. (e) Top view of phase and amplitude 3-D tomograms

Experiment 5 was performed to observe the effect of sweep-delay on the quality TC-PCT images (Figure 5.18). All parameters in this experiment were kept constant as experiment 4, except for sweep-delay. To observe the change in visualization of the caries, a longer sweep-delay step (200 ms) was used. A sweep-delay of 50 ms (experiment 4) generates a stack of 101 2-D images while changing the sweep-delay to 200 ms (experiment 5) produces 24 2-D images. That is, by increasing the sweep-delay, each of the resultant 2-D images deliver larger slice width (thicker TC-PCT slice) and higher energy localization leading to higher SNR for each slice [81]. On the other hand, the depth resolution (thinness of TC-PCT slices) degrades as sweep-delay increases [82-84]. In terms of caries detection, our preliminary experiments suggest that short sweep-delay provides better visualization of caries with sufficient SNR.

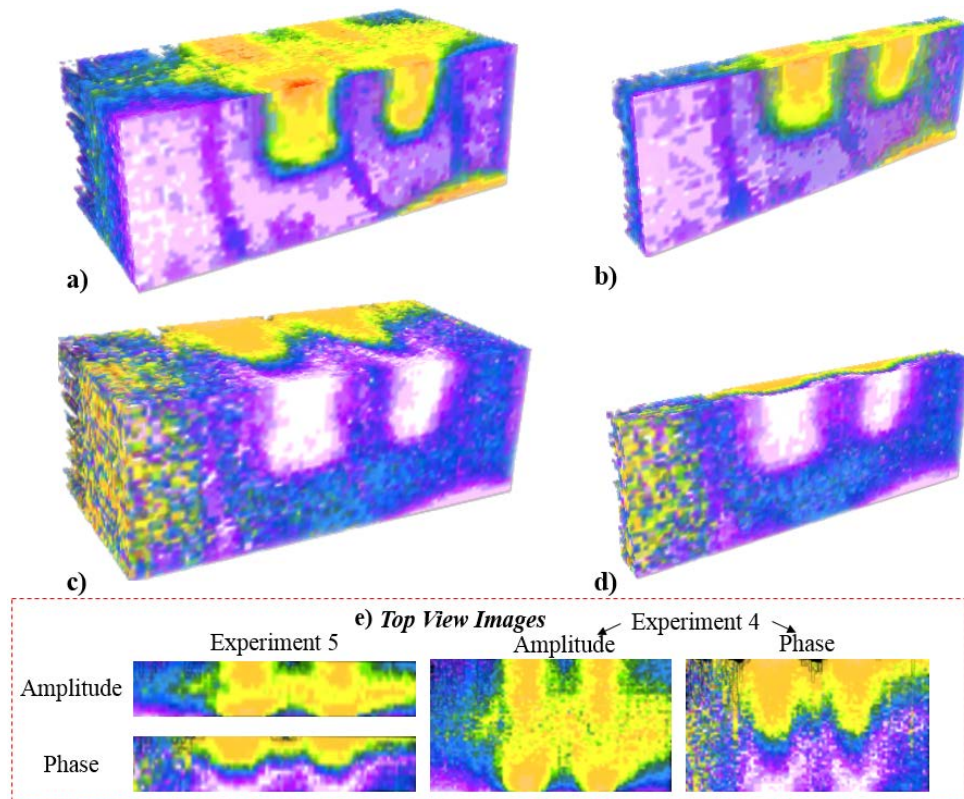


Figure 5.18: 3-D amplitude tomograms of (a) experiment 4 and (b) experiment 5, along with 3-D phase tomograms of (c) experiment 4 and (d) experiment 5. (e) Top view of phase and amplitude 3-D tomograms.

In summary, the recommendations on suitable system parameters for optimized detection of early dental caries include the parameters studied in experiment 2. Because early caries are subsurface features that are located close to the surface of enamel, high frequencies are better suited as the thermal diffusion length is inversely proportional to the square root of frequency. In addition, it is recommended to keep the laser intensity/excitation pulse width at a range that provides a reasonable SNR in visualization of early caries similar to the value set in experiment 2, but also not exceed the maximum permissible exposure induced in tooth. In terms of setting a feasible sweep-delay range, lower values increase depth resolution which is more desired in early detection of caries.

5.5 Summary of the TC-PCT Experiments

In summary, TC-PCT was applied to image artificially-induced caries and invisible defects in tooth such as holes. Compared to OCT, TC-PCT has much deeper subsurface penetration depth and ability to detect caries at very early stages of formation due to its intrinsic enhanced sensitivity and specificity as a light absorption based imaging modality. Similar to OCT, TC-PCT has the ability to visualize dental defects in 3-D and thus determine lesion/defect depth. However, resolution of OCT is significantly better than TC-PCT. Compared to TPLI, the most important advantage of TC-PCT is its ability to produce tomographic images, enabling quantification of lesion's geometric parameters such as depth. Therefore, our preliminary experimentations indicate that TC-PCT imaging of dental defects is feasible and potentially superior to both OCT and TPLI as it offers the key advantages of both technologies with minimal compromise.

Chapter 6

Conclusion and Future Directions

This chapter provides the conclusion obtained in this research project. Potential future works in this area are also discussed.

6.1 Conclusion

In this thesis, a comprehensive comparison was conducted to compare the detection performance of OCT and TPLI as two promising early dental caries detection imaging modalities based on enhancement of light scattering and absorption in caries, respectively. Through experimentation and statistical analysis, we demonstrated that the molecular-contrast based TPLI imaging technology outperforms OCT in terms of detection threshold, detection sensitivity, and specificity for detection of early caries, demonstrating the more specific and sensitive nature of light absorption based imaging modalities. These enhancements in performance are believed to be key to the success of preventive measures in order to heal or arrest caries. Since TPLI inherently involves a compromise between inspection depth and imaging resolution, its modification to a tomographic system with enhance depth-resolution, such as the TC-PCT system used in chapter 5, is highly desired. Therefore, in the last part of this thesis we demonstrated feasibility of achieving light-absorption based tomographic imaging using TC-PCT. TC-PCT simultaneously offers the major advantages of OCT and TPLI by providing 3-D maps based on absorption of light. In this thesis, TC-PCT's depth-resolved imaging capability was tested through preliminary experimentation on simulated hidden defects in tooth and artificially-induced caries. Results suggest that TC-PCT can successfully reconstruct maps of light absorbing/heat impeding defects in three-dimensions, enabling quantification of

geometrical parameters of deep defects otherwise not possible by TPLI and OCT. In addition, preliminary experimentation conducted using TC-PCT revealed a matrix of system parameters suitable for diagnosis and visualization of dental caries.

Despite the promising results obtained from TC-PCT experiments, one shortcoming which has to be addressed is the laser intensity. Increasing the laser intensity or excitation pulse width in TC-PCT increases heat generation, therefore, producing strong thermal waves that exceed the maximum permissible exposure induced in a tooth. Therefore, the best compromise between the laser intensity and expected exposure duration should be found with more experimentation. Furthermore, existing TC-PCT systems incorporate very powerful lasers ($>100\text{W}$) which are very unlikely to be approved for clinical use.

Better and more efficient optical delivery parameters can be utilized to reduce the laser power requirement for creating diagnostic images with acceptable quality. For future experiments of similar kind, we should investigate and utilize the minimum laser power which results in acceptable image quality. In addition, the entire diameter of laser beam should be illuminated on the sample by adjusting the distance between the optical fiber and the sample.

6.2 Future Directions

The future direction for this project would be to expand an already existing TPLI technology that detects early dental caries in the LWIR band into a 3-D molecular contrast imaging technology that would outperform TC-PCT which detects early caries in the MWIR band. Studies have proved thermophotonic detection of early dental caries in the LWIR band results in improvement in the detection sensitivity compared to system detecting in the MWIR band [85].

Another future direction would be to explore the possibility of performing TC-PCT using low-cost cellphone attachment infrared cameras [61] for 3-D diagnostic imaging of biological tissues or non-destructive testing of manufactured parts and civil structures.

Development of photothermal optical coherence tomography (PT-OCT) is another potential venue to explore in which light absorption signature are probed through the phase information of OCT interferometric signals.

Lastly, since the extracted teeth were collected anonymously, the age of the samples were unknown. While mechanical and optical properties of tooth vary based on person's demographics and oral hygiene, the purpose of this study was to simply choose healthy teeth samples with no visible sign of defect and create artificial caries on them to compare capabilities of the two systems in detection of early caries. Therefore, the influence of age of the extracted teeth samples were not considered in this work and can be considered a potential future research direction.

References

- [1] "Preventing dental caries," M. Y. University, P. National Center for Chronic Disease, and P. Health, Eds., ed: CDC, [National Center for Chronic Disease Prevention and Health Promotion], U.S. Dept. of Health and Human Services.
- [2] E. A. M. Kidd, "Essentials of dental caries the disease and its management," U. Oxford Scholarship Online - York, Ed., ed: Oxford University Press.
- [3] J. D. Featherstone, "Dental caries: a dynamic disease process," *Aust Dent J*, vol. 53, pp. 286-91, Sep 2008.
- [4] R. P Ellwood, J. Gomez, and I. A Pretty, *Caries Clinical Trial Methods for the Assessment of Oral care Products in the 21st century* vol. 24, 2012.
- [5] S. O. Griffin, E. Regnier, P. M. Griffin, and V. Huntley, "Effectiveness of fluoride in preventing caries in adults," *J Dent Res*, vol. 86, pp. 410-5, May 2007.
- [6] J. D. Bader and D. A. Shugars, "The evidence supporting alternative management strategies for early occlusal caries and suspected occlusal dentinal caries," *J Evid Based Dent Pract*, vol. 6, pp. 91-100, Mar 2006.
- [7] P. E. Petersen, D. Bourgeois, H. Ogawa, S. Estupinan-Day, and C. Ndiaye, "The global burden of oral diseases and risks to oral health," *Bull World Health Organ*, vol. 83, pp. 661-9, Sep 2005.
- [8] A. Nanci, *Ten Cate's Oral Histology - E-Book: Development, Structure, and Function*, 9 ed.: Elsevier Health Sciences, 2017.
- [9] O. Fejerskov and E. Kidd, *Dental Caries: The Disease and Its Clinical Management*, 3 ed.: John Wiley & Sons, 2004.

- [10] *Sangi's Pioneer Technology*. Available: http://www.sangi-co.com/en/technology/consumer_benefits/index.html
- [11] A. Elgreatly, "Management of initial caries lesions: Iowa survey," Master of Science, Oral Science, The University of Iowa, 2017.
- [12] K. Shivakumar, S. Prasad, and G. Chandu, "International Caries Detection and Assessment System: A new paradigm in detection of dental caries," *Journal of Conservative Dentistry*, vol. 12, pp. 10-16, 2009.
- [13] M. Madhumitha, P. V. Ratna, and S. R, "Diagnostic methods for early detection of dental caries - A review," *International Journal of Pedodontic Rehabilitation*, vol. 1, pp. 29-36, 2016.
- [14] S. C. White and M. J. Pharoah, *Oral Radiology: Principles and Interpretation*: Mosby, 2000.
- [15] N. Tabatabaei, *Development of Frequency and Phase Modulated Thermal-wave Methodologies for Materials Non-destructive Evaluation and Thermophotonic Imaging of Turbid Media*: Library and Archives Canada = Bibliothèque et Archives Canada, 2012.
- [16] A. Matvienko, A. Mandelis, R. J. Jeon, and S. H. Abrams, "Theoretical analysis of coupled diffuse-photon-density and thermal-wave field depth profiles photothermally generated in layered turbid dental structures," *Journal of Applied Physics*, vol. 105, p. 102022, 2009.
- [17] A. Hellen, "Quantitative Evaluation of Simulated Enamel Demineralization and Remineralization Using Photothermal Radiometry and Modulated Luminescence," Master's, Dentistry, University of Toronto, 2010.

- [18] A. Ojaghi, "Long-Wave Infrared Thermophotonic Imaging of Demineralization in Dental Hard Tissues," Master's, Mechanical Engineering, York University, 2016.
- [19] L. Bachmann, R. Diebold, R. Hibst, and D. M. Zezell, "Infrared Absorption Bands of Enamel and Dentin Tissues from Human and Bovine Teeth," *Applied Spectroscopy Reviews*, vol. 38, pp. 1-14, 2003/01/04 2003.
- [20] M. J. S.C. White, Pharoah, *Oral Radiology: Principles and Interpretation*, 7th ed.: Elsevier Health Sciences, 2013.
- [21] A. P. Dhawan, B. D. Alessandro, and X. Fu, "Optical Imaging Modalities for Biomedical Applications," *IEEE Reviews in Biomedical Engineering*, vol. 3, pp. 69-92, 2010.
- [22] G. M. Davies, H. V. Worthington, J. E. Clarkson, P. Thomas, and R. M. Davies, "The use of fibre-optic transillumination in general dental practice," *Br Dent J*, vol. 191, pp. 145-7, Aug 11 2001.
- [23] S. C. Berg, J. M. Stahl, W. Lien, C. M. Slack, and K. S. Vandewalle, "A clinical study comparing digital radiography and near-infrared transillumination in caries detection," *Journal of Esthetic and Restorative Dentistry*, vol. 30, pp. 39-44, 2018.
- [24] J. D. Bader, D. A. Shugars, and A. J. Bonito, "A systematic review of the performance of methods for identifying carious lesions," *J Public Health Dent*, vol. 62, pp. 201-13, Fall 2002.
- [25] I. A. Pretty, "Caries detection and diagnosis: novel technologies," *J Dent*, vol. 34, pp. 727-39, Nov 2006.
- [26] K. Angelino, D. A. Edlund, and P. Shah, "Near-Infrared Imaging for Detecting Caries and Structural Deformities in Teeth," *IEEE Journal of Translational Engineering in Health and Medicine*, vol. 5, p. 2300107.

- [27] S. Chung, D. Fried, M. Staninec, and C. L. Darling, "Near infrared imaging of teeth at wavelengths between 1200 and 1600 nm," *Proceedings of SPIE--the International Society for Optical Engineering*, vol. 7884, p. 78840X, 2011.
- [28] M. K. Jeffcoat and M. S. Reddy, "Advances in measurements of periodontal bone and attachment loss," *Monogr Oral Sci*, vol. 17, pp. 56-72, 2000.
- [29] S. Tranæus, R. Heinrich-Weltzien, J. Kühnisch, L. Stösser, and B. Angmar-Månsson, "Potential Applications and Limitations of Quantitative Light-induced Fluorescence in Dentistry," *Medical Laser Application*, vol. 16, pp. 195-204, 2001/01/01/ 2001.
- [30] E. de Josselin de Jong, S. M. Higham, P. W. Smith, C. J. van Daelen, and M. H. van der Veen, "Quantified light-induced fluorescence, review of a diagnostic tool in prevention of oral disease," *Journal of Applied Physics*, vol. 105, p. 102031, 2009/05/15 2009.
- [31] H. Nokhbatolfoghahaie, M. Alikhasi, N. Chiniforush, F. Khoei, N. Safavi, and B. Yaghoub Zadeh, "Evaluation of Accuracy of DIAGNOdent in Diagnosis of Primary and Secondary Caries in Comparison to Conventional Methods," *Journal of Lasers in Medical Sciences*, vol. 4, pp. 159-167, Autumn 2013.
- [32] L. Fung, R. Smales, H. Ngo, and G. Moun, "Diagnostic comparison of three groups of examiners using visual and laser fluorescence methods to detect occlusal caries in vitro," *Aust Dent J*, vol. 49, pp. 67-71; quiz 101, Jun 2004.
- [33] A. M. Costa, L. M. Paula, and A. C. Bezerra, "Use of Diagnodent for diagnosis of non-cavitated occlusal dentin caries," *J Appl Oral Sci*, vol. 16, pp. 18-23, Jan-Feb 2008.
- [34] C. Kouchaji, "Comparison between a laser fluorescence device and visual examination in the detection of occlusal caries in children," *The Saudi Dental Journal*, vol. 24, pp. 169-174.

- [35] Y.-S. Hsieh, Y.-C. Ho, S.-Y. Lee, C.-C. Chuang, J.-c. Tsai, K.-F. Lin, *et al.*, "Dental Optical Coherence Tomography," *Sensors*, vol. 13, p. 8928, 2013.
- [36] M.-T. Tsai, H.-C. Lee, C.-K. Lee, C.-H. Yu, H.-M. Chen, C.-P. Chiang, *et al.*, "Effective indicators for diagnosis of oral cancer using optical coherence tomography," *Optics Express*, vol. 16, pp. 15847-15862, 2008/09/29 2008.
- [37] J. Espigares, A. Sadr, H. Hamba, Y. Shimada, M. Otsuki, J. Tagami, *et al.*, "Assessment of natural enamel lesions with optical coherence tomography in comparison with microfocus x-ray computed tomography," *J Med Imaging (Bellingham)*, vol. 2, p. 014001, Jan 2015.
- [38] Y. Shimada, A. Sadr, M. F. Burrow, J. Tagami, N. Ozawa, and Y. Sumi, "Validation of swept-source optical coherence tomography (SS-OCT) for the diagnosis of occlusal caries," *J Dent*, vol. 38, pp. 655-65, Aug 2010.
- [39] C. Sinescu, M. L. Negrutiu, C. Todea, C. Balabuc, L. Filip, R. Rominu, *et al.*, "Quality assessment of dental treatments using en-face optical coherence tomography," *J Biomed Opt*, vol. 13, p. 054065, Sep-Oct 2008.
- [40] D. Fried, J. Xie, S. Shafi, J. D. Featherstone, T. M. Breunig, and C. Le, "Imaging caries lesions and lesion progression with polarization sensitive optical coherence tomography," *J Biomed Opt*, vol. 7, pp. 618-27, Oct 2002.
- [41] H. Schneider, K.-J. Park, M. Häfer, C. Rüger, G. Schmalz, F. Krause, *et al.*, "Dental Applications of Optical Coherence Tomography (OCT) in Cariology," *Applied Sciences*, vol. 7, 2017.

- [42] L. L. Otis, M. J. Everett, U. S. Sathyam, and B. W. Colston, "OPTICAL COHERENCE TOMOGRAPHY: A NEW IMAGING: TECHNOLOGY FOR DENTISTRY," *The Journal of the American Dental Association*, vol. 131, pp. 511-514, 2000/04/01/ 2000.
- [43] B. Wolff, A. Matet, V. Vasseur, J. A. Sahel, and M. Mauget-Faysse, "En Face OCT Imaging for the Diagnosis of Outer Retinal Tubulations in Age-Related Macular Degeneration," *J Ophthalmol*, vol. 2012, p. 542417, 2012.
- [44] D. Fried, M. Staninec, C. L. Darling, K. H. Chan, and R. B. Pelzner, "Clinical Monitoring of Early Caries Lesions using Cross Polarization Optical Coherence Tomography," *Proc SPIE Int Soc Opt Eng*, vol. 8566, Mar 25 2013.
- [45] D. Fried, M. Staninec, C. Darling, H. Kang, and K. Chan, "Monitoring tooth demineralization using a cross polarization optical coherence tomographic system with an integrated MEMS scanner," *Proc SPIE Int Soc Opt Eng*, vol. 8208, Feb 9 2012.
- [46] J. C. Simon, H. Kang, M. Staninec, A. T. Jang, K. H. Chan, C. L. Darling, *et al.*, "Near-IR and CP-OCT imaging of suspected occlusal caries lesions," *Lasers Surg Med*, vol. 49, pp. 215-224, Mar 2017.
- [47] A. Baumgartner, S. Dichtl, C. K. Hitzenberger, H. Sattmann, B. Robl, A. Moritz, *et al.*, "Polarization-Sensitive Optical Coherence Tomography of Dental Structures," *Caries Research*, vol. 34, pp. 59-69, 2000.
- [48] J. Walther, J. Golde, L. Kirsten, F. Tetschke, F. Hempel, T. Rosenauer, *et al.*, "In vivo imaging of human oral hard and soft tissues by polarization-sensitive optical coherence tomography," *J Biomed Opt*, vol. 22, pp. 1-17, Dec 2017.

- [49] P. Ngaotheppitak, C. L. Darling, and D. Fried, "Measurement of the severity of natural smooth surface (interproximal) caries lesions with polarization sensitive optical coherence tomography," *Lasers Surg Med*, vol. 37, pp. 78-88, Jul 2005.
- [50] J. Golde, F. Tetschke, J. Walther, T. Rosenauer, F. Hempel, C. Hannig, *et al.*, "Detection of carious lesions utilizing depolarization imaging by polarization sensitive optical coherence tomography," *J Biomed Opt*, vol. 23, pp. 1-8, Jan 2018.
- [51] Y. Shimada, H. Nakagawa, A. Sadr, I. Wada, M. Nakajima, T. Nikaido, *et al.*, "Noninvasive cross-sectional imaging of proximal caries using swept-source optical coherence tomography (SS-OCT) in vivo," *Journal of Biophotonics*, vol. 7, pp. 506-513, 2014.
- [52] G. M. C. T. Astarita, *Infrared Thermography for Thermo-Fluid-Dynamics*, 1st ed. Berlin, Germany: Springer-Verlag Berlin Heidelberg, 2013.
- [53] W. W. O. Breitenstein, M. Langenkamp, *Lock-in Thermography: Basics and Use for Evaluating Electronic Devices and Materials*, 1st ed. Berlin, Germany: Springer-Verlag Berlin Heidelberg, 2003.
- [54] N. Tabatabaei, A. Mandelis, and B. T. Amaechi, "Thermophotonic lock-in imaging of early demineralized and carious lesions in human teeth," *J Biomed Opt*, vol. 16, p. 071402, Jul 2011.
- [55] Y.-K. An, J. Min Kim, and H. Sohn, "Laser lock-in thermography for detection of surface-breaking fatigue cracks on uncoated steel structures," *NDT & E International*, vol. 65, pp. 54-63, 2014/07/01/ 2014.

- [56] C. Meola, G. M. Carlomagno, A. Squillace, and A. Vitiello, "Non-destructive evaluation of aerospace materials with lock-in thermography," *Engineering Failure Analysis*, vol. 13, pp. 380-388, 2006/04/01/ 2006.
- [57] C. John and A. Salerno, "Raw data set of thermal wave propagation in hard dental tissues," in *Proc. of 11th Int. Symp. and Exhibition for Computer Assisted Radiology (CAR97)*, 1997, p. 98601952.
- [58] C. John, D. Wu, A. Salerno, G. Busse, and C. Löst, "Nondestructive Characterization of Materials VIII," S. US, Ed., ed, 1998, pp. 757-762.
- [59] N. Tabatabaei, A. Mandelis, M. Dehghany, K. H. Michaelian, and B. T. Amaechi, "On the sensitivity of thermophotonic lock-in imaging and polarized Raman spectroscopy to early dental caries diagnosis," *Journal of biomedical optics*, vol. 17, pp. 0250021-0250025, Feb 2012.
- [60] A. Ojaghi, A. Parkhimchyk, and N. Tabatabaei, "First step toward translation of thermophotonic lock-in imaging to dentistry as an early caries detection technology," *Journal of biomedical optics*, vol. 21, pp. 096003-096003, Sep 1 2016.
- [61] M. Razani, A. Parkhimchyk, and N. Tabatabaei, "Lock-in thermography using a cellphone attachment infrared camera," *AIP Advances*, *In Press*, 2018.
- [62] M. Streza, B. Belean, I. Hodisan, and C. Prejmorean, "Improving lock-in thermography detection of microgaps located at the tooth-filling interface using a phase versus amplitude image signal extraction approach," *Measurement*, vol. 104, pp. 21-28, 2017/07/01/ 2017.

- [63] A. Ojaghi, A. Parkhimchyk, and N. Tabatabaei, "First step toward translation of thermophotonic lock-in imaging to dentistry as an early caries detection technology," *J Biomed Opt*, vol. 21, p. 96003, Sep 1 2016.
- [64] A. Ojaghi, A. Parkhimchyk, and N. Tabatabaei, "A pilot study on the detection of early proximal and occlusal dental caries using long-wave infrared thermophotonic imaging," in *Lasers in Dentistry XXII*, 2016.
- [65] M. E. Brezinski, *Optical Coherence Tomography: Principles and Applications*, Revised ed.: Elsevier, 2006.
- [66] V. Kozobolis, A. Konstantinidis, and G. Labiris, "Recognizing a Glaucomatous Optic Disc," in *Glaucoma*, S. Rumelt, Ed., ed: IntechOpen, 2013.
- [67] N. Tabatabaei, A. Mandelis, and B. T. Amaechi, "Thermophotonic lock-in imaging of early demineralized and carious lesions in human teeth," *Journal of biomedical optics*, vol. 16, pp. 071402-071402-10, Jul 2011.
- [68] K. Hajian-Tilaki, "Receiver Operating Characteristic (ROC) Curve Analysis for Medical Diagnostic Test Evaluation," *Caspian Journal of Internal Medicine*, vol. 4, pp. 627-635.
- [69] A. Aden, A. Anthony, C. Brigi, M. S. Merchant, H. Siraj, and P. H. Tomlins, "Dynamic measurement of the optical properties of bovine enamel demineralization models using four-dimensional optical coherence tomography," *J Biomed Opt*, vol. 22, p. 76020, Jul 1 2017.
- [70] J. S. Holtzman, K. Osann, J. Pharar, K. Lee, Y. C. Ahn, T. Tucker, *et al.*, "Ability of optical coherence tomography to detect caries beneath commonly used dental sealants," *Lasers Surg Med*, vol. 42, pp. 752-9, Oct 2010.

- [71] Y. Shimada, H. Nakagawa, A. Sadr, I. Wada, M. Nakajima, T. Nikaido, *et al.*, "Noninvasive cross-sectional imaging of proximal caries using swept-source optical coherence tomography (SS-OCT) in vivo," *J Biophotonics*, vol. 7, pp. 506-13, Jul 2014.
- [72] S. Kaipravil and A. Mandelis, "Truncated-correlation photothermal coherence tomography for deep subsurface analysis," *Nature Photonics*, vol. 8, p. 635, 06/29/online 2014.
- [73] D. C. Adler, S.-W. Huang, R. Huber, and J. G. Fujimoto, "Photothermal detection of gold nanoparticles using phase-sensitive optical coherence tomography," *Optics Express*, vol. 16, pp. 4376-4393, 2008/03/31 2008.
- [74] A. Melnikov, K. Sivagurunathan, X. Guo, J. Tolev, A. Mandelis, K. Ly, *et al.*, "Non-destructive thermal-wave-radar imaging of manufactured green powder metallurgy compact flaws (cracks)," *NDT & E International*, vol. 86, pp. 140-152, 2017.
- [75] L. Litwin, "Matched filtering and timing recovery in digital receivers," *RF design*, vol. 24, pp. 32-49, 2001.
- [76] N. Tabatabaei, "Matched-Filter Thermography," *Applied Sciences*, vol. 8, p. 581, 2018.
- [77] N. Tabatabaei and A. Mandelis, "Thermal-wave radar: A novel subsurface imaging modality with extended depth-resolution dynamic range," *Review of Scientific Instruments*, vol. 80, 2009.
- [78] M. A. B. Othman, J. Belz, and B. Farhang-Boroujeny, "Performance Analysis of Matched Filter Bank for Detection of Linear Frequency Modulated Chirp Signals," *IEEE Transactions on Aerospace and Electronic Systems*, vol. 53, pp. 41-54, 2017.

- [79] N. Tabatabaei, A. Mandelis, and B. T. Amaechi, "Thermophotonic radar imaging: An emissivity-normalized modality with advantages over phase lock-in thermography," *Applied Physics Letters*, vol. 98, p. 163706, 2011/04/18 2011.
- [80] T. Nima and M. Andreas, "Thermal Coherence Tomography Using Match Filter Binary Phase Coded Diffusion Waves," *Physical Review Letters*, vol. 107, p. 165901, 2011.
- [81] P. Tavakolian, S. Sfarra, G. Gargiulo, K. Sivagurunathan, and A. Mandelis, "Photothermal coherence tomography for 3-D visualization and structural non-destructive imaging of a wood inlay," *Infrared Physics & Technology*, vol. 91, pp. 206-213, 2018/06/01/ 2018.
- [82] P. Tavakolian, K. Sivagurunathan, and A. Mandelis, "Enhanced truncated-correlation photothermal coherence tomography with application to deep subsurface defect imaging and 3-dimensional reconstructions," *Journal of Applied Physics*, vol. 122, p. 023103, 2017.
- [83] S. Kaipilavil and A. Mandelis, "Truncated-correlation photothermal coherence tomography for deep subsurface analysis," *Nature Photonics*, vol. 8, pp. 635–642, 2014.
- [84] S. Kaipilavil, A. Mandelis, X. Wang, and T. Feng, "Photothermal tomography for the functional and structural evaluation, and early mineral loss monitoring in bones," *Biomedical Optics Express*, vol. 5, pp. 2488–2502, 2014.
- [85] O. Ashkan, P. Artur, and T. Nima, "First step toward translation of thermophotonic lock-in imaging to dentistry as an early caries detection technology," *Journal of Biomedical Optics*, vol. 21, pp. 96003-96003, 2016.